UCL Université catholique de Louvain

École polytechnique de Louvain (EPL)

epl

Study of the mechanical properties of sintered ternary carbide Cr_2AlC as a function of temperature

Dissertation presented by
Florian LHOEST

for obtaining the Master's degree in
Chemical and Materials Engineering
Option(s): Nanotechnology

Supervisor(s)
Pascal JACQUES, Jean-Pierre ERAUW

Reader(s)
Matthieu MARTELEUR, Thomas PARDOEN

Academic year 2017-2018

Acknowledgements

This work would not have been possible without the hard work and expertise of a great number of people helping me along the way. Starting from the beginning, with my promoter M.Jacques whom I wish to thank for his continuous support and guidance along the way. M.Erauw, whom I cannot thank enough for his help and invaluable time he dedicated me during my internship and the whole year. I am grateful for his advice and the car rides together to Mons.

Many thanks to my tutor, M.Marteleur. The door to his office was always open when I ran into trouble or had questions about my research.

I am enormously indebted to the researchers of the laboratories of chemistry of Louvain-La-Neuve for their efforts in helping me during the different tests performed during this year, giving me the necessary schooling that allowed me to realise most of these tests by myself and securing all the images and data that adorn these pages.

A very special gratitude goes to the staff of Belgian Ceramic Research Centre which I had the chance to work with during my internship. It was fantastic to have the opportunity to conduct the majority of my research in your facilities.

I would also like to acknowledge M.Pardoen from IMAP of the UCL as the third reader of this work, and I am gratefully indebted to his very valuable comments on this thesis.

I am grateful for my family for being a constant source of encouragement and support in my life and especially during the last months. I am also grateful to my other family members and friend who have encouraged me along the way.

To my father especially, thank you for all your help and your unbelievable patience and invaluable contribution along the year. This work wouldn't be what it is without his critical and exterior opinion. I am also very grateful to him for the four previous years during which he was always present when I was in trouble and when I needed help. You were always there to encourage me and recenter me when I strayed from the right path.

Lastly, I offer my regards and blessings to all of those who supported me in any respect during the completion of this work.

Abstract

In this work, the mechanical behaviour under compression at room and high temperature of a bulk Cr_2AlC sample is studied. The microstructure resulting form conditions of loading and heat treatment during the sintering process are identified. The purity and the density of these samples are also determined. An additional phase present in the samples after sintering containing iron is observed and an identification of this phase is achieved. Hardness tests of Vicker and Berkovich are performed on sintered sample at room temperature with different grain sizes and different tips of indentation. The global and local hardness is then obtained. Sample are machined in two macroscopic shapes, square-based bar samples under the dimension 3x3x8 mm^3 and cylinder samples with a diameter of 4 mm and a height of 8 mm. These samples are also extracted from the sintering specimen under different directions regarding the compaction direction. Then, they are compressed in a plasto-dilatometre at 800 and 1000°C at different amount of deformation and observed with scanning electron microscope to identify the mechanisms of damaging and deformation. Then, creep resistance of the Cr_2AlC is studied for samples with different grain sizes and passed mechanical and thermal treatments. This property is compared with the other MAX-phase Ti_3SiC_2 and the dependence on the grain size is confirmed. Eventually, perspective for future researches to continue this study are proposed.

Contents

List of Figures

Chapter 1

Introduction

1.1 First overview, the ceramics

A ceramic is an inorganic compound, but not a metal, and often oxide, carbide or nitride material. It is an abundant material on earth which can have a very varied composition. Besides oxides, carbides and nitrides, one can also find silicides, tellurides, silicates, etc... in this family of materials. The first ceramic appeared tens of thousand years ago, and they were used first for pottery 6000 years ago. This kind of material and its synthesis process are still very present nowadays. The first process to make pottery is the potter's wheel appeared in Egypt 5000 years before Christ (BC). The first closed oven appeared 4000 years B.C. I allowed for a higher and better controlled temperature in comparison with an open oven [ENS98]. During the same millennium, glass was discovered.T his material based on the chemical compound silica, or quartz was first used for jewellery.

The class of ceramic has such a large possibility for the composition and the structure as well as all elements, all types of bonding and all levels of cystallinity can be found. Due to this large diversity of the composition, their properties vary also a lot and this is why the ceramics are used in a wide range of applications. For example, most of them are brittle, hard while they have low toughness and ductility. They can also withstand chemical erosion, which means that they are very stable in various types of hostile environment. In general, they are strong in compression while they are weak in shearing and torsion [Wik18b]. They have a high melting point which allow them to be used in high temperature applications, even under strong mechanical stresses.

The ceramics used in technological applications can be divided in two groups; traditional and advanced ceramic materials. In the class of traditional ceramic materials we find white wares, structural clay products, brick and tile, abrasives, refractories and cement [Sub18]. However in advanced ceramic class more exotic ceramic materials used in specific applications like electro-ceramics, tribological ceramics, automotive ceramics, etc. can be found as well as the so-called MAX-phases. The specific ceramic type studied in the report is described in the next section. Firstly, the MAX-phases will be introduced in a general manner with their structure and main properties. A quick overview of the synthesis process will follow before a highlight of some examples of applications and potential field activity for MAX-phases. Then, the material studied in this work and its main properties are detailed.

1.2 State of the art

1.2.1 The MAX-phases

MAX-phases have been first reported by Nowotny in 1970-1971 [Now71] as a ceramic carbide or nitride, and more specifically as a ternary layered carbide or nitride. The general formula is $M_{n+1}AX_n$ where M is an early transition metal, A is an A-group element (mainly III-A and IV-A element) and X is either carbon (C) or nitrogen (N) (see Figure 1.1). This notation is the reason why this family of ceramics are called MAX-phases. Nowadays, almost 70 MAX-phases have been reported by successful synthesis of the carbides or nitrides with different combinations of the three kinds of elements [ALG17]. The Figure 1.1 shows the different elements in the periodic table apt to be used as components of the MAX-phase family. It also shows many possibilities of MAX-phases already discovered.

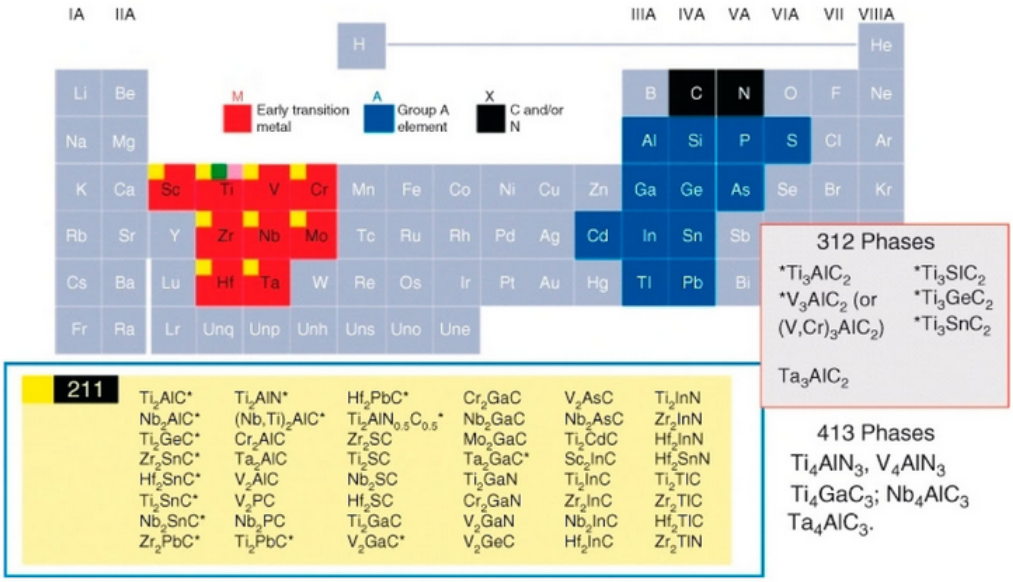

Figure 1.1: Periodic table summarized different MAX-phases discovered [Bar13]

The structure of MAX-phases is represented in Figure 1.2, they are ternary nanolaminates with a close-packed hexagonal lattice in the space group P63/mmc, where M layers are separated by layers of A group element, while X atoms fitting into octahedral sites of M layers [Low12]. As shown in Figure 1.2, MAX-phases can be classified regarding their number of atoms of M-, A- and X-elements. For example, 211 corresponds to class M_2AX components, 312 for M_3AX_2, etc.

Due to this particular structure, one layer of carbide separated by one layer of a metallic element, the properties of these materials are a combination of metallic and ceramic properties. Indeed, it is the alternation between the strong covalent bonds M-X and the weaker metallic bonds M-A that induces this combination of properties. This unique set of properties if of great interest to researchers in the world, and many studies have been performed.

MAX-phases have, like general ceramics, a high strength, a high melting point, a thermal stability and a good oxidation resistance. Also, like metallic materials, they exhibit good thermal and electrical conductivity, which is not the case of general ceramics. They are also easily machinable, fatigue and thermal shock resistant. Furthermore, they are damage tolerant, resistant to chemical attack, have a relatively low thermal expansion coefficient and some are creep resistant ([BR11] and [Low12]). The lamellar structure of MAX-phase family can be observed in Figure 1.3 on a surface of a sample of Cr_2AlC.

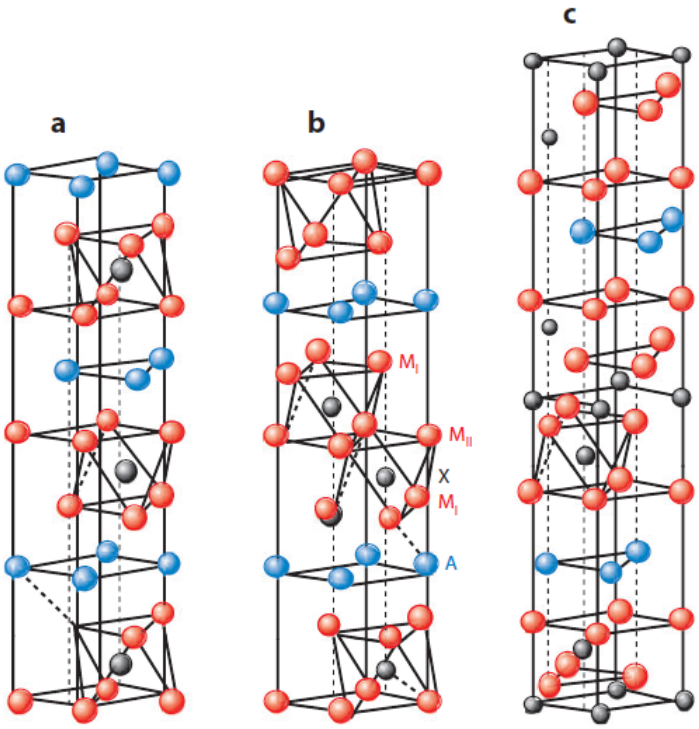

Figure 1.2: Structure of one unit cell of MAX-phases : (a) 211, (b) 312 and (c) 413 [BR11]

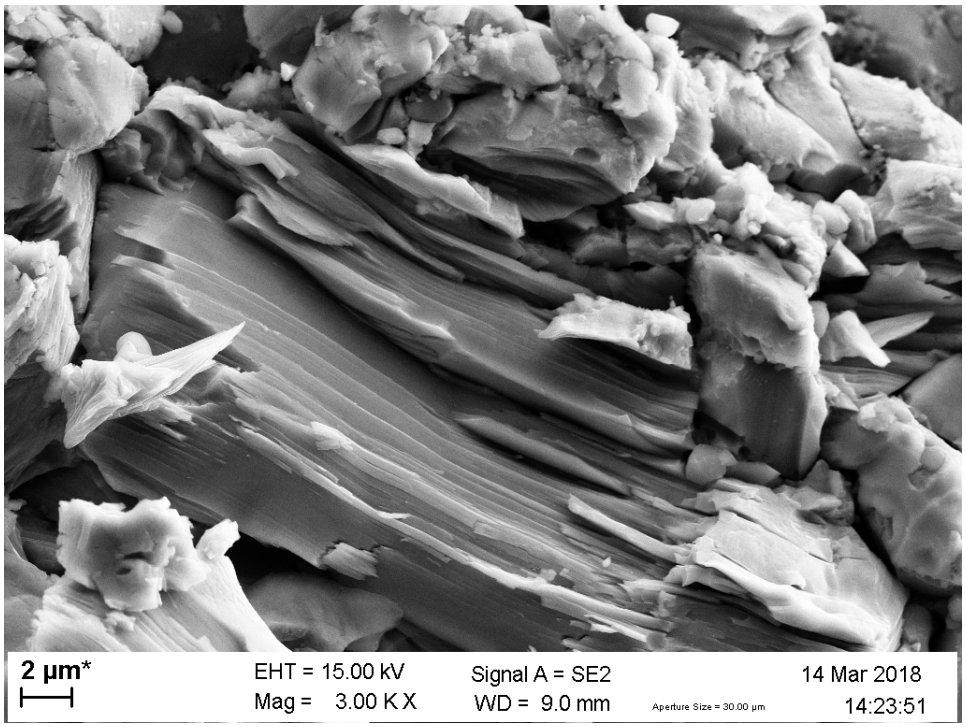

Figure 1.3: SEM image of the surface of Cr_2AlC sample where the structure in lamellae of MAX-phases are observed

1.2.2 Synthesis process

Spark Plasma Sintering

The main process used to synthesis MAX-phases is the sintering process. From raw powders of carbides and pure A-elements also in the form of powder, the sintered process consists of

heating at high enough temperature and press the powder at a sufficient load to obtain a 3D bulk material. Examples of the processes are hot isostatic pressing (HIP), self-propagating high-temperature synthesis (SHS), pulsed laser deposition (PLD) or spark plasma sintering (SPS). This last method has many advantages as a lower temperature process, a shorter time of sintering with the possibility to heat the sample quickly in the matrix [Low12]. The SPS components are represented on the Figure 1.4 where the graphite spacer applied the load on a matrix, composed of the graphite punch and graphite die. The powder at the centre of the framework is pressed by the punches. Because the whole structure is made of graphite, the powder is heated by Joule effect but also by the heat transfer from the matrix. With this technique, the heating rate for the SPS can reach 1000°C/min. However, a too high heating rate could imply an inhomogeneous material because of too high temperature gradient between the core and the surface of the sample during the process [Dem11].

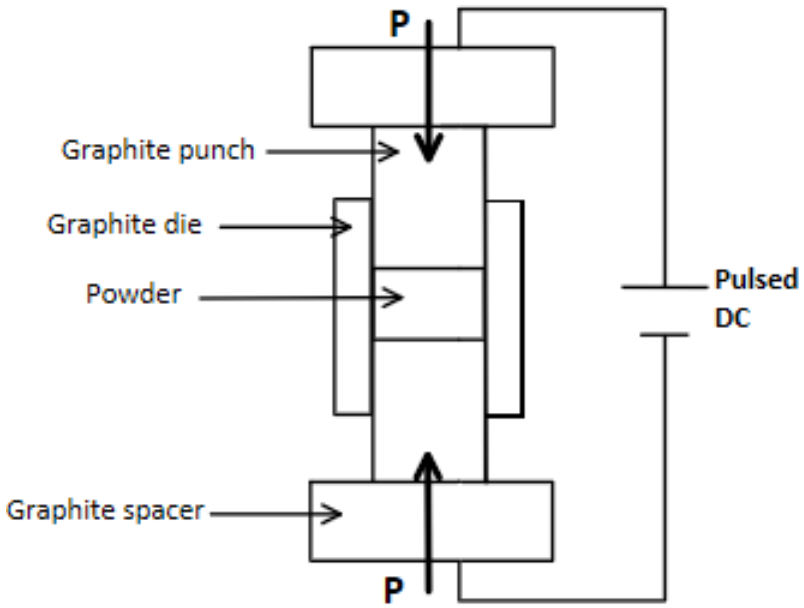

Figure 1.4: Schematic representation of the SPS equipment with different elements highlighted as well as the pressure and the direct current applied to the powder [Dem11]

As in any sintering equipment, the application of the pressure makes reaching the same final density of the product with a lower temperature possible. It also allows keeping finer grains in the material during the process because a higher temperature helps their growth. So the advantage of the SPS in comparison with other techniques are a shorter sintering time, a lower sintering temperature and pressure and a higher densification rate. It does not need a cold compaction, and it is less sensitive to initial powder composition. Materials difficult to sinter are easier to synthesis with this process and the product obtained has a finer and more homogeneous microstructure as well as a higher density [Low12].

Synthesis of pure Cr_2AlC

The technique used to synthesis the sample plays an important role in its densification. The starting mixture also plays a role. Then, J. Gonzalez-Julian and al. proposed an experimental procedure to obtain fully dense and highly pure MAX-phase Cr_2AlC. The procedure consists of, firstly pressureless sintering using raw powder composed of Cr/Al/C in molar ratio (2:1.1:1)

because of a loss of Al content during the thermal process, to obtain a pure MAX-phase but not fully dense. Then, SPS densification [GJOBG16].

If the two steps of the mechanism are compared separately, the sample is either not pure, or not dense enough. In the case of the process without the first step, pressureless calcination, pure MAX-phase is not obtained at a temperature of 1400°C. According to Gonzalez, one of the explanations is the heating rate and the isothermal plateau that are not optimal for the synthesis of Cr_2AlC because a fast heating and short isothermal holding time limit the kinetic of the reaction. While, with the mechanism without the SPS process, the density obtained at 1400°C for the pure Cr_2AlC is 5.08g/cm^3 [GJOBG16].

With the process in two steps, highly dense and pure sample is obtained, 5.17 and 5.21 g/cm^3 whereas the theoretical density of Cr_2AlC is 5.229 g/cm^3 (JCPDS 029-0017), for a temperature of 1250-1300°C with a heating rate of 100K/min and an isothermal holding time of 10 minutes and under a pressure of 50 MPa. But at 1300°C small traces of Cr_2Al are detected, so the optimal condition is at 1200°C [GJOBG16].

1.2.3 Applications

Before going into the details of the main applications of MAX-phases, availability and cost have to be put in perspective. Firstly, Max-phases can be processed as bulk materials, powders, porous foam, coating and thin films. In general, powder of highly pure MAX-phases are more expensive than mechanical ceramics like alumina, silicon carbide and nitride powders used as structural and high temperature ceramics. Therefore, as MAX-phases are readily machinable with high tolerance, this implies that the final cost can be competitive compared to other mechanical ceramics [RB13].

Some applications have already been listed by Barsoum *et al.* [Bar00] like a substitution for machinable ceramics, kiln furniture or heat exchangers. Other sectors for potential applications have been identified, for example in the electronic sector where MAX-phases are used as electrodes, or as microelectronic elements. They can be coated on the surface of another material to protect it from corrosion and wear, or as a damping material. In the sector of the defence, they can be used as materials for armour in nuclear applications, etc. and in the automobile sector, as exhaust gas filters. Eventually, they can also be used as biomaterials.

Recently, a group of researchers found an example of a high-temperature application for the MAX-phases. It is used in a novel high-temperature reactor for an *in situ* X-ray absorption spectroscopy measurement in fluorescence [GGP$^+$09]. For this application, the reactor has to heat a sample up to 1000°C and work under oxidizing or reducing atmospheres. The heater part also has to be easily machinable in order to design it into a circular form with a zigzag shape to increase the resistivity. The heating element of the reactor is shown on the Figure 1.5 where the Maxthal 211 is another name for the MAX-phase Ti_2AlC and the sample in the form of a pellet is placed directly onto the Maxthal [GGP$^+$09]. The properties of thermal shock resistance, wear, oxidation and corrosion resistance, but also the good thermal and electrical conductivity of the Maxthal are used for this application.

MAX-phases have also been determined as superior to steel for high temperature materials like gas burner nozzles, in a corrosive environment containing sulphur gas. The MAX-phase used here is also the Maxthal because due to the Al layers, an additional layer of alumina is formed on the surface to protect the material from corrosion and oxidation. After one year in such a furnace at 1200-1500°C, the nozzle made of steel is completely deteriorated while the Maxthal is still available [Sun11].

For researchers J. Gonzalez-Julian *et al.*, the Cr_2AlC also formed alumina outer layer after a thermal barrier coating on its surface. The oxide layer is formed by diffusion of the Al atoms

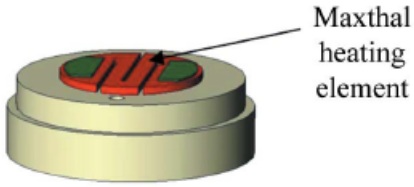

Figure 1.5: Schematic view of the circular Maxthal (Ti_2AlC) heating element into a zigzag form and supported by a substrate in boron nitride [GGP+09]

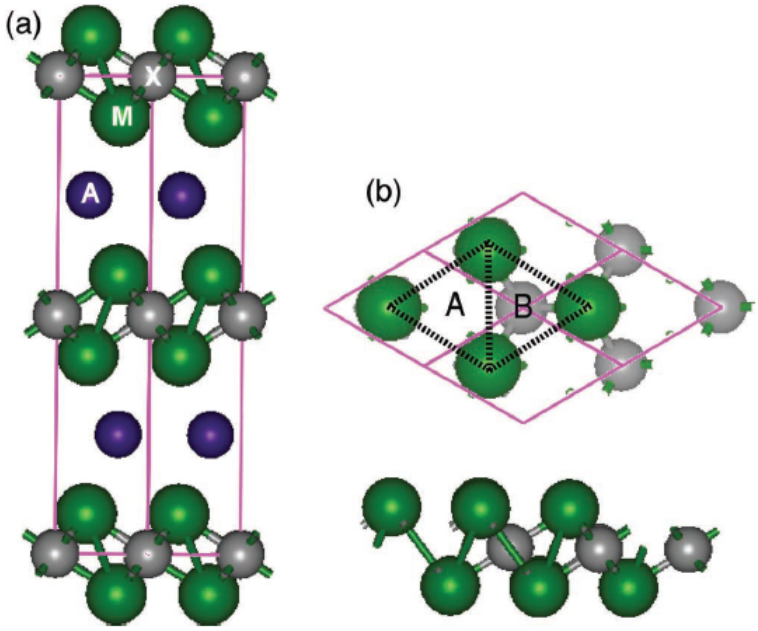

Figure 1.6: Schematic representation of (a) the structure of a MAX-phase of type M_2AX, (b) top view of a layer of MXene with upper available sites A and B after the etching of the A-layer and (c) structure of a single-layer MXene [KAS+13]

through the surface and its thickness varies between 10 and 50 μm as a function of the temperature of the coating. Such a sample presents remarkable resistance under cycling of heating and cooling which confirms the potential of MAX-phases to work for a long time at high temperature and in an oxidation environment [GJGMV18].

Another potential application for the MAX-phase family has been found by Naguib *et al.* in 2011. It consists of etching a MAX-phase as a bulk material in an acid solution of hydrogen fluoride (HF) to attack and remove the A-layers. A mechanical step called sonication is then performed to separate the different layers of carbides remaining and form a 2D nano-layered material that has been named MXene in analogy to the graphene [NKP+11]. These MXenes are mono-layers of carbides and/or nitrides, as a function of the MAX-phase etching, as represented in Figure 1.6.

Like its parent materials, MXenes exhibits an interesting combination of properties such as an electrical conductivity close to that of multi-layer graphene, but also a semi conducting behaviour and a magnetic behaviour as a function of the structure and the composition of the MXenes [LZZ15]. A promising application for this family of materials is the Li-ion battery. Due to its particular structure after the etching ([LZZ15]) the ions of Li can be stored and realized on the surface of the MXene layers [ALG17].

1.3 Compression and creep resistance

Mechanical properties and behaviour of a given material can be determined with a compression or a tensile test. These tests are performed by applying a force on the sample to respect a certain displacement rate previously defined. With that kind of test, a stress-strain curve can be drawn that describes the mechanical response of the sample under loading. It is then possible to obtain information such as Young's modulus, ultimate stress and strain or the strain at the fracture, for example. Furthermore, the toughness, the capacity of the materials to deform plastically and its ductility can be determined.

An example of this curve is given by the Figure 1.7. The Stress is noted σ and is expressed in Pa and the strain is ϵ, expressed in %. This typical curve shows information like the Young modulus, noted E, which is the slope of the first linear part of the curve, the point 1 is the yield strain, the "exact" moment when the material starts to deform plastically. Or, in other words, when the relation between the stress and the strain in not linear anymore. Then, the point 2 is the yield strain à 0.2%, a standard value that also defines the beginning of the plastic deformation of the material. This value is used for classical materials where the distinction between the elastic and the plastic region on the curve is not obvious. An example of this type of curve is given on the Figure 1.15.

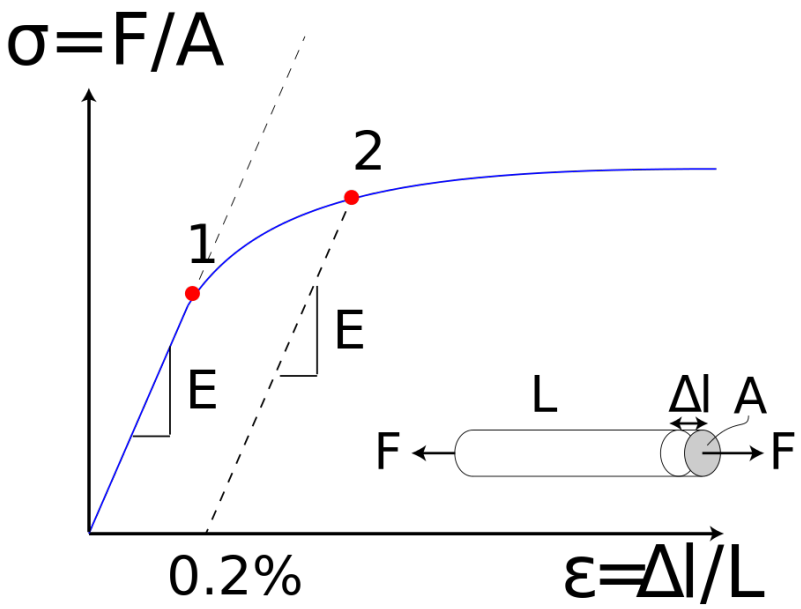

Figure 1.7: Theoretical stress-strain curve where the points 1 and 2 are two definitions of the Yield strain [Wik18f]

While a sample is stressed in compression between pistons, the geometry is critical to prevent buckling. This phenomenon is characterized by a sudden sideways deflection of the sample that may cause the fracture even if the stress applied is well below the critical stress of failure. An example of buckling is shown in Figure 1.8 (c) for a ductile material. In general, the use of samples with a ratio h/d > 2-3 (h is the height and d is the diameter or the characteristic size of the base) is avoided to prevent buckling and shearing of the sample during the test [Ins18]. If the ratio h/d < 2, and due to the profile of friction at the surface in contact with the piston during the compression test, the specimen will deform in the shape of a barrel. This phenomenon is called the barrelling of the sample. The profile of the friction at the surface in contact with the pistons shows a minimum at the centre of the surface while the maximum is located at the edges,

which implies that the horizontal component of the local strain is small. An example, also for a ductile material, is shown in Figure 1.8 (a).

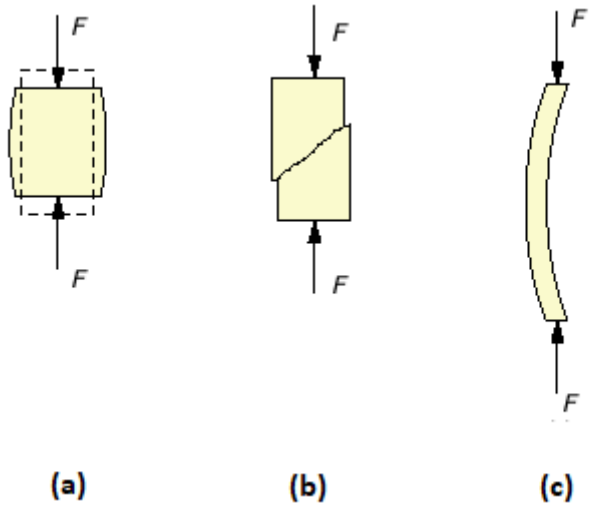

Figure 1.8: Behaviour in compression of a (a) ductile specimen with a small h/d ratio (height/base), (b) brittle specimen, with small h/d and (c) ductile specimen with a large ratio h/d [eFu18]

If the property to be tested is the resistance of a material to creep, the test involves a tensile or compression sample under constant load and at a constant temperature, mainly close to the melting temperature of the sample. Once the loading is applied at the given temperature, the sample starts to deform plastically, following the three modes of creeping. The first one called the primary strain (see Figure 1.9) implies a large deformation in a short time. Then the steady-state creep begins where the relation between the strain and the time is linear. From this step, the following equation can be written;

$$\dot{\epsilon}_{ss} = B\sigma^n \tag{1.1}$$

Where $\dot{\epsilon}_{ss}$ strain rate of the steady-state creep, σ is the stress, n the creep exponent and B a constant. Eventually, the strain increases again in a short time and the specimen begins the tertiary mode and creeps until the fracture of the material at the time t_f. A theoretical curve of the behaviour of a metal under constant load is shown on the Figure 1.9.

Depending on the load applied during the creep test, two different mechanisms can be identified: the diffusion creep at low stress and the power-law creep at higher stress. Because it depends upon the mechanism, the Equation 1.1 can be modified in the form:

$$\frac{\partial \epsilon}{\partial t} = \frac{C\sigma^m}{b} e^{\frac{-Q}{kT}} \tag{1.2}$$

Where ϵ is the creep strain, C is constant and dependent on the material tested and the particular creep mechanism, m and b are also constants that depend on the creep mechanism, Q is the activation energy of the creep mechanism, σ is the stress applied, d is the grain size of the material, k is the Boltzmann's constant, and T is the absolute temperature of the test [Mur17].

The diffusion creep refers to the diffusion of vacancies through their crystal lattice. To allow this diffusion, the atoms next to the vacancies have to "jump" in the empty sites. Therefore, an activation energy is needed to perform this mechanism. The mass transport of the vacancy is then easier at a higher temperature.

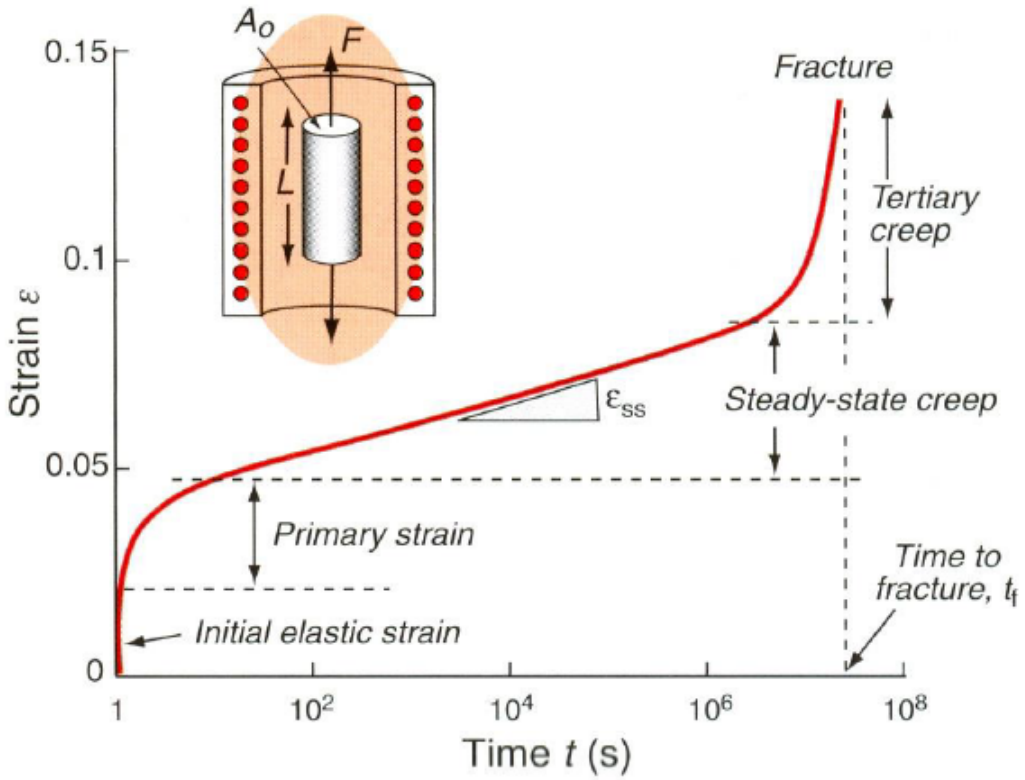

Figure 1.9: Theoretical curve obtained with a creep test, a continuous deformation with time and ending with the fracture of the sample [JS18]

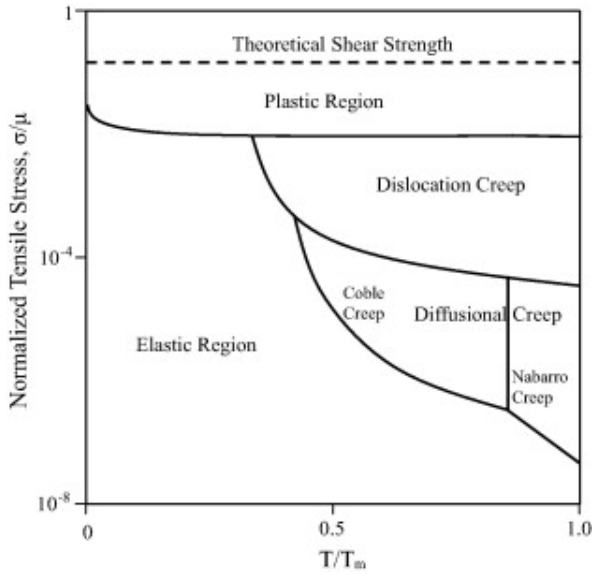

Figure 1.10: Deformation mechanism diagram that predicted the mechanism contributing to creep deformation in a typical metal as a function of the temperature and the stress level [CK14]

At low stress, the vacancies diffuse rather inside the grain than from one grain boundary to another, this is called Herring-Nabarro creep. They are able also to diffuse in the grain boundaries. This mechanism is called the Coble creep [Wik18d]. By applying the stress on the sample, nucleation of vacancies is favoured in the direction perpendicular to the tensile stress. Inside the grains, the vacancies will diffuse from the grain boundaries normal to the applied stress toward those parallel to it and the grains will elongate. So, the grain boundaries act as perfect

sources and sinks for the vacancies [CM99]. Figure 1.11 (b) shows the motion of the atoms while the stress is applied (red arrows) and the deformation of the grains due to the diffusion.

The mechanism proposed by M. Coble [Cob63] occurs at a lower temperature than the mechanism of Herring-Nabarro (see Figure 1.10). The diffusion of the atoms is observed along the grain boundaries instead of in the bulk, which implies an elongation of the specimen [CM99]. For these two models, the resistance of a material to creep enhance with the increase of the grain size. Indeed, the deformation rate will be inversely proportional to the size of the grain and so decrease when the grain is bigger. A directional solidification can be performed to eliminate as many grain boundaries as possible that are perpendicular and inclined to the stress (tensile) axis [CM99].

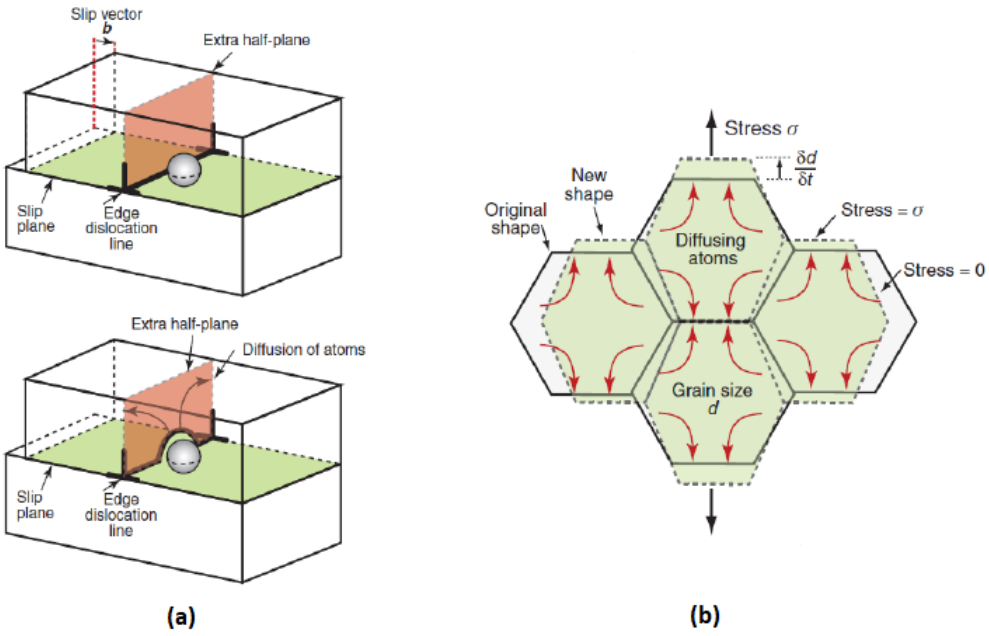

Figure 1.11: (a) Schematic mechanism of power-law creep, the dislocations climb overcome the obstacle and (b) Schematic view of the mechanism of diffusion of the atoms inside the grains, from the grain boundaries normal to the applied stress σ toward those parallel to it (red arrow) which result in the elongation of the grains of $\frac{\delta d}{\delta t}$ (where d is the grain size) in the direction of σ [JS18]

If the stress applied on the sample is significantly increased, another creep mechanism can be identified, the dislocation creep (Figure 1.10). In this case, the creep is performed rather by dislocation glide than with vacancies diffusion. During this mechanism, the dislocations are pinned by obstacles, like interstitial atoms or precipitates, and overcome them by climb as shown in Figure 1.11 (a). The deformation creep, here, is dependent on the rate of escape of a dislocation from the impurity. This rate depends on the repulsive forces, generate due to the stress field around the impurities, that have to be exceeded by the applied stress on the dislocation itself.

1.4 Main properties of MAX-phases

1.4.1 The Brittle-to-Plastic Transition

Until now, every MAX-phase system studied presents a brittle-to-plastic transition (BPT) for these mechanical properties. This behaviour is specific to this family of materials. The following

analyses have been realized on few MAX-phases and in particular on Ti_3SiC_2. The mechanical response of this compound depends on the temperature and the deformation rate. At room temperature, the dislocations are only allowed to move through the basal plan of the hexagonal structure of the MAX-phases, which implies that fewer than 5 independent slip systems (Figure 1.12), needed for the ductility of a polycrystal material, are reported.

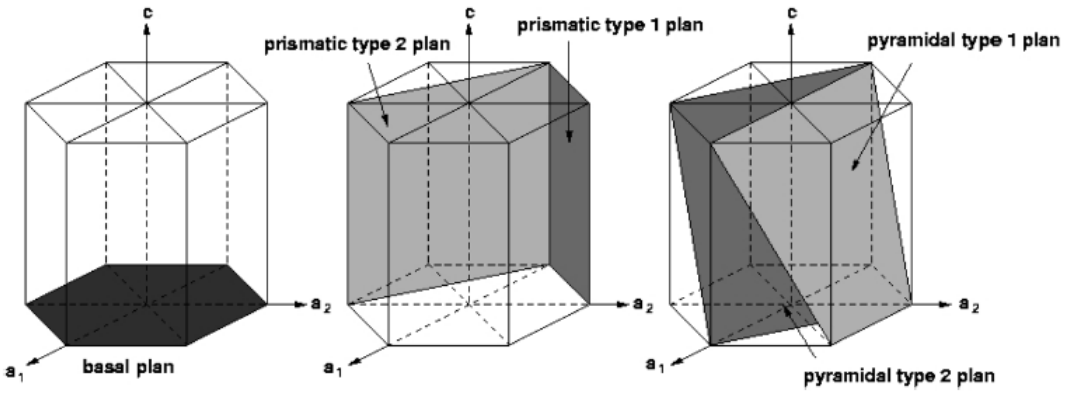

Figure 1.12: Schematic view of a compact hexagonal structure with the different slip systems: (left) basal plan, (centre) type I and II prismatic planes, (right) type I and II pyramidal planes [PRX+11]

For the MAX-phases, the movement of dislocations is impossible in another direction than the basal plan at room temperature and they will fail in a brittle manner, whatever the deformation rate [RB13], [Sun11]. When a MAX-phase is deformed under the BPT, the dislocation that moves through the basal planes arrange themselves in walls or arras parallel to their basal planes. From this configuration of the dislocations, a very important microstructure mechanism appears called the kink band formation, the mechanism is shown in Figure 1.13. When the loading begins, the grains that are well oriented, those where the basal planes are in the same orientation that the easy slip plans, start to deform and cause the development of incipient king bands (IKB) [BZK+03]. These are coaxial dislocation loops that are fully reversible.

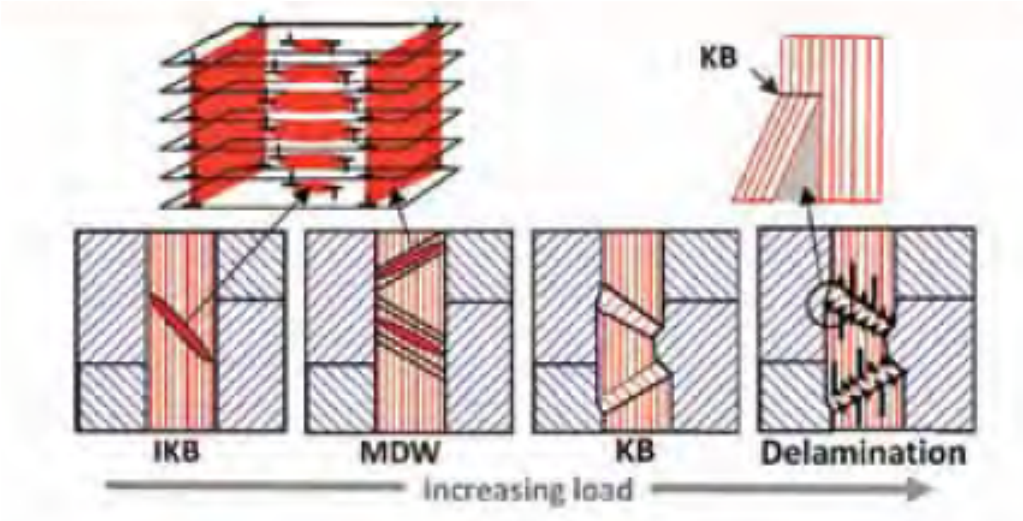

Figure 1.13: Schematic representation of the evolution of the microstructure and the formation of kink bands with the increase of the loading, the blue grain is well oriented in comparison with the direction of loading for an easy slip and the red grain are hard grain where the slipping of dislocations is difficult [RB13]

By further increasing the loading, the IKBs turn to mobile wall dislocation (MWD) and then permanent kink bands (KB), characteristic observation of a deformed MAX-phase. This phenomenon has been observed by M.W. Barsoum *et al.* and is shown in Figure 1.14.

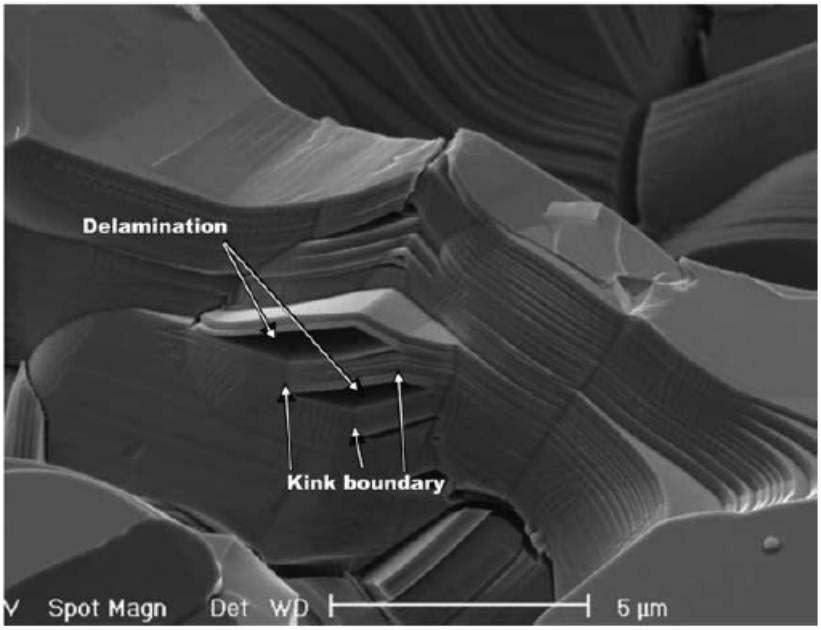

Figure 1.14: Scanning electron micrograph of a porous Ti_3SiC_2 sample that failed in compression, delamination and kink bands are clearly seen [SMZ+05]

In increasing the temperature above the BPT, the grain boundaries are softer and the IKBs are developed in MDW and KB. They will then induce delamination inside the grains and lead to considerable plasticity.

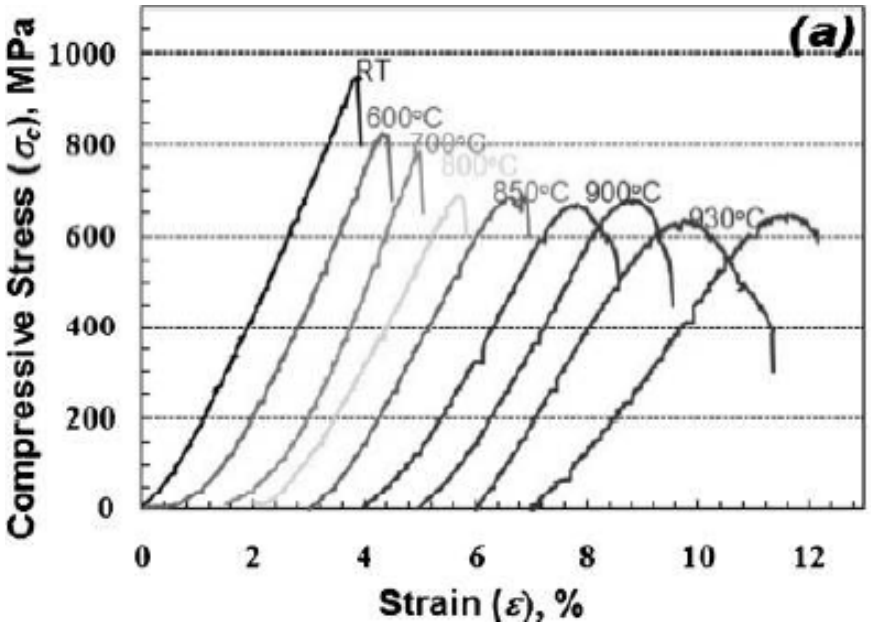

Figure 1.15: Stress-strain curve of Ti_3SiC_2 samples under compression at different temperatures, the brittle-to-plastic transition temperature can be considered between 850 and 900°C [Sun11]

As observed in Figure 1.15, the behaviour of Ti_3SiC_2 changes with the temperature. When the temperature reaches 850°C, the material starts to deform plastically.

1.4.2 Properties of Cr_2AlC

For pure MAX-phase Cr_2AlC, the hardness is around 3.5 GPa [TWZ+06a]. It also has a large elastic modulus (278-288 GPa), good electrical and thermal conductivity (1.4-2.3$\times 10^6$ $\Omega^{-1} \cdot m^{-1}$ and 17.5-22.5 W/M $\cdot$ K respectively) [TWZ+06a] [GJOBG16]. It also shows excellent oxidation resistance, 1.1 $\cdot$ 10^{-11} and 3.0 $\cdot$ 10^{-9} kg^2 m^{-4} s^{-1} at 1000 and 1300°C respectively [GJOBG16].

X. Duan and al. find a hardness of 3.4± 0.2 GPa and 5.3 ± 0.9 GPa for a coarse- and fine-grained Cr_2AlC sample sintered at 1400°C, respectively [DSJ+15]. For this fine-grained samples after ball-milled, the critical fracture toughness value K_c is 4.6 MPa$\times m^{1/2}$ in all direction [DSJ+15].

Main properties of Cr_2AlC are summarized in the Table 1.1 and compared with other MAX-phases, like Ti_3SiC_2 and the ternary system Ti/C/Al.

Property	Value			
	Cr_2AlC	Ti_2AlC [9]	$Ti_3Al_{1.1}C_{1.8}$ [20]	Ti_3SiC_2 [20]
Elementary cell	Hexagonal	Hexagonal	Hexagonal	Hexagonal
a (Å)	2.863(4)	3.051	3.0654	3.0665
c (Å)	12.814(3)	13.637	18.487	17.671
Theoretical density (g/cm^3)	5.229	4.113	4.247	4.531
Measured density (g/cm^3)	5.21	–[a]	4.2	4.5
Coefficient of thermal expansion (K^{-1})	1.33×10^{-5}	8.2×10^{-6}	9.0×10^{-6}	9.2×10^{-6}
Special heat capacity at 25 °C J/(kg K)	590	579	–[a]	588 [2]
Thermal conductivity at 200 °C W/(m K)	17.5	41.7 [12]	–[a]	43 (at room temp.) [2]
Electrical conductivity (S/m)	1.4×10^6	2.7×10^6	2.9×10^6	4.5×10^6
Temperature coefficient of resistivity, β (K^{-1})	0.0028	0.0035 [12]	0.0031	0.004
Young's modulus (GPa)	278	–[a]	297	333
Shear modulus (GPa)	116	–[a]	124	139
Poisson's ratio	0.153	–[a]	0.2	0.2
Flexural strength (MPa)	378	–[a]	375 ± 15	260 ± 20 [2]
Hardness (GPa)	3.5	4.5	3.5	4 [2,20]

[a] Not reported.

Table 1.1: Summary of some properties of Cr_2AlC compared to Ti_2AlC,$Ti_3Al_{1.1}C_{1.8}$ and Ti_3SiC_2 [TWZ+06a]

Chapter 2

Materials and methods

2.1 Raw materials

For the system Cr/Al/C, CroMax powder (Cr_2AlC) was used. This powder comes from the Institute of Energy and Climate Research in Germany. It has an average particle size of about 6 μm (Figure 2.2), and is highly pure according to the XRD analysis of Figure 2.1.

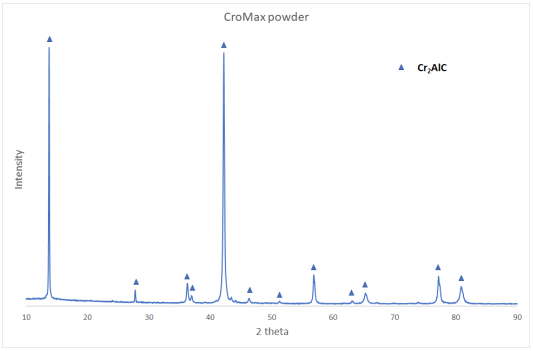

Figure 2.1: XRD analysis of CroMax powder

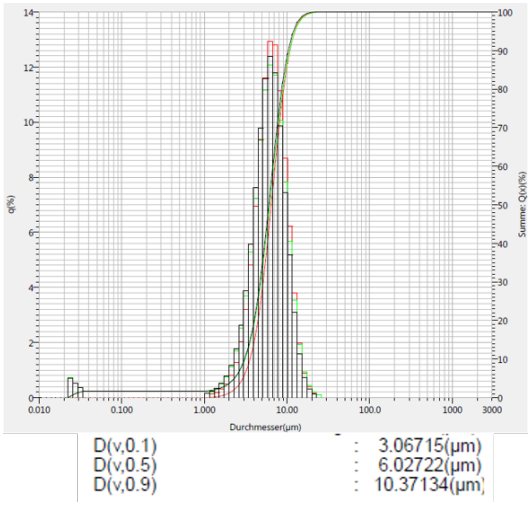

Figure 2.2: Distribution of the grain size of the powder of Cr_2AlC

The small peaks around 43 and 44° represent impurities of Al_2O_3 - Cr_2Al (the major peaks of these two phases are mingled) and Cr_7C_3 - $Cr_{23}C_6$, respectively. These peaks are shown in Figure 2.3 and their relative intensities compared to the main peak are 3.6 and 2.4%, respectively.

ICP analyses have been performed on the powder to eventually identify heavy metals present in impurities. According to this analyse, the presence of chrome and aluminium is indeed observed. On the contrary of the afore-mentioned analysis, a small but not negligible amount of iron has also been found (Table 2.1.

2.2 Sintering by SPS

All the samples have been sintered by SPS (HPD10 from FCT, in Mons at the BCRC, Belgian Ceramic Research Centre). In order to characterize a highly pure and dense sample, different conditions of SPS have been tested.

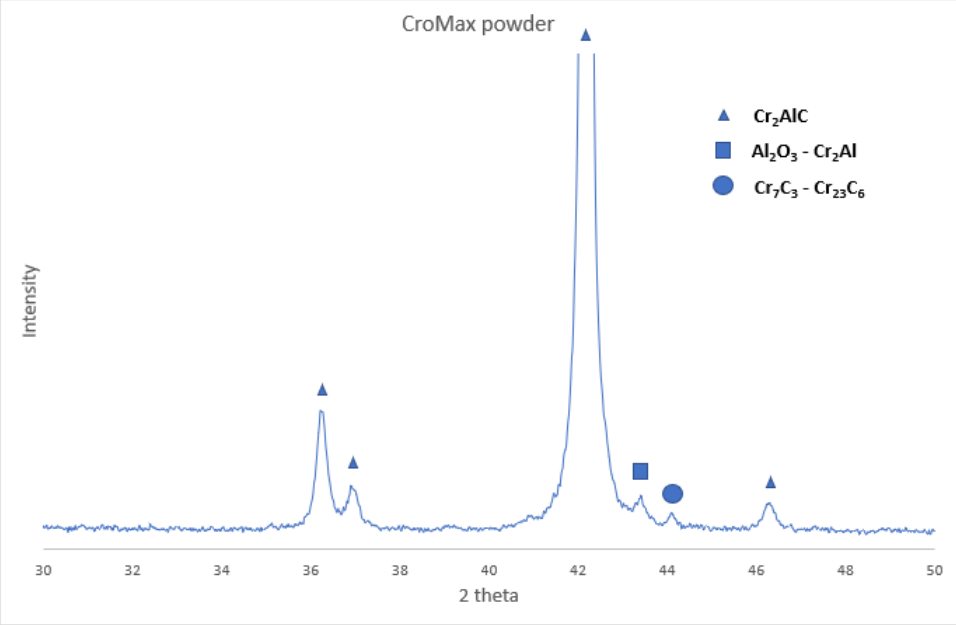

Figure 2.3: Zoom of the Figure 2.1 in the range of 30 and 50° (2 theta angle), the peaks of Al_2O_3 is located at 43.5° and the peak of Cr_7C_3 at 44°

Echantillon	N° Labo	Teneurs %wt Al	Co	Cr	Fe	Ni	Si	Ti	W		C^{tot}	Masse *mg*
CroMax	62188	18,9	0,02	69,4	0,32	0,03	0,04	0,02	0,09		6,52	18,5
		18,8	0,02	70,6	0,31	0,03	0,05	0,02	0,09		5,22	5,3
											8,01	11,2
											6,10	4,9
											7,01	10,2
	Max. 3% d'erreur sur les valeurs											

Table 2.1: Summary of the results obtained by ICP on the powder

First, one sample has been heated at 1400°C for 5 minutes with a heating rate of 100°C/min and under 10 MPa but a part of the material was molten. Another sample has been sintered at 1300°C but it was also molten. Then at 1200°C the sample was well sintered with the same conditions of pressure and heating rate. Other tests were therefore made at this temperature but in varying the other conditions (the operating conditions and a small analyse can be found in Appendix A). Table 2.2 summarizes the different tests. An example of the process of sintering in the SPS is shown in Figure 2.4 for the sample sintered at 1200°C for 5 minutes with a heating rate of 100°C/min and under 10 MPa.

The relative displacement in green represents the displacement of the sample during the process as a function of time in compression. When the relative displacement increases, it means that the height of the sample is decreasing. The shape of the curve as well as the moment and amount of heat and load applied on the sample during the sintering process are described in Appendix A. The curve in red is the absolute temperature measured by the pyrometer at the top of the sample, which means that small differences are allowed in the centre of the sample. The blue curve represents the pressure applied by the pistons on the sample (refer also to Figure 1.4) with a scaling factor equal to 50 to match with the scale of the relative displacement.

All the tests summarized in Table 2.2 were performed with initially 6g of powder, and the height of the sample once sintered was about 3 mm except for two other tests that have then

Temperature (°C)	heating rate (°C/min)	Pressure (MPa)	Height of the sample (mm)
1400	100	10	3
1300	100	10	3
1200	100	10	3
1200	100	30 (800°C)[1]	3
1200	100	30	3
1200	100	50 (800°C)	3
1200	100	50	3
1200	50	10	3
1200	50	50	3
1200	200	10	3
1200	200	50	3
1200	100	10	8

Table 2.2: Summary of the different test performed by SPS on the CroMAX powder

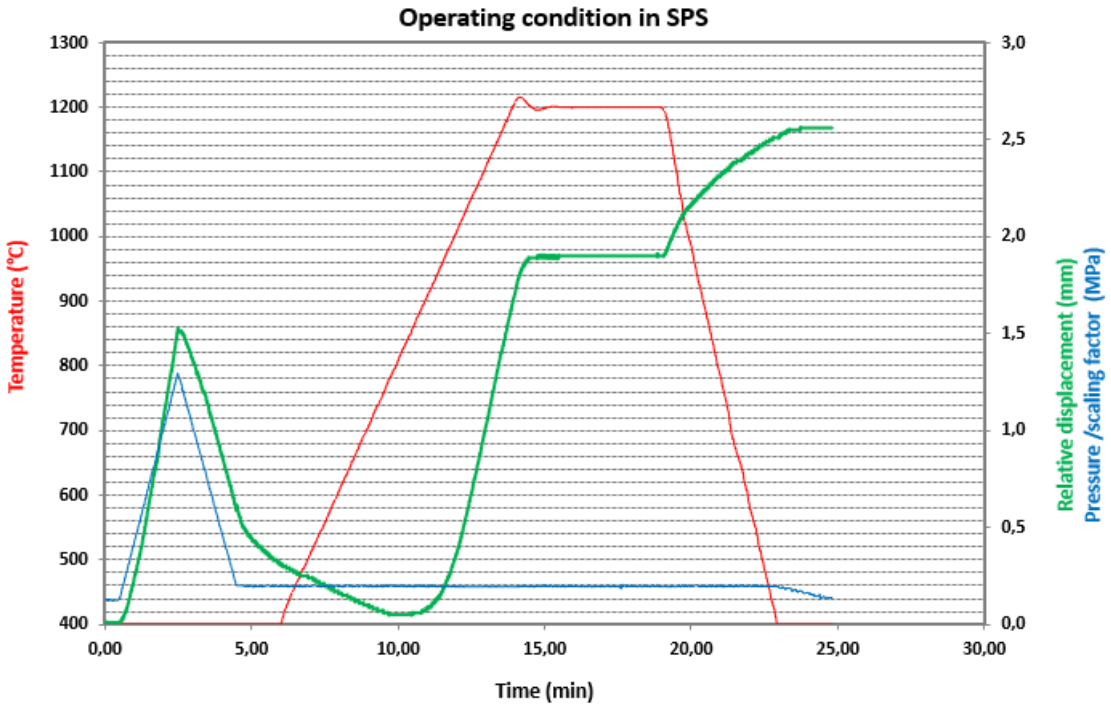

Figure 2.4: Operating condition of a sample sintered, with initially 6g of powder, by SPS at 1200°C with a heating rate of 100°C/min, under a pressure of 10 MPa and with a soaking time of 5 min. The pressure is divided by a scaling factor, which is equal to 50, in order to match with the scale of the relative displacement

been performed to obtain samples with a height of about 8 mm, so with 18g of powder. They have been sintered at a temperature of 1200°C under a load of 10 MPa with a heating rate of 100°C/min and a soaking time of 5 min, which will be the sintering conditions considered as reference for the rest of this work. The sintering curves of these two samples are shown in Figure 2.5 and compared with the sintering curve of the sample sintered in the same conditions but with 6g as amount of initial powder.

[1]The appliance of the pressure start when the temperature of the sample in the SPS reached 800°C because it is the moment when the sample starts to compress under higher temperature, this is the minimum on the sintering curve. These conditions are shown in Figure A.5 in the appendix.

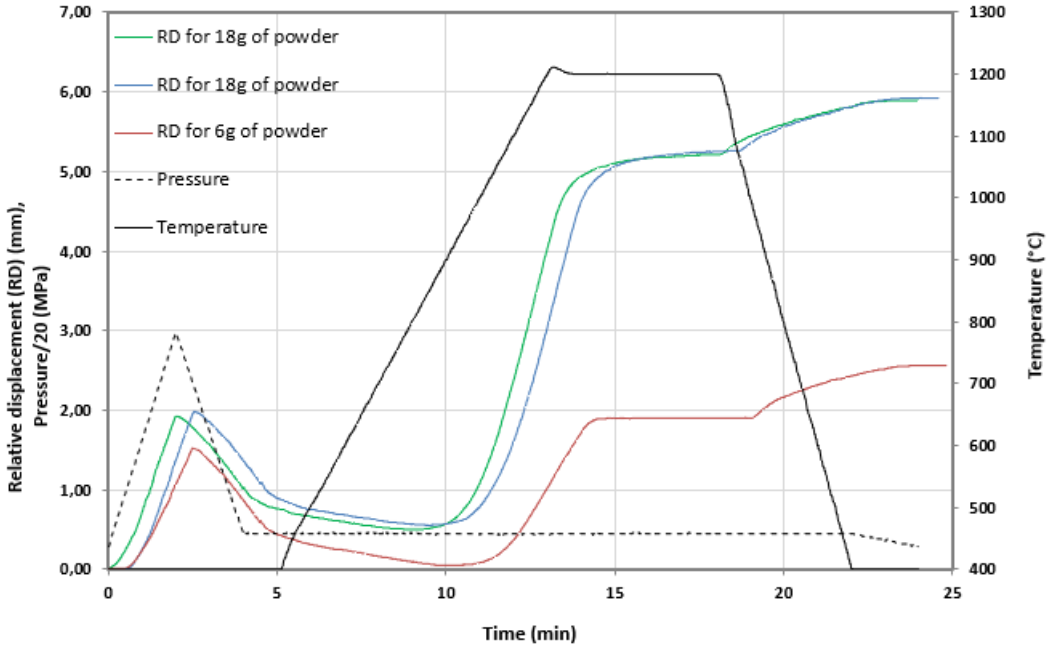

Figure 2.5: Relative displacement of samples sintered at 1200°C for 5 minutes, with a heating rate of 100°C/min and a loading of 10 MPa, the green and blue curves show the two samples sintered in the same conditions

The two curves in green and blue on Figure 2.5 are the relative displacement of the two samples sintered with 18g of powder with a little shift to be allowed to distinct them.

2.3 Sample preparation

In order to prepare a sample of Cr_2AlC after a sintering process in order to observe the microstructure, the different steps described below are performed before each observation at the scanning electron microscope or at the optical microscope:

Cutting methods: A sample of Cr_2AlC can be cut in different ways. Two techniques have been used, micro-cutting and electric discharge machining (EDM).

Polishing steps: Once the sample has two perfectly planes and opposite parallel surfaces as a result of the grinding machine or the cutting process, it can be polished through the different steps as described below:

- approximately 10 min with SiC paper denoted 1200 as a function of its roughness
- 7 min on the 9 μm ceramic Draps Plan disc diamond powder
- 5 min on the 6 μm ceramic Draps Pan disc diamond powder
- 4 min on the 3 μm ceramic Draps Dur disc diamond powder
- 4 min also on the same ceramic support disc (3 μm ceramic Draps Dur disc) with diamond powder of 1 μm

The first step with SiC paper is necessary for roughing the surface up and erasing the main surface porosity. The diamond finishing surface steps are then necessary and sufficient to erase many scratches and observe the surface with scanning electron microscope or with the optical microscope. After all these steps of polishing, clean up the sample in an ethanol bath at the ultrasound machine for 10 minutes is needed to eliminate the gas in the sample and prevent the deposition of dust in the cavities at its surface.

Etching process: In order to be able to observe the grains boundaries, as well as to distinguish the different grains, the sample can be etched in a solution of hydrofluoric acid for 2 to 4 minutes after polishing [TWZ+06b]. The etching is stopped after 4 minutes by dipping the sample in a bath of acetone and is then cleaned up with ethanol and clean water.

2.4 Measurement of the densification

In order to quantify the densification of the samples after the sintering process, the principle of Archimede is used. It allows the calculation of the apparent and the closed density of a sample in performing three weighings (balances used, STARTORUS AC 210S, accuracy of 1/10000). The protocol is to first weigh the sample when it is dry (m_{dry}). Then, two methods to prepare the sample for the next two weighings are used;

- The first method consists in putting the sample in a locked container under vacuum and underwater during enough time (here 2 hours to make vacuum and 2 hours underwater) in order to let the the water penetrate the open pores
- The second method is used only when the first one is not possible because the system of vacuum is not available. This second method is simply an immersion of the sample in clean water for 24 hours. It is then assumed that the water has indeed entered all open pores.

The sample is then weighed twice again: once underwater ($m_{unwater}$) and once wet (m_{wet}) after wiping the sweaty surface in order to not weigh the water outside the pores. This last measure is the less accurate one because of the evaporation of the water during the measurement. Once these three weighings have been done, and the temperature of the water used for the underwater and the wet weighing has been recorded, the following equations are used.

$$\rho_{app} = \frac{m_{dry} \cdot \rho_{liq}}{m_{wet} - m_{unwater}} [g/cm^3] \tag{2.1}$$

$$P_{open} = \frac{m_{wet} - m_{dry}}{m_{wet} - munwater} [\%] \tag{2.2}$$

$$\rho_{app,closed} = \frac{m_{dry} \cdot \rho_{liq}}{m_{dry} - m_{unwater}} [g/cm^3] \tag{2.3}$$

Where ρ_{app} is the apparent density of the sample (which is the ratio of the mass of the dry material to its apparent solid volume, European Committee for Standardization, Ref. No. EN 6232:1993 E), ρ_{liq} is the density of the liquid used for the measure of $m_{unwater}$ (which depends on the temperature of the liquid), P_{open} is the percentage of open pores in the sample and $\rho_{app,closed}$ is the apparent density of the sample without the influence of the open porosity. This last density does not take into account the roughness of the surface of the sample, this means that measuring m_{wet} is not useful anymore.

To eventually compute the relative density, some other parameters are needed. As noted at the beginning of this chapter, the powder used in the sintering process is not 100% pure. Therefore

the theoretical density (ρ_{th}) of Cr_2AlC, Al_2O_3 and Cr_7C_3 are useful and are 5.23 g/cm^3 (JCPDS 04-007-2697 and JCPDS 00-029-0017 [TWZ+06a] [GJOBG16]), 3.97 g/cm^3 [Wik18a] and 6.877 g/cm^3 (JCPDS 36-1482 [TWZ+06a]), respectively. The fraction of each phase in the sample is also useful, x_{Cr_2AlC}, $x_{Al_2O_3}$ and $x_{Cr_7C_3}$, in the following equation.

$$\rho_{rel} = \frac{\rho_{app}}{(\rho_{th,Cr_2AlC} \cdot x_{Cr_2AlC} + \rho_{th,Al_2O_3} \cdot x_{Al_2O_3} + \rho_{th,Cr_7C_3} \cdot x_{Cr_7C_3})} \cdot 100 \ [\%] \tag{2.4}$$

Where ρ_{app} can be replaced by $\rho_{app,closed}$ to compute the relative closed density.

2.5 Measurement of the crystallographic orientation

The texture of a material has a relative "intensity" that gives an idea of the distribution of the crystallographic orientation of a polycrystal. A totally random sample is taken as reference and will have a texture of 1 which means that it has no texture. If a large number of grains have a preferred orientation, the level of texture will be higher than 1 and can even be very large. The texture can be determined in different ways, using the electron back-scattered diffraction or with X-ray diffraction. In general, pole figures are used as a stereographic projection to represent the texture of a material.

The measurement of the texture consists of a comparison of experimental and calculated coefficients for a given symmetry of the sample. If the two values for each coefficient fit well, the symmetry of the sample is identified and the intensity of the texture is found.

A measure of the texture is realized on the sample sintered at 1400°C with the other sintering conditions that respect the conditions chosen as reference. The pole figures are measured and compared with calculated values that correspond to a theoretical symmetry previously chosen. The pole figures that fit well the calculated data with a minimum error will cause the selection of this symmetry and the texture is determined.

2.6 Analyse of the microstructure

The identification of the microstructure of the sample is an important step of this study in order to relate it to the condition of the synthesis process and the mechanical properties. Once the samples are ready to be observed with the optical microscope or by scanning electron microscope (SEM), there are two main parameters to identify: the grain size and the proportion of the different phases, also used to determine the relative density.

In order to be able to see grains at the surface of a sample, the etching process explained above is used. The solution (HF) is used to attack the aluminium layer of the structure of the MAX-phase. The Al-ion once attacked will be removed from the surface and replaced by F-ion. If the sample is attacked for a long time (more than 2 hours), the bulk material will lead to the formation of MXene as explained in Chapter 1.

First, because the samples are sintered (pressed under high temperature) a texture measurement is realised to identify if the grains have a preferential orientation or if the grains are randomly distributed and shaped.

The method used to identify the mean grain size is called the mean linear intercept. That method consists in taking random pictures of the surface (with the optical microscope or with the SEM) and by drawing lines (or circle if the texture of the sample may have an influence) on these pictures. Once the lines are drawn, the number of times a grain boundary crosses the line is counted, and the total length of the line is then divided by this count. Figure 2.6 shows an

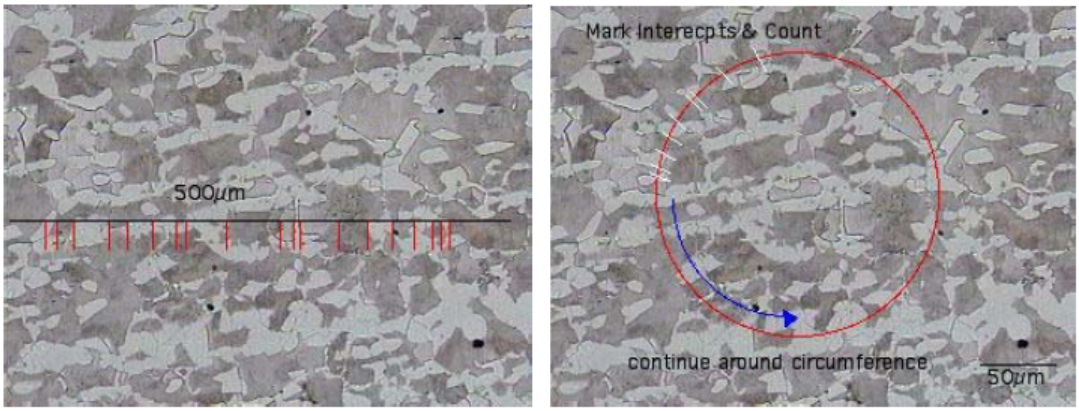

Figure 2.6: Example of mean intercept linear method to determine the proportion of two phases in a sample, (right) example for any microstructure and (left) example of a rolled sample or a sample with a high texture [JI17]

example of intercepts and counts with a line or a circle to determine the proportion of two phases in the sample. It is done by measuring the length of the small segment between two counts, then summing all the length of segments for each phase and divide the result by the total length.

This purely statistical method gives a good approximation for the mean grains size and the amount of MAX-phase and impurities. A summary of the calculation can be found in Appendix D.

2.7 Differential scanning calorimetry

Differential scanning calorimetry measurement has been performed on DSC instrument (NETZSCH STA 409PC/PG). The powder used in the SPS during the sintering process of the sample studied in this work has been analysed by DSC and heated in a furnace with a heating rate of 5°C/min until 1490°C. The measure gives the heat flow necessary to keep the powder at the same temperature as a reference material (alumina) placed in a second furnace.

2.8 Vicker's and Berkovich hardness

In general, MAX-phases are softer than structural ceramics. Their Vicker's hardness lies between 2 and 8 GPa [BR11]. The hardness represents the material's ability to resist to plastic deformations. The hardness cannot be considered as a fundamental property of the material, but it has to be considered as an empirical and comparative method to test the resistance of a material to plastic deformation [CM99]. The indentations and the measures of the hardness have been achieved at room temperature in two ways. First, the measure is performed with a micro-indenter in order to determinate the global Vicker's hardness and second, the hardness is measured by nano-indentation with a Berkovich tip (see Figure 2.7 (b)).

The advantage of the Vicker's hardness test is that the calculations required to determine the hardness are independent from the size of the indenter. Another advantage is that a Vickers indenter can be used on all kind of materials. The aim of this test is to indent the polished surface of a sample with a pyramidal diamond indenter that will leave an imprint of the form of a square on the surface. By measuring the two diagonals of the square and knowing the force applied during the test, the hardness is computed using equation 2.5:

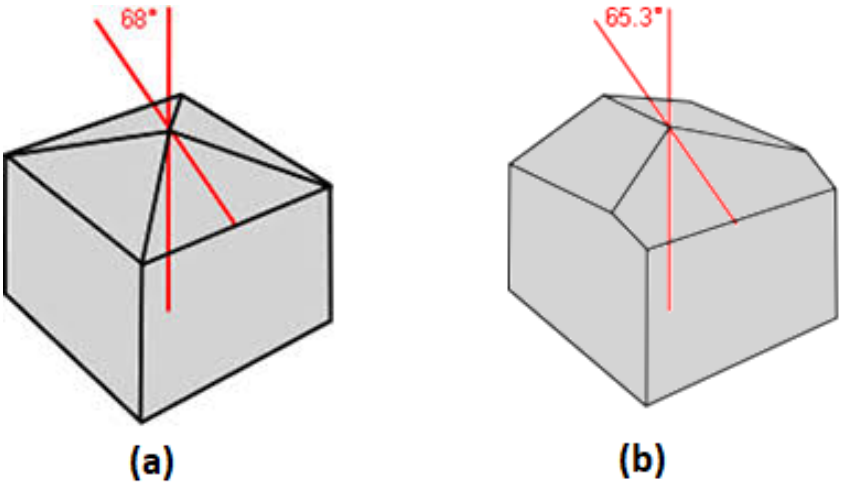

Figure 2.7: Tip used for (a) Vicker's hardness test, (b) Berkovich hardness test [GK18]

$$HV = 1.8544 \frac{F}{d^2} [kgf/mm^2] \tag{2.5}$$

with F, the force applied on the sample by the indenter and d, the average of the two diagonals of the square [CM99]. The coefficient 1.8544 depends on the semi-angle of the Vickers tip.

Berkovich hardness is different from the Vicker's hardness with respect to the tip used to indent the surface of the sample. The first difference is the characteristic size of the imprint made by the tip at the surface of the sample, which is in the order of magnitude of several dozens micrometers for the Vickers tip and from tens to hundreds of nanometres for the Berkovich tip. The shape of the tip is also different, as shown on Figure 2.7.

The Berkovich tip is a three-sided pyramid with the angle between a face and the centerline of 65.3° (Figure 2.7(b)) while the Vickers tip is four-sided pyramid with an angle of 68° (Figure 2.7(a)).

The hardness H, measured y Berkovich indentation is given at the Equation 2.6.

$$H = \frac{P_{max}}{A} \tag{2.6}$$

Where P_{max} is the maximal load and A is the projection of the contact area reached at maximum load. The load/displacement curve is obtained from this kind of test, as well as a typical curve shown on Figure 2.9. The contact area and the load are a function of the penetration depth of the tip. For the loading curve, its evolution as a function of the displacement follows a perfect quadratic polynomial [LGS$^+$96]. The stiffness of the sample indent can also be determined following Equation 2.7 during the unloading.

$$S = \frac{dP}{dh} \tag{2.7}$$

In the first case, the indents are bigger than the typical grain size while in the second case, they are smaller. The hardness measured in the second case is then the local hardness of one grain, i.e. the hardness for pure Cr_2AlC.

Eleven micro-indents were achieved by applying a force of 500g on the surface of the sample with the Vickers tip. The force was applied for 10 sec before it was realized. Using Equation 2.5 after having measured the two diagonals, the global Vicker's hardness of the material is obtained.

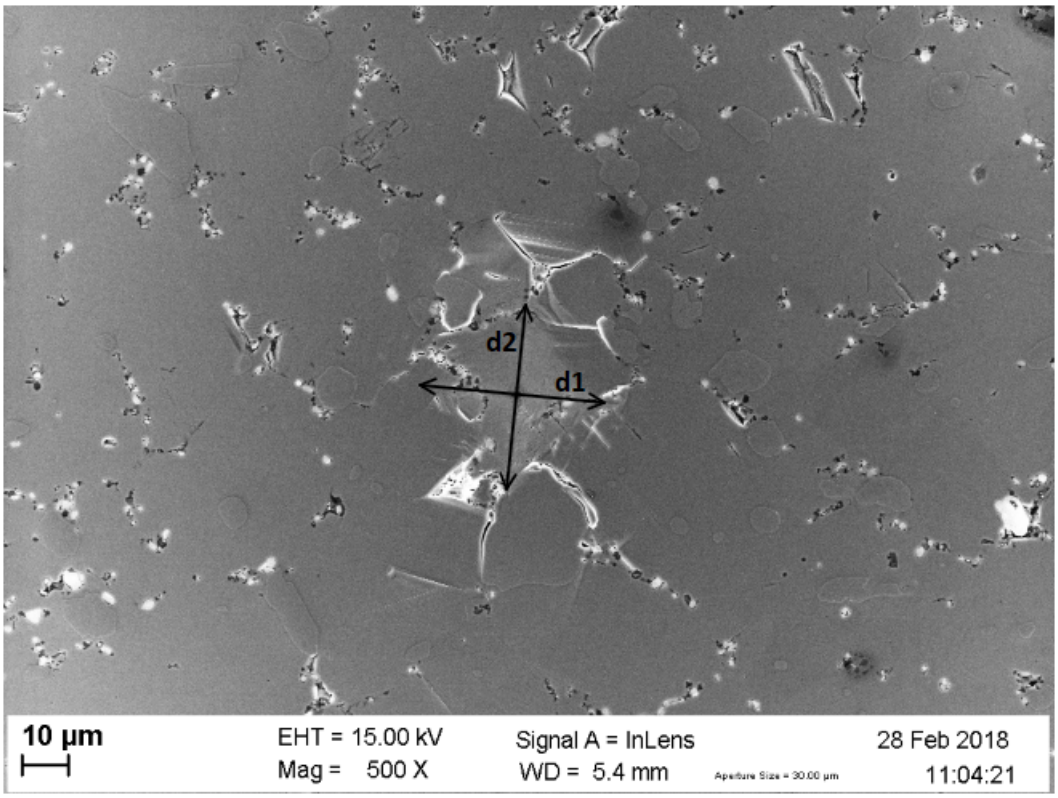

Figure 2.8: SEM image of Vickers indent on the surface of a sample of Cr_2AlC, d1 and d2 are the two diagonals of the square print on the surface used to determine the mean d, used in the equation 2.5

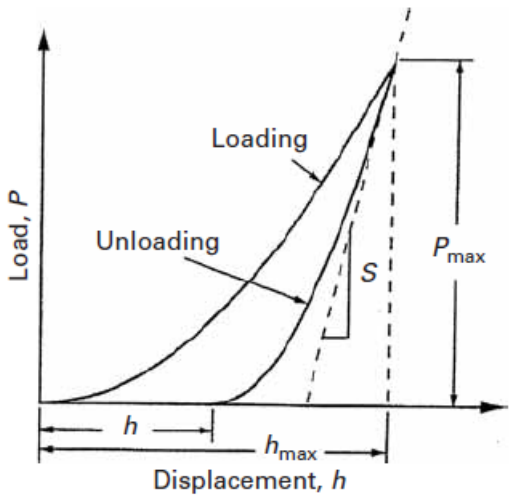

Figure 2.9: Typical load/displacement curve of a Berkovich indentation [CM99]

These indents have been performed on the sample sintered at 1400°C. For the nano-indentation, the issue was to perform indents in the grains and try to induce cracks at the corners of the indents. They had to be small enough to remain inside the limits of the grains and to not interfere with them. They also have to be far enough from the impurities and porosities as to not influence the results.

The nano-indents have been performed on the sample sintered at 1200°C and under the same conditions of pressure and heat rate than the sample of the micro-indentation. These indents

have a depth of 500, 400, 300, 200 and 100 nm and are arranged in rows. Ten nano-indents for each depth are performed. Some indents of 1 μm depth have also been done to test the precision of location of the nano-indenter and the behaviour of the material. These deeper indents are also useful to localise the smaller indents because they mark the beginning of each row. The nano-indenter can provide images of the indents as well as the hardness and the load/displacement curve for each of them. The stiffness of the materials are also determined. In order to be certain that the indents will effectively be inside one grain, the maximal depth (h) of one indent is determined according to the grains size (d) following this relation: $h < 1/3d$.

The nano-indenter realises the indents by controlling the force applied on the tip. The programme starts to measure the displacement of the tip when this last one hits the surface of the sample and stops the application of the force when the wanted displacement is reached. An example of the load/displacement curve is shown in Figure 2.10.

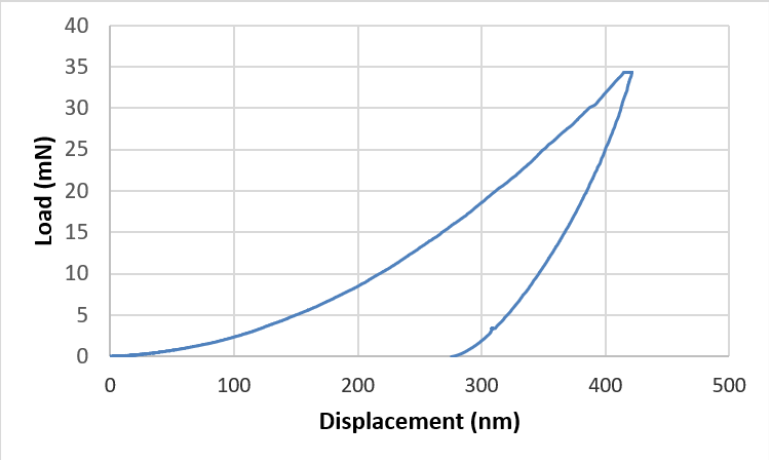

Figure 2.10: Load/displacement curve of a nano-indent deep of 400 performed on the surface of a sample sintered in the reference conditions with a Berkovich tip

Berkovich hardness is measured by the software using Equation 2.6 where the projection contact area (A_p) is determined for the maximal depth (h_{max}) of the tip in the surface of the sample. The area is calculated at Equation 2.8 where C_0 and C_1 are two coefficients which make a correction for the wear of the tip. These coefficients are determined by performing indent on a reference material for which the elastic modulus and the hardness are well known [Wik18e].

$$A_p = C_0 h_{max}^2 + C_1 h_{max} \tag{2.8}$$

2.9 Dilatometre

Tests have been performed with a plasto-dilatometre in order to study the mechanical behaviour of the Cr_2AlC at high temperature. The dilatometre is able to compress the sample and heat it. By controlling the pressure or the displacement applied on the sample, a compression or a creep test is then feasible. These tests have to be realised with the greatest attention because this machine is not designed for these kinds of tests. The coefficient of thermal expansion can also be determined as a function of the heating rate.

The tests are performed under a high vacuum to prevent any oxidation ($5 \cdot 10^{-4}$ mbar), the sample is heated by induction at a rate of 4°C/sec and cooled down with Helium (He) gas injected in the vacuum chamber. The He allows the cooling of the sample and the pressurization of the chamber to the atmosphere. The sample is placed between two pistons in alumina after

the thermocouple has been welded on the sample. It is then compressed with a deformation rate of 0.01 mm/sec. As the specimen is stressed in compression, its geometry is critical to avoid buckling (see Chapter 1). The ratio $h/d \approx 2.0$ is used for the test. Indeed, two macroscopic shapes have been used for the compression tests, a square-base bar with dimension 3x3x8 mm^3 and a cylinder with a height of 8 mm and a diameter of 4 mm. Figure 2.11 shows a schematic representation of the specimen sintered by SPS high of 3 mm (Figure 2.11 (a)) and 8 mm (Figure 2.11 (b)) in dotted lines. The samples used for the compression and creep tests are in continuous line.

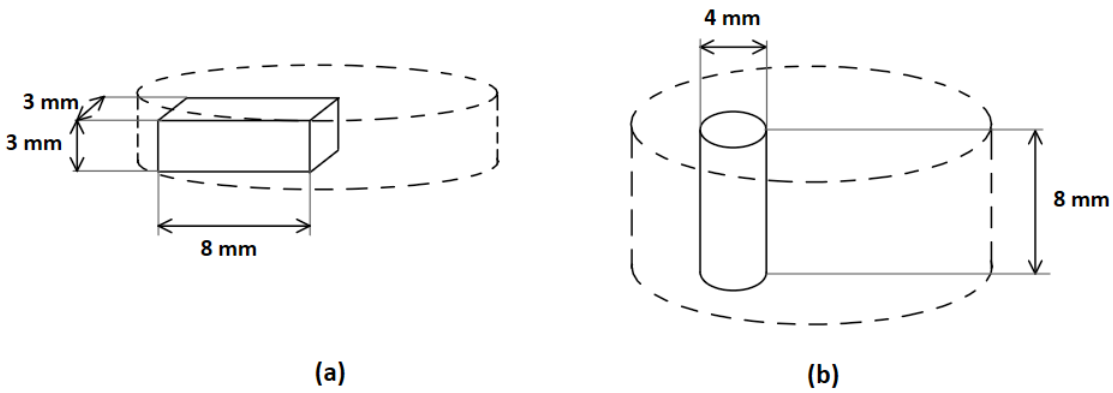

Figure 2.11: Schematic view of the samples used for the compression and creep tests, (a) square-base bar 3x3x8mm^3 cutting from specimens sintered at 1200°C for 5 minutes, with a pressure of 10 MPa and a heating rate of 100°C/min, the bar is cut in the direction perpendicular to the direction of the pressure applied during the sintering process and (b) cylinder 4x8 mm^2 cut in a specimen sintered in the same conditions but high of 8 mm and in the direction parallel to the pressure. The samples cut the compression tests are in full-line while the dotted lines represent the specimen sintered by SPS.

The sample in square-base bar was designed because of the shape of the specimen from the sintering process. Then specimen with a height of 8 mm has been designed to be able to cut cylinder with these dimensions. The two specimens of 3 and 8 mm have been sintered in the same conditions, 1200°C for 5 minutes, under a loading of 10 MPa and with a heating rate of 100°C/min. Their purity, density and microstructure have been compared to check if one of these parameters would induce a significant difference in the mechanical behaviour.

Chapter 3

Results

3.1 Parameters studied

Before presenting the results, the parameters studied are specified. From the synthesis process, the sintering temperature, the loading applied during the process and the heating rate of each sample are studied. The samples sintered under these conditions are compared regarding their density, purity and microstructure. This comparison will demonstrate the impacts of these parameters on the structure of the samples. As said in Chapter 2, two categories of samples have been sintered: first a set of samples with 6g of powder which gives a height of about 3 mm after the process and then samples with 18g of powders so a height of more than 8 mm is obtained after the process. The parameter of the amount of powder used for the sintering process (or the height of the sample) is also studied in this chapter.

One set of conditions has been chosen to study the mechanical behaviour under compression. The conditions are a sintering temperature of 1200°C for 5 minutes, a loading of 10 MPa and a heating rate of 100°C/min. The parameters studied are, for the compression tests, the macroscopic shape of the sample, either a cylinder with a height of 8 mm and a base of a diameter of 4 mm or a square-based bar of dimensions of 3x3x8 mm^3, as said in Chapter 2. The speed and the temperature at which the sample is deformed are also studied.

For the creep test, the macroscopic shape of the sample is also studied as well as the pressure applied to the sample for the creep test and the temperature of this test.

3.2 Texture

Following the sintering process, as the sample is compressed at high temperature, a measure of the texture of the material is realized. Two tests of texture have been performed to identify the symmetry of the samples sintered with 6g of powder. Two symmetries have been tested and the errors on the coefficients measured are presented in Table 3.1.

Pole figure	Error coeff. for triclinic symmetry (%)	Error coeff. for fibre symmetry (%)
002	15.02	1.88
103	27.54	22.06
106	15.02	4.99
109	20.96	2.44

Table 3.1: Comparison of the error on the coefficients measured regarding the coefficients calculated for the triclinic and fibre symmetry

The triclinic symmetry means that no symmetry is present in the material and the fibre symmetry means that one common direction is present for almost each grain in the material. The error coefficients for the fibre symmetry are small enough to assume that the sample possesses this symmetry and the texture measured in this condition is about 8.60. A texture is present in samples of 3 mm high. The measured and calculated pole figures are shown on Figures B.1 and B.2 in Appendix B.

3.3 Densification of Cr_2AlC

According to the method described in Chapter 2 and the equations 2.1, 2.2, 2.3 and 2.4, the closed and the relative density of samples sintered by SPS are determined. The Table 3.2 summarizes the different densities for the condition of sintering studied. A table with the details of the calculation is shown on Figure C.1 in the Appendix C.

Sintering conditions[2]	Relative density (%)	**SD** (%)	Close relative density (%)	**SD** (%)
1200°C	**99.38**	**0.32**	**99.46**	**0.32**
1300°C	97.59	1.45	97.79	1.45
1400°C	98.12	1.18	98.35	1.19
10 MPa	**99.38**	**0.32**	**99.46**	**0.32**
30 MPa	99.60	0.08	99.72	0.08
50 MPa	98.72	1.19	98.87	1.19
50°C/min	98.90	0.20	99.10	0.20
100°C/min	**99.38**	**0.32**	**99.46**	**0.32**
200°C/min	98.27	0.19	98.40	0.19
1200°C, 3 mm	**99.38**	**0.32**	**99.46**	**0.32**
1200°C, 8 mm	96.10	0.10	97.79	0.10

Table 3.2: Summary of the closed and relative density of the different samples studies in this chapter, the sample with the reference conditions is repeated more than once to compare the sintering parameters and in bold text

3.4 Analyse of the microstructure

Due to the variation in the sintering conditions, the microstructure of each sample may be affected. Statistic measurement has been performed with the mean linear intercept method to determine the mean grain size and the proportion of each phase as well as the amount of porosity (see Chapter 2 for the method). XRD and EDX measurement have also been realized to confirm the calculations.

3.4.1 Grain size

First, the mean grain size of each sample has been determined and compared as a function of the sintering conditions. For the parameter "height of the sample", the mean grain sizes are compared in Table 3.3.

[2]The sintering conditions are not all written to make the table clearer, so the missing parameters are the same as for the "reference" conditions, which are, as a reminder, 1200°C, 10 MPa, 100°C/min and 3 mm high, and in bold text in the table.

Height (mm)	Mean grain size (μm)	**SD** (μm)
3	9.61	2.74
8	5.72	1.31

Table 3.3: Results of the mean linear intercept method for the samples sintered with 6 and 18g of powder

For the set of samples with a height of 3 mm, the following graphics show the evolution of the mean grain size as a function of the sintering temperature (Figure 3.1), the pressure (Figure 3.2) and the heating rate (Figure 3.3). The details of the calculations and the statistical sampling are reported at Appendix D in Figures D.1 to D.8.

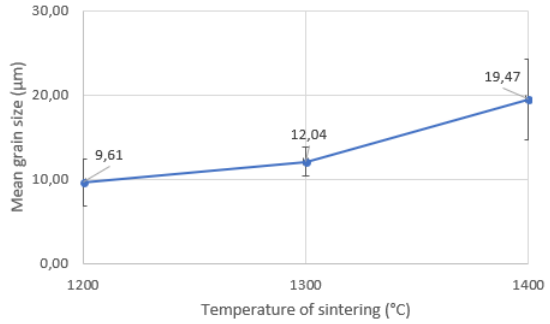

Figure 3.1: Mean grain size of Cr_2AlC sample as a function of the sintering temperature

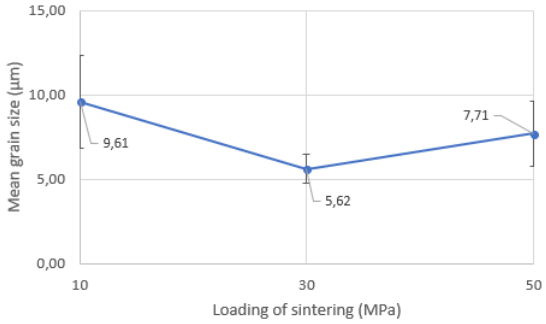

Figure 3.2: Mean grain size of Cr_2AlC sample as a function of the pressure

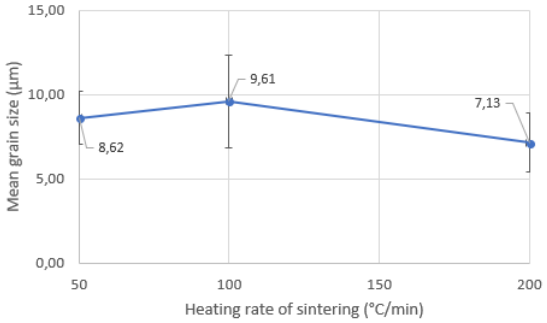

Figure 3.3: Mean grain size of Cr_2AlC sample as a function of the heating rate

3.4.2 Phase proportions

According to the X-ray diffraction (XRD) spectrum of the powder (see Figure 2.1) and the samples (see Figure 3.4 and Figure E.1), the presence of 3 phases is observed, the MAX-phase Cr_2AlC and two phases considered as impurities, chromium carbides $Cr_7C_3/Cr_{23}C_6$ (the main peaks for these two phases overlaid) and alumina Al_2O_3. An analysis by energy dispersive spectroscopy (EDX) confirms the presence of these two phases and also shows a small amount or iron as found with the ICP analyse of the powder (see Chapter 2).

In Figure 3.4, small peaks of carbides and alumina have been identified on sample sintered at 1400°C. The main pic of the alumina located around 43° is covered by the main pic of Cr_2AlC at 42°. The presence of iron is not observed on this analysis. Another XRD analysis is shown on Figure 3.5 for a sample with same sintering conditions excepted for the temperature of sintering, which is at 1200°C.This analysis shows the main peak of the alumina is well distinguished from the main peak of the MAX-phase like on the XRD shown on Figure 2.1.

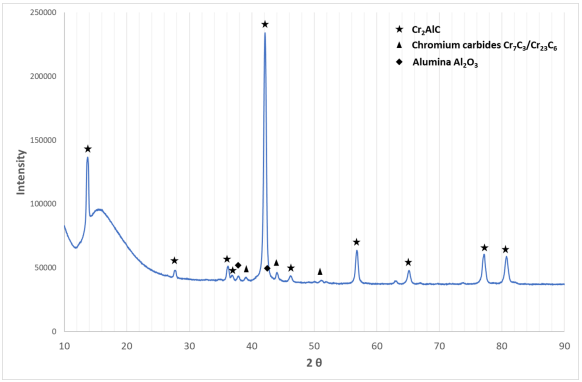

Figure 3.4: XRD spectrum of the sample sintered at 1400°C for 5 minutes, under 10 MPa and with a heating rate of 100°C/min, the spectrum is defined between 10 and 90°. Presence of Cr_23C_6, Cr_7C_3 and Al_2O_3 is confirmed.

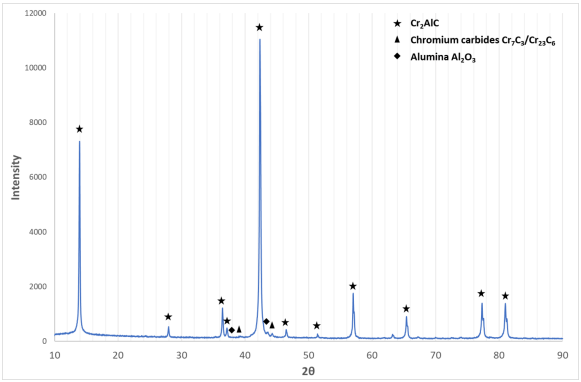

Figure 3.5: XRD spectrum analysis performed on a sample sintered under the reference conditions

EDX analyse is available on the sample sintered at 1400°C. Firstly, the 3 phases observed in XRD are found with this analyse as shown by Figure 3.6 and Table 3.4.

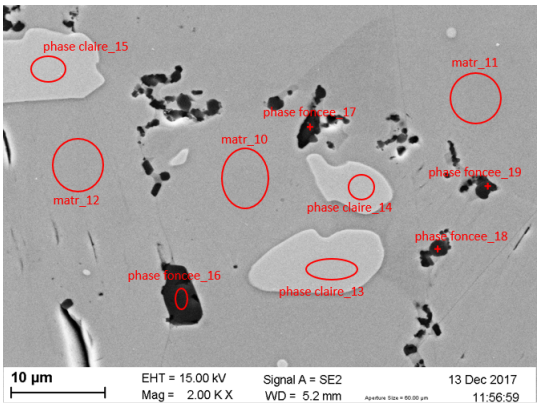

Figure 3.6: SEM image of the sample sintered at 1400°C for 5 minutes, under 10 MPa and with a heating rate of 100°C/min, 3 phases are observed, one darker and one clearer and the matrix, the amount of each phase is shown in Table 3.4

Atomic percent (%)

Spectrum	C	N	O	Al	S	Cr
matr_ 10	23.46	0.51	2.65	23.11	-	50.27
matr_ 11	23.77	0.00	2.69	22.61	-	50.94
matr_ 12	23.61	0.25	2.28	24.02	-	49.84
phase claire_ 13	27.92	0.00	3.77	1.23	-	67.09
phase claire_ 14	28.54	0.00	3.52	1.21	-	66.73
phase claire_ 15	28.45	0.06	3.88	1.00	-	66.61
phase foncee_ 16	3.97	0.98	56.59	37.98	-	0.48
phase foncee_ 17	11.21	32.67	9.94	44.68	0.21	1.30
phase foncee_ 18	7.29	0.97	53.19	35.16	-	3.39
phase foncee_ 19	9.28	1.90	51.15	35.24	-	2.44

Table 3.4: Atomic percent of the proportion of different components present in the phases shown in Figure 3.6

According to the atomic percentage obtained from Table 3.4, the clearer phase is the chromium carbide and the proportion of chrome and carbon are close to the composition of Cr_7C_3. The darker phase contains a higher amount of aluminium and oxygen than the other phases, so it is supposed that it is the alumina Al_2O_3. The atomic percentage of Al and O confirms that. The MAX-phase is the matrix as show the proportions in the table.

The iron has been observed in the sample sintered at 1400°C but in very small quantity. Another EDX analyse has been performed on the sample sintered in the reference conditions. It results that the iron formed a cluster who looks like a eutectic phase (see Figure 3.7 and Table 3.5) which contains the same amount of iron than in the sample sintered at 1400°C. The iron is only observed in these clusters.

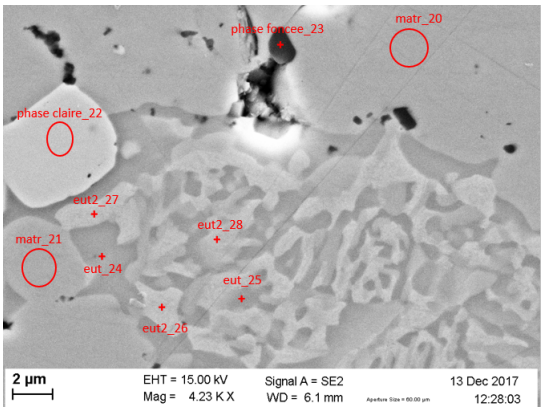

Figure 3.7: SEM image of the sample sintered at 1200°C for 5 minutes, under 10 MPa and with a heating rate of 100°C/min, the iron is observed in the shape of a phase that looks like a eutectic compound

Atomic percent (%)

Spectrum	C	O	Al	Cr	Fe
matr_ 20	24.53	3.40	22.52	49.56	-
matr_ 21	24.24	2.08	24.29	49.39	-
phase claire_ 22	27.13	3.49	0.59	68.78	-
phase foncee_ 23	5.88	53.42	36.35	4.36	-
eut_ 24	8.06	2.46	39.45	48.13	1.90
eut_ 25	11.55	2.25	40.06	44.16	1.98
eut2_ 26	8.98	3.75	32.19	52.89	2.19
eut2_ 27	9.23	3.16	32.71	52.25	2.66
eut2_ 28	9.19	2.81	33.81	52.47	1.72

Table 3.5: Atomic percent of the amount of components present in the different phases shown in Figure 3.6

The amount of each phase in the samples (except the phase with the iron, which is present in too small amount) are computed with the mean linear intercept method and summarized in the Table 3.6. The details of the calculations and the distinguished amount of carbide and alumina are available in Appendix D.

Sintering conditions				Proportions (%)					
Temperature (°C)	Pressure (MPa)	Heating rate (°C/min)	Height of the sample (mm)	Cr2AlC		Imputities (Cr7C3 + Al2O3)		Porosity	
				Mean	SD	Mean	SD	Mean	SD
1400	10	100	3	87,73	5,28	11,93	4,72	0,34	0,27
1300	10	100	3	84,97	4,84	7,04	5,13	7,98	3,01
1200	10	100	3	87,57	1,16	5,31	1,47	7,12	2,34
1200	30	100	3	92,09	1,42	2,39	0,60	5,52	1,15
1200	50	100	3	84,86	7,25	8,90	6,89	6,25	4,47
1200	10	50	3	85,37	9,98	6,69	2,81	7,93	4,91
1200	10	200	3	91,16	6,80	5,04	1,17	3,81	2,78
1200	10	100	8	87,08	3,85	8,72	6,19	4,20	2,33

Table 3.6: Summary of the amount of the different phases and the porosity in samples for the different sintering conditions studies

3.5 Damage under indentation

The indentations realized at the microscopic scale give a global measure of the Vicker's hardness while the local hardness is measured by nanoindentation of Berkovich hardness on pure grains of Cr_2AlC. Table 3.7 summarizes the hardness measured with the two methods.

Method	Hardness (GPa)	Standard deviation (GPa)
Vicker	5.4	0.2
Berkovich	10.1	1.9

Table 3.7: Summary of the hardness calculated with two methods, a micro Vicker's hardness and a nano Berkovich hardness

Images of a micro- and a nano-indent are shown on Figures 3.8 and 3.9 were performed on sample sintered at 1400 and at 1200°C, respectively, with other sintering conditions that are the

same as the reference. Damage is observed around the marks let by the indenter. The mechanism of damaging is described in the next chapter. It can however be noticed that the damaging looks very different for a Vicker or a Berkovich indent.

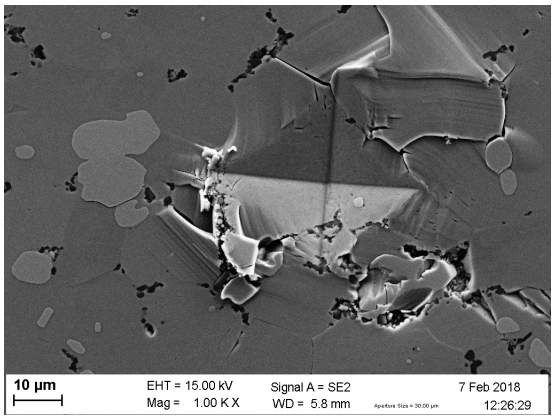

Figure 3.8: SEM image of a Vicker indent realized with a force applied on the tip of 500g for 10 seconds on the sample sintered in the reference conditions except for the temperature of sintering that have reached 1400°C

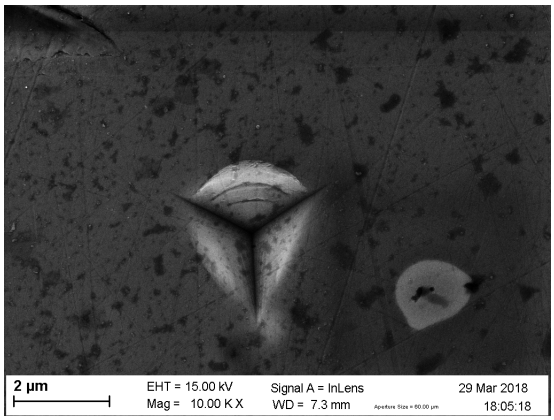

Figure 3.9: SEM image of a Berkovich indent with a depth of 500 nm realized on a sample sintered under the reference conditions

Berkovich indents of 1 μm depth are performed to test the precision of the nano-indenter. One of them is shown on Figure 3.10. This indent has been made on the surface of the sample previously marked with a permanent marker which can explain the contrast noticed on the figure. The clearest part in the centre of the indent is the surface that has been penetrated by the tip. The part of the mark extends from the clearest zone towards the damage zone and is darker because it is the surface initially painted with the marker and pressed by the tip. A start of small cracks appeared at the three corners of the indent. The damage around the indent seems to be overlapping of layers of the materials due to the stress field caused by the Berkovich tip. This damage seems to be an extension of the damage observed in Figure 3.9. But, it is very different from damage caused by the Vicker's tip.

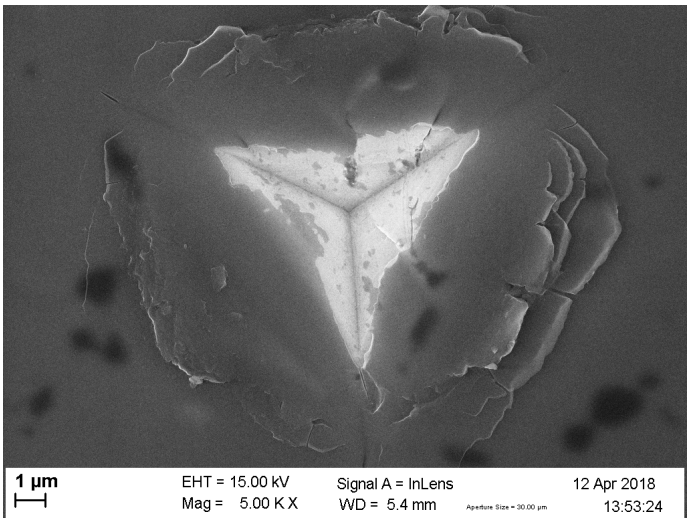

Figure 3.10: SEM image of a Berkovich indent with a depth of 1μm realized on a sample sintered at 1400°C and with others sintered parameters following the reference conditions, the contrast is due to the permanent marker

One interesting point of this image is the contrast between the zone where the tip penetrates the surface the sample and the zone where the tip deforms the surface.

The load/displacement curves resulting from the Berkovich hardness tests depth of 400 nm are presented in Figure 3.11. Discontinuities during the loading are observed on the majority of the curves but not all. The seventh and eighth curves reach a maximum loading of 35 mN without discontinuities. These plateaux are related to the damage caused by the test around the indent (see Chapter 4). The curves obtained for the indents depth of 100, 200, 300 and 500 nm are shown in Figures F.1 to F.4 in Appendix F. It is observed that the curves 7 and 8 in Figure 3.11 show no discontinuities and the curve 6 shows only one small discontinuities. These curves show also a higher amount of load that is needed to reach the wanted depth of 400 nm. This observation will be discussed in Chapter 4.

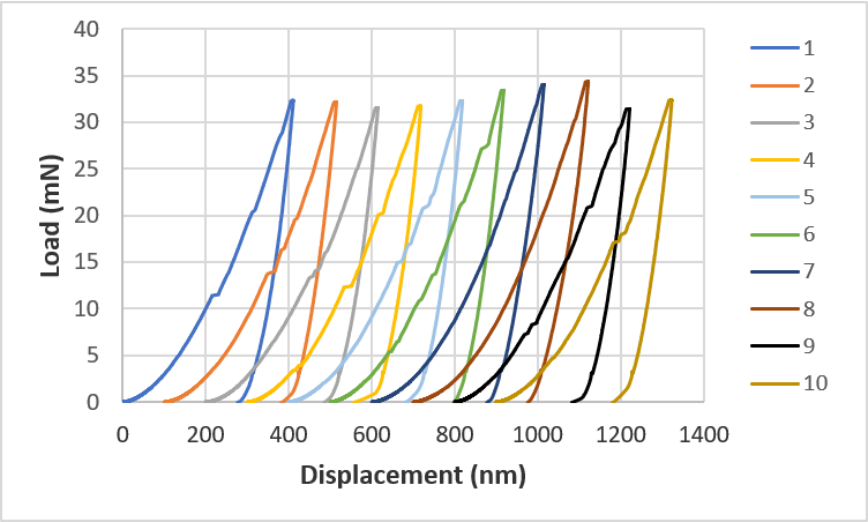

Figure 3.11: Load/displacement curves of the 10 Berkovich indents performed at a depth of 400 nm, the curves are shifted to 100 nm to see them distinctly

Using the unloading curves, the Young's modulus of the sample has been determined and as the mean of the fifty tests, E = 286 (± 14.0) GPa.

3.6 Behaviour in compression

The tests achieved on the plasto-dilatometre provide curves of the displacement and the temperature as a function of the time of the process. These curves can provide informations such as the linear thermal expansion coefficient, stress/strain curves, compressive strength, etc.

The thermal expansion coefficient can be calculated with the definition of the internal energy (U) as a function of the temperature, the volume of the sample and the pressure, $U(T, V, p)$. For very small variation of the internal energy of a system the following equation is defined.

$$dU = \left(\frac{\partial U}{\partial T}\right)_V dT + \left(\frac{\partial U}{\partial V}\right)_T dV \tag{3.1}$$

Where $\left(\frac{\partial U}{\partial T}\right)_V$ is the heat capacity for a constant volume. If, now, this change appends for constant pressure, Equation 3.2 can be defined, and changed in Equation 3.3.

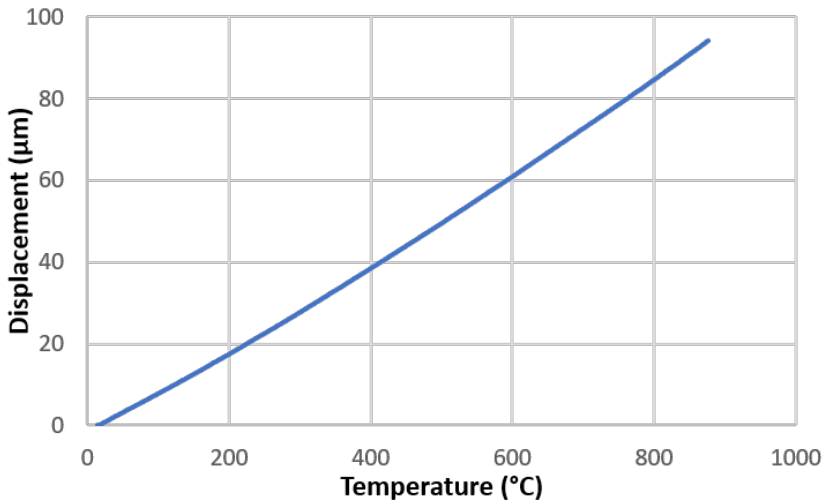

Figure 3.12: Displacement of a square-based bar sample and evolution as a function of its temperature, the heating rate used is 4°C/sec

$$\left(\frac{\partial U}{\partial T}\right)_p = C_V(T) + \left(\frac{\partial U}{\partial V}\right)_T \left(\frac{\partial V}{\partial T}\right)_p \tag{3.2}$$

$$\left(\frac{\partial U}{\partial T}\right)_p = C_V(T) + \beta V \left(\frac{\partial U}{\partial V}\right)_T \tag{3.3}$$

Where β is the coefficient of thermal expansion of the system. The linear thermal expansion coefficient (α_L) has to be determined, as a first approximation, the change of length of a material is related to the change of temperature by α_L. So, the definition is written at Equation 3.4.

$$\alpha_L = \frac{1}{L}\left(\frac{dL}{dT}\right) \tag{3.4}$$

This definition is available for small change of temperature and if no phase transition occurs during this range of temperature [Wik18g]. According to the equations below and the Figure 3.12, the coefficient α_L is computed and summarized in Table 3.8 to make a comparison with literature and other well-known materials. The coefficient α_L is also determined at 800°C and it is equal to 13.55 $\cdot 10^{-6}$ K^{-1}, so it decreases when the temperature increases. The star (*) is used to highlight the difference between the compound calculated and the compound found in the literature for Cr_2AlC.

Materials	α_L at 20°C (10^{-6} K^{-1})
Cr_2AlC	14.06
Cr_2AlC*	12.8(5)
Glass	8.5
Silicon Carbide	2.77
Aluminium	23.1
Magnesium	26
Steel	11.0 − 13.0

Table 3.8: Linear thermal expansion coefficient for different materials, the values of α_L comes from reference [Wik18g], excepted for α_L of Cr_2AlC* that comes from [SAL+09]

Compression tests have been achieved on square-based bar samples at 800 and 1000°C in the plasto-dilatometre. Figure 3.13 shows the stress/strain curve of these tests. The compressive strength is double for the test at 800°C, about 700 MPa, while it is about 350 MPa for the sample compressed at 1000°C. However, the ductility of the same sample at 1000°C seems huge (almost 20 %) compared to that of the sample compressed at 800°C (around 2-3 %). The oscillations observed on the curve for the tests at 1000°C are due to a bad thermal contact between the pistons in alumina and the sample which induced a weak heat transfer and therefore a poor control of the temperature. For the other tests, the contact was better and so the regulation of the temperature.

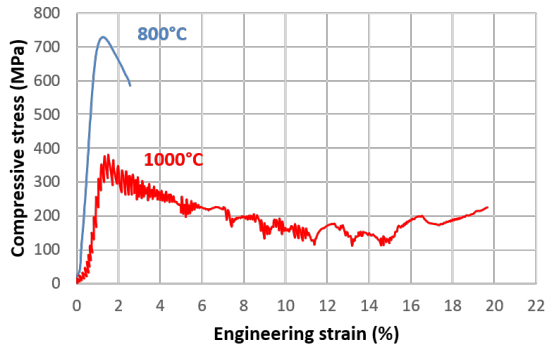

Figure 3.13: Stress/strain of compression tests performed on samples sintered in the references conditions in the shape of a square-based bar and compressed at 800 and 1000°C

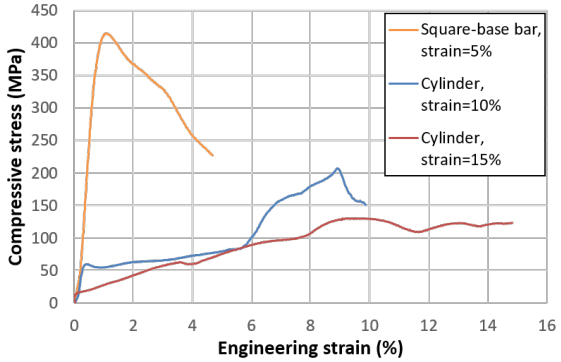

Figure 3.14: Stress/strain curves of the compression tests performed at 1000°C until a global deformation of 5, 10 and 15 %, the sample deformed until 5 % is a square-based bar sample and the two others are cylinders

As show the curve in Figure 3.13, the behaviour of the Cr_2AlC is very different in compression as a function of the temperature. While the sample at 800°C fracture in globally a brittle manner with a fracture plane at approximately 45° with respect to the direction of loading (Figure 3.16), the sample compressed at 1000°C shows an uncommon final shape (Figure 3.15). It means that it does not break in two distinguished parts even after a strain of 20 %. To understand the mechanism of deformation observed on this sample, several tests are performed in the same conditions but with a final engineering strain of 5, 10 and 15 %. The tests deformed at 10 and 15 % are realized on samples with a cylinder shape, while the test at 5 % is achieved on a square-based bar sample as for the sample in Figure 3.15.

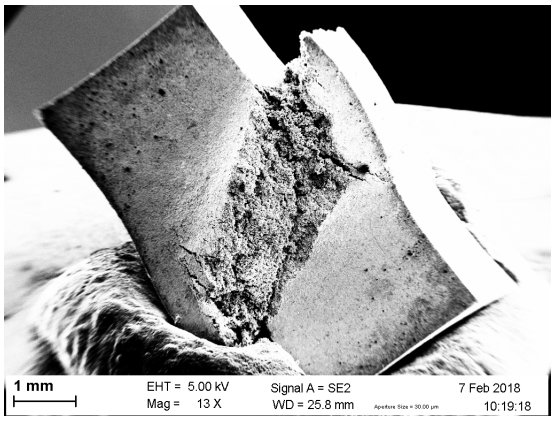

Figure 3.15: SEM image of the macroscopic shape of the square-based bar sample compressed at 1000°C

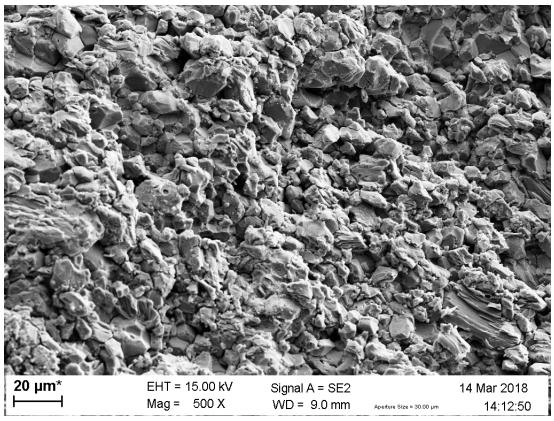

Figure 3.16: SEM image of the fracture surface of the square-based sample compressed at 800°C

These three compression tests give stress/strain curves as presented on Figure 3.14. The compressive strength of the two cylinders are about 50 MPa for the sample deformed at 10 % and about 20 MPa for the sample at 15 %. Even if the yield strength is very different the macroscopic shape of the three compressed samples seems progressively turned into a spindle-like shape. Figure 3.17 shows a cross-section of samples compressed at 5, 10 and 15 % strain after a cut in their middle. The cracks observed on Figure 3.17 (a), (b) and (c) are due to the cutting process with the micro-chainsaw and the diamond disc during the polishing process.

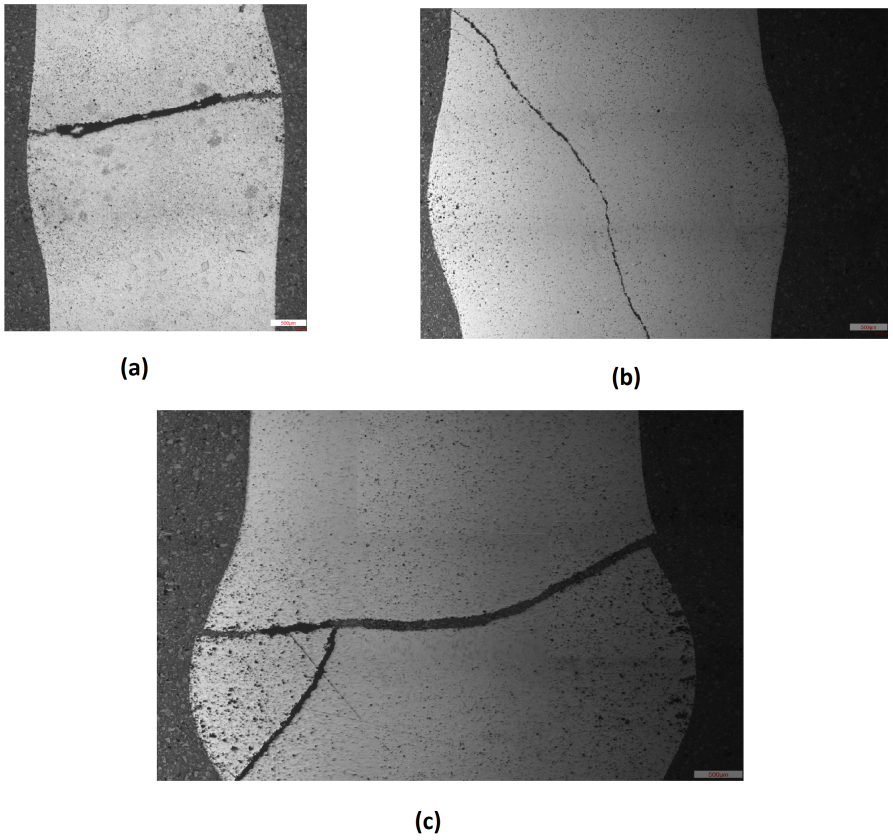

Figure 3.17: Optical images of the cross-section of (a) square-based bar sample deformed at 5 % and (b) and (c) cylinder deformed at 10 and 15 %, respectively

3.7 Creep of Cr_2AlC

After some tests in compression, creep tests in compression have been performed on samples of Cr_2AlC. A first creep test is realized on a sample sintered at 1400°C to check if the sample indeed creep. The creep curve of this test is shown on Figure 3.18. This sample has been creeped at 1000°C and under about 100 MPa. The primary and secondary creep are observed but the test has been stopped before the tertiary creep begins. The primary creep quickly deforms the sample until almost 2 % and the secondary creep begins where the strain evolves in a linear way as a function of time. A second test is achieved on a sample sintered under the reference conditions with the same creep conditions. The load is maintained until the tertiary creep appears to confirm the literature (see Chapter 1). The slope of the steady-state creep ($\dot{\epsilon}_{ss}$) are for the sample sintered at 1400 and 1200°C, $9.5{\cdot}10^{-5}$ and $1.4{\cdot}10^{-4}$ s^{-1}, respectively.

Two other creep tests have been realized on cylinder samples at 1000°C but under a loading of 50MPa. The results are shown on Figures 3.20 and 3.21. The two samples give the same final shape but one has lost the broke parts while the other keeps them attached.

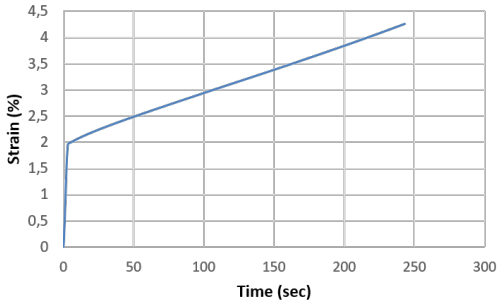

Figure 3.18: Creep curve in compression of the sample sintered at 1400°C while other sintering conditions respect the reference conditions, the creep is performed at 1000°C and under about 100MPa

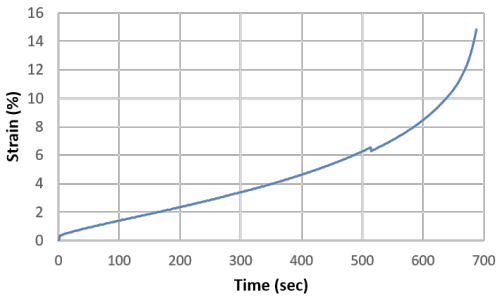

Figure 3.19: Creep curve in compression of the sample sintered under the reference conditions, the creep is performed at 1000°C and under 100MPa

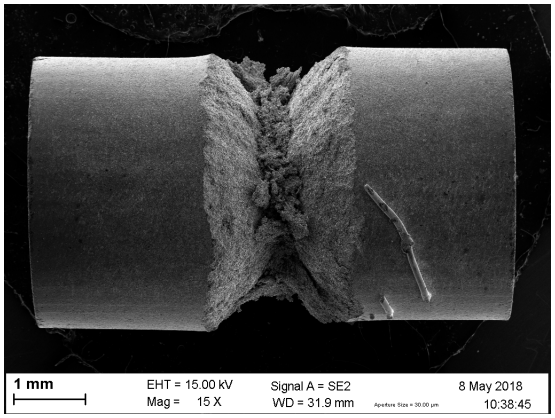

Figure 3.20: Macroscopic shape of a cylinder sample after a creep test at 1000°C under 50MPa, the broken parts are removed from the remaining cylinder

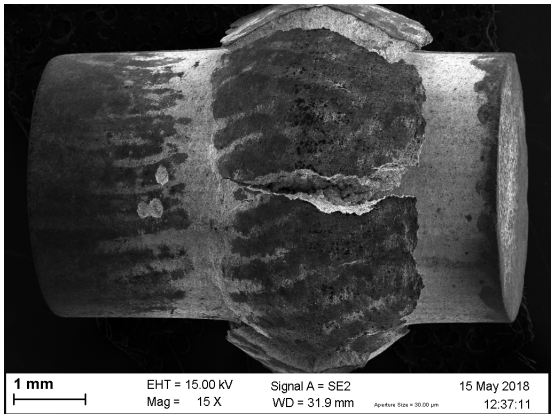

Figure 3.21: Macroscopic shape of a cylinder sample after a second creep test under the same conditions as Figure 3.20, the spindle-like shape after deformation is easily observed

All these results are studied in the next chapter with more details. Comparison with literature and models proposed by researchers are achieved to highlight the mechanism that allowed to obtain these results. Some conclusions can be drawn but other questions remain without answers.

Chapter 4

Discussion

In this chapter, an analyse of the microstructure is first performed to identify the best sintering conditions which lead to a fine grain size as well as a pure and fully dense MAX-phase. Next, the behaviour of the samples of Cr_2AlC at room temperature is studied as a function of the conditions and parameters studied in this report. At high temperature, the material Cr_2AlC has another behaviour. That will be covered in the end of this chapter and compared with the behaviour at room temperature.

4.1 Analyse of the microstructure

According to the results presented in the previous chapters, the microstructure of the samples of Cr_2AlC as a function of the sintering conditions have been identified. As a reminder, reference conditions have been chosen (Chapter 2) to be a sintering temperature of 1200°C for 5 min, with a loading of 10 MPa and a heating rate of 100°C/min with 6g of powder. For these conditions, the sample is 99.46(± 0.32) % dense, has a mean grains size d = 9.61(± 2.74) μm and it is composed at 87.57(± 1.16) % of Cr_2AlC, at 5.31(± 1.47) % of impurities (carbides and alumina together) and at 7.12(± 2.34) % of porosity. The amount of porosity measured by the mean linear intercept method is different from those computed with the Archimede principle. This difference is supposed to be caused by the treatment that the surface received before the observation with the SEM. The mean linear intercept method is performed on SEM images, so the surface is cut, polished and etched and all these steps can increase the surface porosity even with the greatest care.

Sintering conditions				Proportions (%)					
Temperature	Pressure	Heating rate	Height of the	Cr2AlC		Imputities (Cr7C3 + Al2O3)		Porosity	
(°C)	(MPa)	(°C/min)	sample (mm)	Mean	SD	Mean	SD	Mean	SD
1200	10	100	3	94,15	1,79	5,31	1,47	0,54	0,32
1300	10	100	3	90,75	6,58	7,04	5,13	2,21	1,45
1400	10	100	3	86,42	5,91	11,93	4,72	1,65	1,19
1200	10	100	3	94,15	1,79	5,31	1,47	0,54	0,32
1200	30	100	3	97,33	0,68	2,39	0,60	0,28	0,08
1200	50	100	3	89,97	8,08	8,90	6,89	1,13	1,19
1200	10	50	3	92,41	3,01	6,69	2,81	0,90	0,20
1200	10	100	3	94,15	1,79	5,31	1,47	0,54	0,32
1200	10	200	3	93,36	1,36	5,04	1,17	1,60	0,19
1200	10	100	3	94,15	1,79	5,31	1,47	0,54	0,32
1200	10	100	8	89,07	6,29	8,72	6,19	2,21	0,10

Table 4.1: Summary of the composition of samples of Cr_2AlC as a function of the sintering conditions

It is supposed that the additional porosity measured with the mean linear intercept method is only due to the pullout of Cr_2AlC grains during the treatments that the surface receives. The measurement obtained for the closed relative density is supposed to be the closest value to the reality. The composition of the sintered sample under the reference conditions then becomes 94.15(± 1.79) % of MAX-phase, 5.31(± 1.47) % of impurities and 0.54(± 0.32) % of closed porosity. These values are obtained by converting the amount of over-porosity into amount of Cr_2AlC. The same conclusion is available for all the sintered samples, and Table 3.6 can be therefore rectified and turn into Table 4.1. From this table, the composition seems affected by three of the four studied conditions, the temperature of sintering, the loading and the amount of powder used in the process.

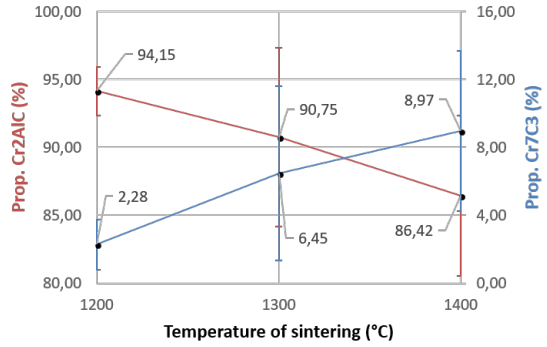

Figure 4.1: Graph of the variation of the carbide and MAX-phase proportion as a function of the temperature of sintering

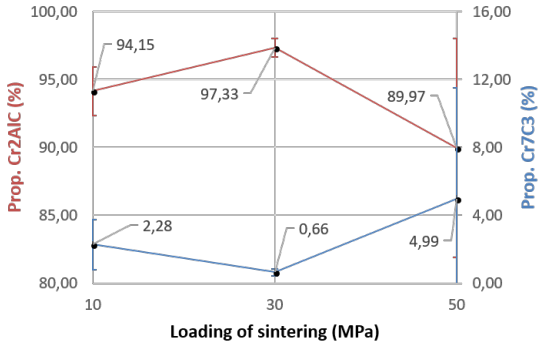

Figure 4.2: Graph of the variation of the carbide and MAX-phase proportion as a function of the loading of sintering

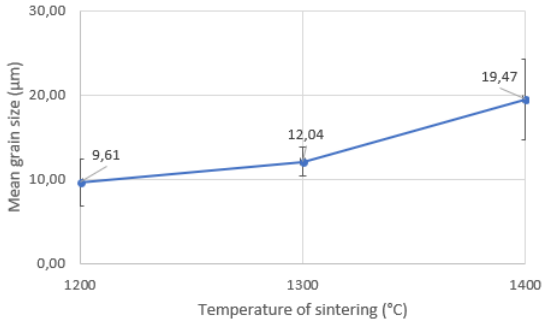

Figure 4.3: Mean grain size of Cr_2AlC sample as a function of the sintering temperature

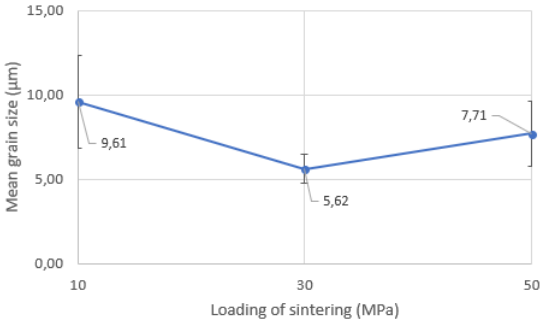

Figure 4.4: Mean grain size of Cr_2AlC sample as a function of the pressure

In summarizing the results obtained from Figures 4.1, 4.2, 4.3, 4.4 and 3.3, the conditions that lead to the finer grain size, the larger proportion of Cr_2AlC and the higher density are a sintering temperature of 1200°C for 5 min and under a loading of 30 MPa. Because the contribution of the heating rate is not obvious, the condition from the reference previously defined can be chosen. Regarding the microstructure of the sample sintered under these conditions (Figure 4.5), with a large amount of porosity, grains of carbides are small and particles of alumina are located in the grain boundaries. Figure 4.6 shows a very different microstructure with bigger grain of Cr_2AlC and Cr_7C_3, less porosity on the surface even after the treatments on the surface and the small particles of alumina seem to have diffusd in the grain boundary like in the sample sintered at 30 MPa but closer to the carbides grains and the porosities.

According to the results of the EDX analysis from Figure 3.7 and Table 3.5, one phase that contains a small amount of iron has been found in the sample. This phase has a higher amount of aluminium than the MAX-phase and a smaller amount of carbon. After etching, this phase

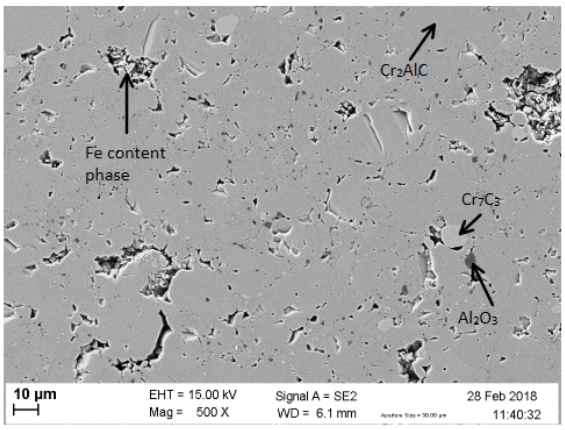

Figure 4.5: SEM image of the polishing and etching surface of the sample of Cr_2AlC sintered under 30MPa and other conditions identical to the reference

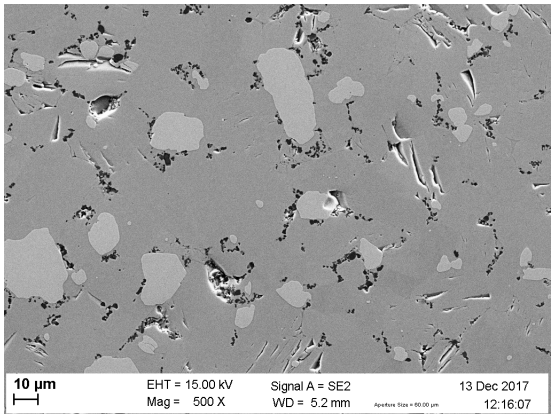

Figure 4.6: SEM image of the polishing, but not etching surface of the sample of Cr_2AlC sintered at 1400°C with other conditions identical to the reference conditions

exhibits a dendritic shape as shown on Figure 4.5 and 4.11. A differential scanning calorimetry (DSC) analysis has been performed on the powder used in the SPS. The result is shown on Figure 4.7 where two peaks are observed at 1252 and 1313°C. The melting point of the powder has been assumed to be around 1500°C. Therefore, something happens around 1400°C but it is not obvious that it can be identified as a peak. As the DSC compares the heat flow required to keep the sample and the reference at the same temperature, these two small peaks mean that a higher amount of heat is needed to maintain the powder at the same temperature than the material of reference. A change in the powder, like a phase transition, occurs at these particular temperatures. It is supposed that phases present in the powder melt at these temperatures, but the two phases identified as chromium carbide and alumina have a melting point far away from these two peaks, around 1780 [PB85] and 2100°C [Wik18a], respectively, and only the dendritic phase containing iron remains. Under the assumption that the results of EDX are influenced by the matrix around due to the size of the phase with a shape of dendrites, this result suggests the formation of stable intermetallic Fe-Al. During the synthesis process of the powder, which initially contained a small amount of iron and pure aluminium, this last diffuses once melted towards the iron and forms rich-Al intermetallic. It then stabilized in FeAl after enough diffusion and time. The binary phase diagram of Fa-Al is shown on Figure 4.8, where two transitions can be observed for the compound FeAl around 1230 and 1310°C. If the composition of iron and aluminium is balanced at 50/50 %, the first transition temperature is rather around 1250°C. The two transition temperature of the FeAl observed correspond to the peaks in the DSC analysis.

The phase with iron seems to be present in the samples sintered at 1200°C contrarily to the sample at 1400°C. It is not exactly the case because Figure 4.9 shows this phase in the sample sintered at 1400°C and its size is compared with the clusters observed in sample sintered under the reference conditions in Figure 4.10.

Again, as observed on Figures 3.7 and 4.11, the phase containing iron seems to be divided into two phases of different compositions. The so-called phase "eut" in Table 3.5 contains a higher amount of Al while the phase "eut2" has a higher amount of Cr. This result is confirmed by the clearer contrast of the phase "eut2" that implies a higher amount of heavy chemical element. From this, it is finally supposed that the clearer phase "eut2" is mainly ferritic steel with Al and Cr in solid solution while the darker phase which contains a higher amount of Al is the intermetallic Fe-Al.

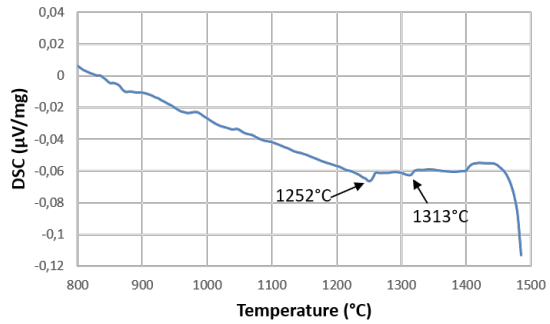

Figure 4.7: Differential scanning calorimetry of the powder of Cr_2AlC used in the SPS with two peaks identify at 1252 and 1313°C and the melting point of the powder at 1500°C

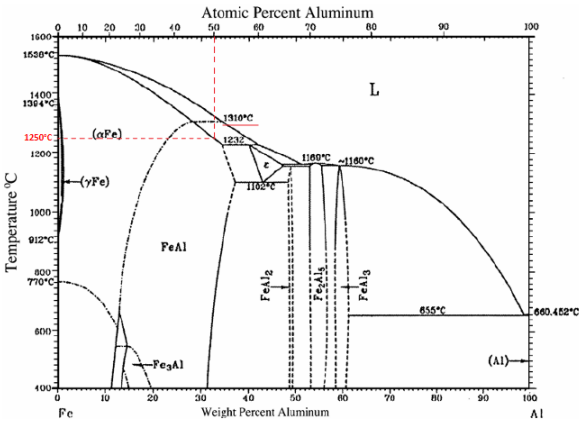

Figure 4.8: Binary phase diagram of Al-Fe with melting temperature for FeAl of 1250 and 1310°C in a composition of 50/50 in % atomic [Hen07]

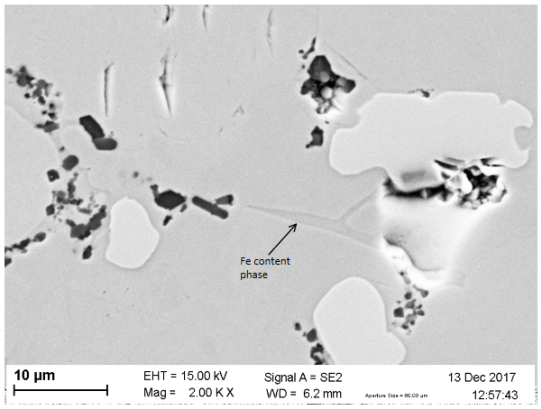

Figure 4.9: SEM image of the polished surface of the sample sintered at 1400°C with other sintering conditions as the reference

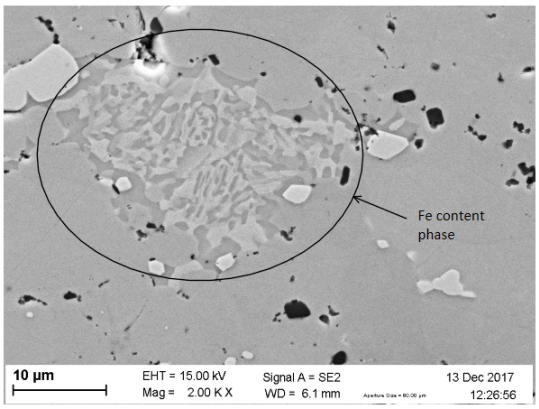

Figure 4.10: SEM image of the polished surface of the sample sintered under the reference conditions

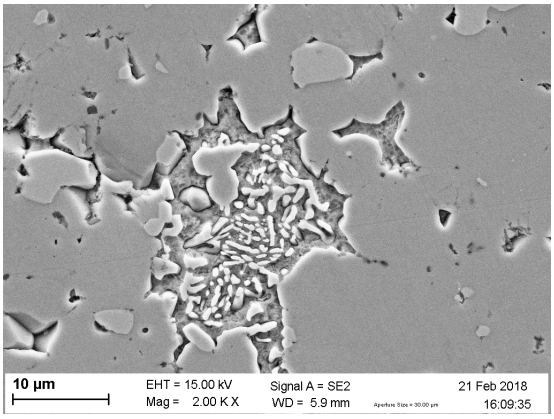

Figure 4.11: SEM image of the phase containing iron of polished and etched surface on sample sintered under reference conditions

4.2 Mechanical behaviour at low temperature

As indicated in Table 3.7, the hardness can be very different with the different methods used (about 5 GPa for the Vicker's hardness and about 10 GPa for the Berkovich hardness). The

measure obtained for the Berkovich hardness is the mean of the hardness calculated for each depth of indents. This difference may be explained by two elements. First, the sintering conditions of samples indent with Vicker and Berkovich indenters are slightly different. As the analyse of the microstructure have shown, the grain sizes of the samples sintered at 1200 and at 1400°C, and with the other conditions like those of the reference, are different. Then, as the Vicker's hardness is performed on the sample with the mean grain size of about 20 μm and the Berkovich hardness on the sample with $\pm$ 10 μm of mean grain size, the measure can be affected. Second, the size of the indent is so different (see Figure 3.8 and Figure 3.9) that the micro-indent of Vicker is bigger than the mean grain size. This implies that the grain boundaries, the porosities and the impurities can impact the measure of the hardness. As the impurities of alumina and carbide are harder than the MAX-phase, the hardness is slightly increased, but due to the high amount of porosity in the surface and due to the grain boundaries, the hardness may decrease. For the nano-indent, it is smaller than the mean grain size which implies that the hardness measured is for pure mono-crystal of Cr_2AlC. Another assumption may be that the size of the indent influences the hardness measured.

As reported in Chapter 1, Duan *et al.* find a Vicker's global hardness for fine-grain samples of Cr_2AlC sintered at 1400°C of 5.3 $\pm$ 0.9 GPa [DSJ$^+$15] which is a good correlation with the result obtained in this work. Duan observed two behaviours of the material under indentation as a function of the microstructure and the direction of the sintering loading. For coarse-grains (about 50-100 μm mean grain size) a plastic deformation zone around and inside the mark let by the indent and not leading to cracks is observed. While for fine-grains (about 1-3 μm mean grain size) cracks appear at the corner of the indent and no plastic deformation zone is noticed (Figure 4.13).

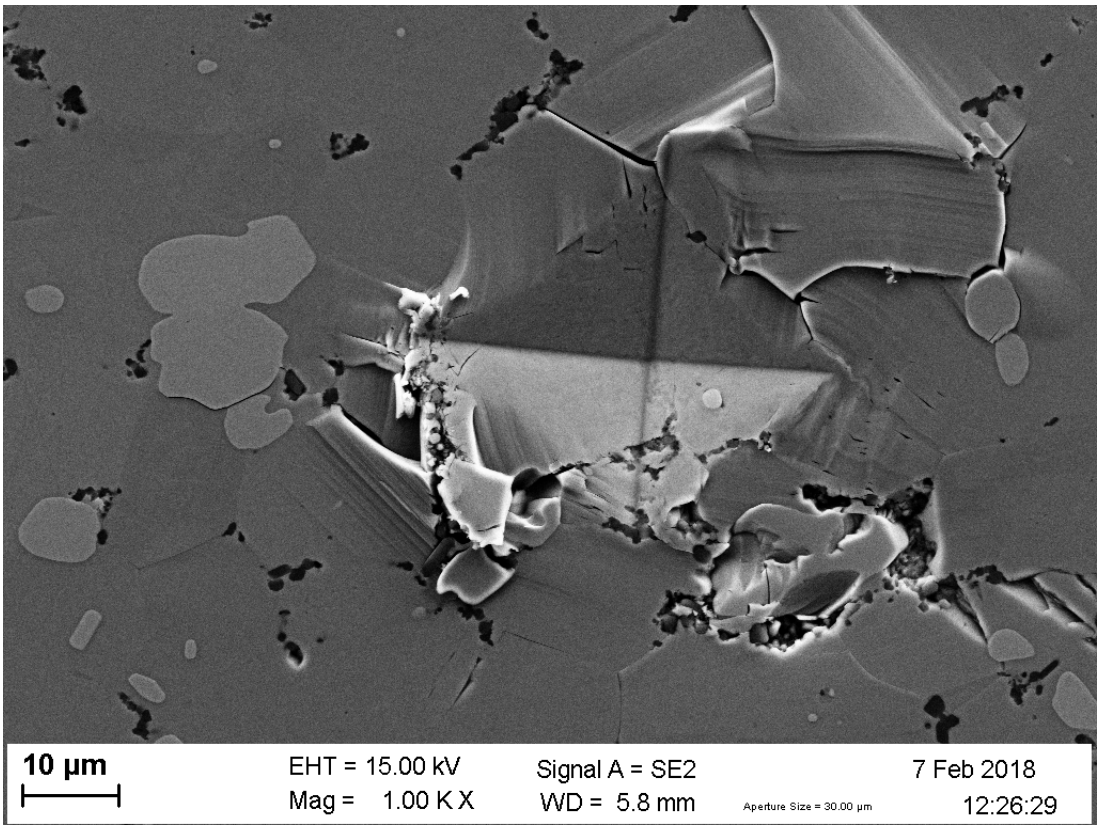

Figure 4.12: SEM image of a Vicker's indent realized with a force applied on the tip of 500g for 10 seconds on the sample sintered in the reference conditions except for the temperature of sintering that have reached 1400°C

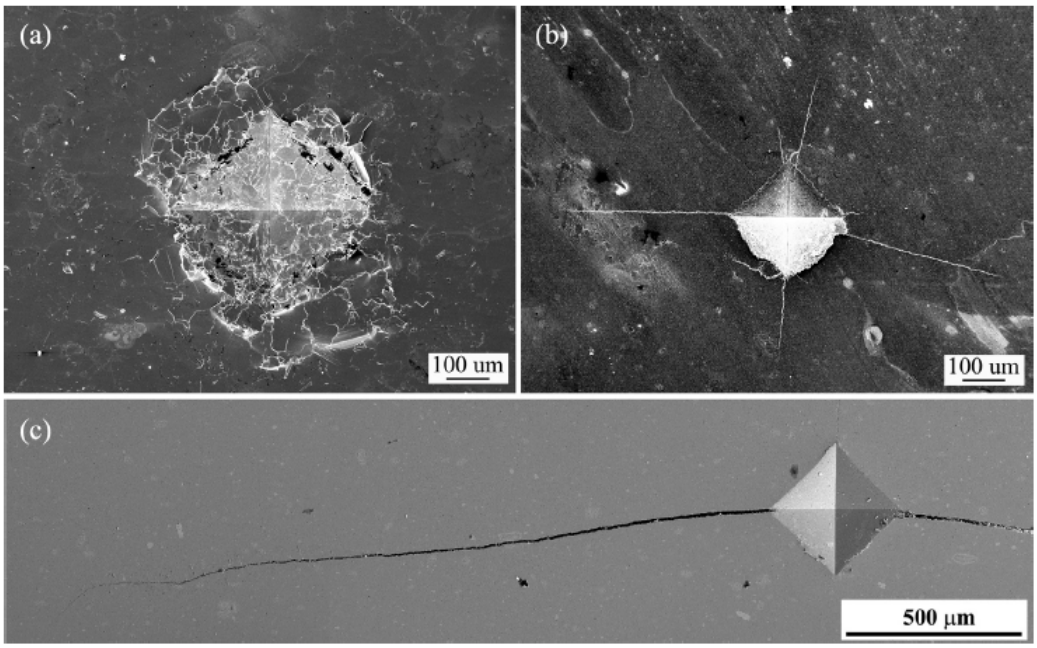

Figure 4.13: SEM image of Vicker's indentation on (a) coarse-grained Cr_2AlC, (b) fine-grained Cr_2AlC surface perpendicular and (c) parallel to the sintering compaction direction [DSJ+15]

In this work, the behaviour observed is in between the coarse- and fine-grains results. As the mean grain size is about 20 μm and the indent has a size of about 40-50 μm, plastic deformation zone is observed around the mark without apparition of cracks (Figure 4.12) as for coarse-grains indentation. The crack at the top of the mark in Figure 4.12 is rather due to the fact that the corner of the indent lies in a grain boundary, which induces its opening. Therefore, the hardness is similar to that obtained for fine-grains microstructure. The deformation mechanism followed a sample with coarse-grains while the hardness measured is very close to that obtained for fine-grains.

Moreover, Figure 4.12 shows clearly well the mechanism of damage observed for the MAX-phase family. Due to the high stress applied by the tip on the surface of the sample, some delamination around the indent is observed (see Figures 4.14 and 4.15). Indeed, the compression induced by the tip of the indenter brings bends and delamination of the grains (example in Figure 3.8, on the right of the mark let by the micro-indent). The inability for the dislocations to move out of the basal slip plans, and the concentration of stress in tension under the tip due to the friction during the indentation induced apparition and growth of cracks either inside the grain (Figure 4.17) or at the grain boundaries (Figure 4.16) without plastic deformation of the grains.

The Berkovich indents realised at different depths present a hardness that evolves with the depth. This evolution is shown on the graph in Figure 4.18 of the hardness as a function of the depth of the indent. As previously said, the hardness is determined using Equation 4.1, where P_{max} is supposed to be square dependent on the displacement as for A_p (see Equation 2.8).

$$H = \frac{P_{max}}{A_p} = \frac{Bh_{max}^2}{C_0 h_{max}^2 + C_1 h_{max}} \tag{4.1}$$

Therefore, as a good approximation, when the displacement is large, the hardness does not depend on the displacement because the term to the square is dominant in Equation 2.8, so it is simplified with the term to the square in the relation of P_{max}. But if the displacement is small, the term to the square is not anymore predominant and the hardness will increase as

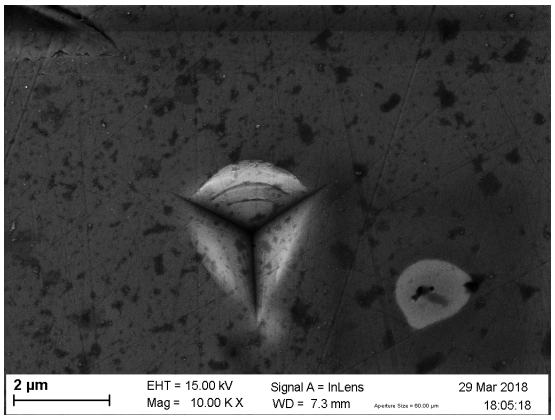

Figure 4.14: SEM image of a Berkovich indent with a depth of 500 nm realized on a sample sintered under the reference conditions

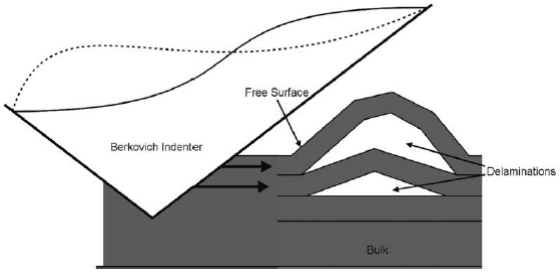

Figure 4.15: Schematic representation of the delamination of lamellae due to high compression stress caused by the tip

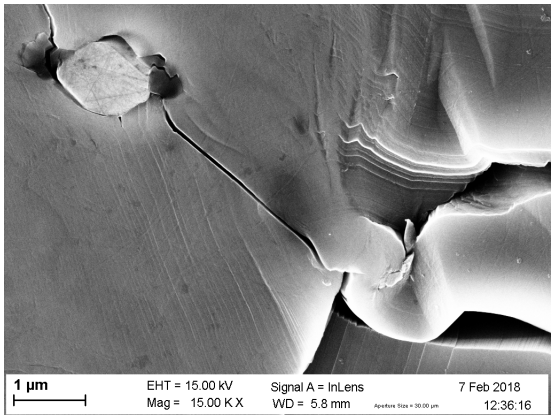

Figure 4.16: Zoom of Figure 3.8, propagation of cracks that nucleate from a particle of carbides (white) and small particles of alumina (black) at the top of the image, observation also of bending and delamination of the structure at the bottom of the image

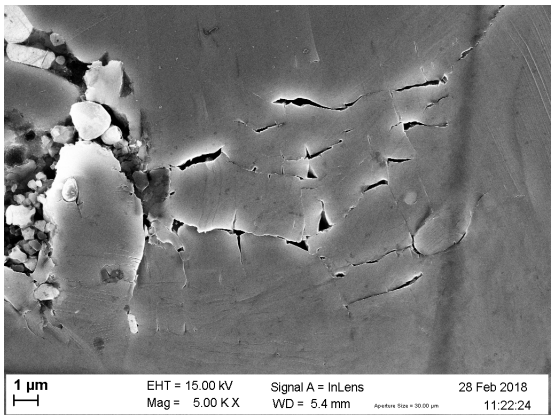

Figure 4.17: Cracks between the lamellae of Cr_2AlC due to the stress in traction in the mark of the indent

the displacement decreases because of the influence of the second term in Equation 2.8. This behaviour is well observed on Figure 4.18.

Figure 4.19 shows the mean value for each depth of the Berkovich and the Vicker's hardness measurements. The linear prevision of the Berkovich hardness as a function of the depth of the indent is represented by the dotted line. It is observed that the Vicker's measurement is far from the prevision. This result confirms the model described above where the dotted line predicts the hardness until a critical depth where the model changes and does not depend anymore on the depth of the indent. To be able to determine this model, more points are needed on this graph.

Around Berkovich indent, damage is observed on the load/displacement curve. This curve may sometimes show discontinuities during the loading, as said in Chapter 3. Because the displacement of the tip is controlled by increasing the force rather than by measuring the displacement, if a crack appears, or some damage nucleates, the tip will quickly go deeper in the materials and gives a plateau as shown on Figure 4.20. It is supposed that the first discontinuity observed on the load/displacement graph is due to the delamination observed at the right of the indent shown

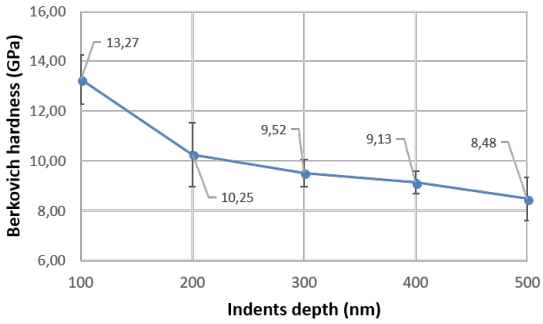

Figure 4.18: Graph of the evolution of the Berkovich hardness as a function of the depth of the indents

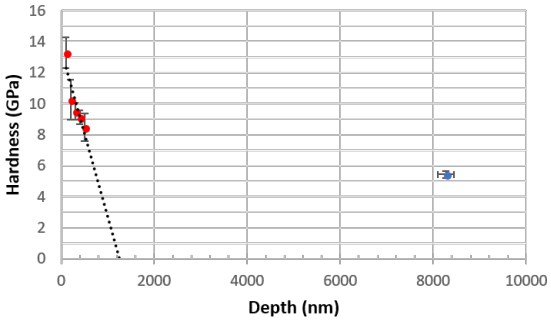

Figure 4.19: Comparison with the hardness measured by Berkovich hardness (red) and Vicker's hardness (blue), each point is the mean of 10 values measured under the same conditions of loading, the dotted line represents the linear prediction of the Berkovich values for higher depth of indents

on Figure 4.21. A second delamination is observed at the left of the mark on Figure 4.21. Indeed, because the delamination is considered as the buckling of the lamellae at the nano-scale, when it appears, the tip will quickly go deeper into the surface which causes these primary plateaux around 15 and 20 mN. A secondary plateau is located above 15 and 20 mN, just after the first one. It can be explained by the re-positioning of the tip after a tilt caused by the right buckling for example. This movement happens because the force applied the tip. When the buckling occurs, the tip tilt because one side of the material realized the internal stresses. In further increase the force on the tip, the left side will catch up the right one and the tip presses again in a symmetric manner until the second delamination.

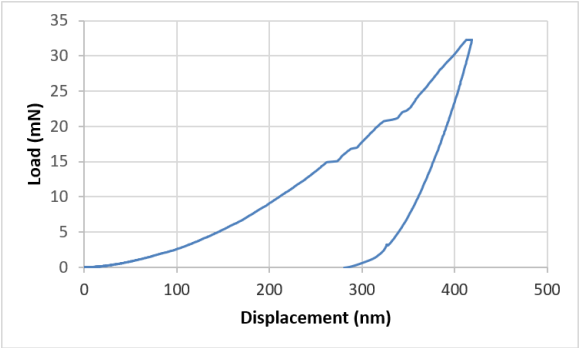

Figure 4.20: Load/displacement curve of the nano-indent deep of 400 nm shown in Figure 4.21 performed on the surface of a sample sintered in the reference conditions with a Berkovich tip

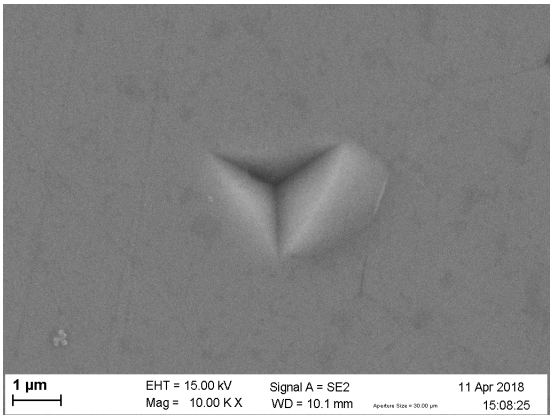

Figure 4.21: SEM image of a Berkovich indent with a depth of 400 nm realized on a sample sintered under the reference conditions

4.3 Mechanical behaviour at high temperature

The sintering conditions used to achieve the mechanical tests at high temperature are a temperature of 1200°C for 5 min, under 10 MPa and with a heating rate of 100°C/min (the reference

conditions described in the beginning of the report). The reason why the sample with optimal microstructure, finer grain size and higher amount of MAX-phase as well as the best densification, is not used for the mechanical tests is because other tests ware already performed on sample sintered under the reference conditions. In order to be able to compare and analyse the conditions of the mechanical tests without the influence of other parameters, the same microstructure for the sample is needed.

The compression tests under 800 and 1000°C are realised on square-based bar, and give different results. First, the sample compressed at 800°C failed in a brittle manner, showing almost no homogeneous plastic deformation. The shape of the sample fracture after the test is shown on Figure 4.22. Second, the sample compressed at 1000°C deformed in a lightning bolt-like shape as shown on Figure 3.15.

Fracture surface of the sample test at 800°C shows two finishing surfaces after the failure first, the grains are well distinguished, it is a rough surface (right in Figure 4.23). Then, part of the same surface seems roughly polished (left in Figure 4.23). This second surface is mainly located at the centre of the fracture surface.

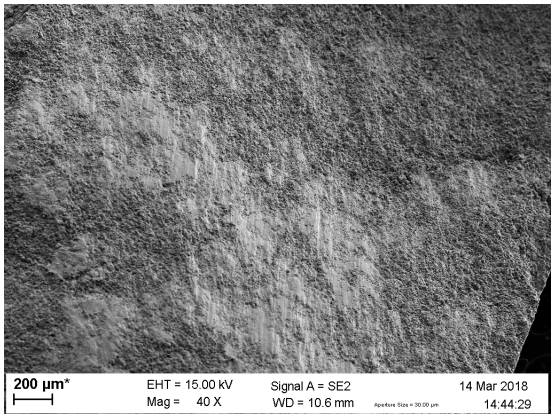

Figure 4.22: SEM image of the fracture surface of the centre of the sample compressed at 800°C

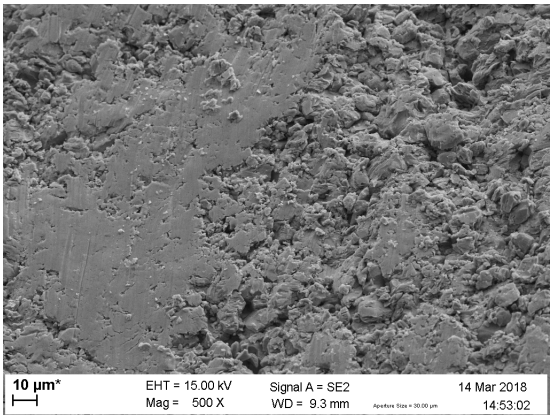

Figure 4.23: Zoom of Figure 4.22

This kind of failure looks the similar to normal fatigue. But the cause of failure is the brinelling phenomenon. It occurs when two hard surfaces have a relative movement one from another. Because at this temperature the fracture that occurs if brittle, the bar will fail by cleavage, and more precisely by basal cleavage due to its crystallographic structure. It means that there is only one cleavage plane and this explains why the fracture surface is oriented at 45° from the loading direction. The fracture surface is represented on Figure 4.24 and the local microstructure is shown with two SEM images taken at different places on the surface.

The surface that seems polished appears during the cleavage when the main failure propagates along the whole sample. The left image on Figure 4.24 that gives an idea of the state of the surface at the top and the bottom of the fracture surface, shows that the predominant failure is an intergranular crack. While the right image on Figure 4.24 lets clearly suppose that the relative movement between the two surfaces, once separated, and the high compressive stress induce a local plastic deformation of the grains crushed together by Hertz contact forces. Another explanation may be simply that the finishing of the surfaces is due to friction. Indeed, as the failure is brittle, the two surfaces are rough. And, because of the relative movement between the two surfaces and their roughness, the grains are smoothed at some location of the surfaces. Figure 4.22 shows lines or scratches. They represent the direction of sliding of the surface and they are parallel to the direction of the slope. These scratches confirm the relative movement between the two surfaces and the following model tries to quantify the amount of local stress

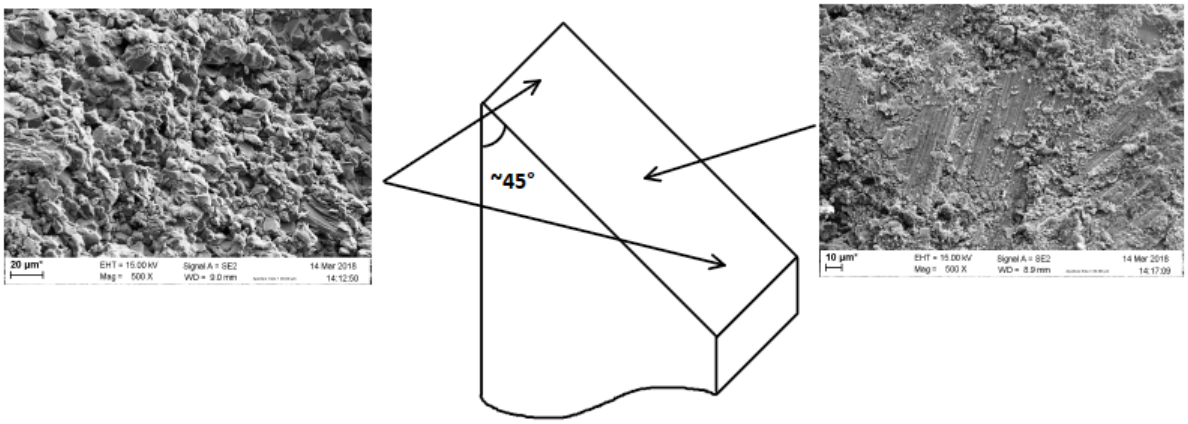

Figure 4.24: Schematic view of the fracture of the sample compressed at 800°C with two SEM images showing the microstructure at different places on the surface, (left) the surface resulting from the main intergranular crack and (right) the brinelling effect observed at the centre of the surface of failure

reach because of this movement.

Under the assumptions that the grains are spherical with a radius that corresponds to the half of the mean grain size (R≈5 μm), and the brinelling effect occurs at the fracture stress (≈600 MPa) which corresponds to a global force (F) of 5400 N. The model of Hertz contact for two spheres in contact is found in reference [Wik18c]. The elastic coefficients E and ν of Cr_2AlC are 286(± 14.0) GPa and 0.25, respectively. The Young's modulus has been determined during the nano-indentation calculation and represents the mean of the values for each depth. With these coefficients, the Young's modulus normalized by the Poisson ratio (E^*) can be computed by Equation 4.2.

$$E^* = \frac{E}{1-\nu^2} \tag{4.2}$$

The contact zone increases with the deformation and becomes a circle with a radius a that is

$$a = \left(\frac{3F}{4}\frac{R}{E^*}\right)^{1/3} \tag{4.3}$$

because the two spheres have the same radius and Young's modulus. The maximal pressure (p_{max}) and the maximal shear stress (τ_{max}) located at the centre of the contact zone are computed using F and a at Equations 4.4 and 4.5.

$$p_{max} = \frac{3F}{2\pi a^2} \tag{4.4}$$

$$\tau_{max} = \frac{p_{max}}{2} \tag{4.5}$$

Eventually, the amount of displacement reached by the grains at the contact is denoted δ and determined at Equation 4.6.

$$\delta = \left(\frac{9}{2R}\left(\frac{F}{E^*}\right)^2\right)^{1/3} \tag{4.6}$$

According to this model, the maximum shear stress sited under the surface at a distance $z = 0.5a$ reached 800 GPa. Due to this high amount of stress at this single point which is larger than the compressive strength, the local plastic deformation of the grains then occurs. This model is only valid under the assumptions made above. They very much simplify the behaviour of the surfaces and the value of the maximum sheer stress is maybe far from the reality.

The stress/strain curves obtained for these two tests can be compared to those found in the literature. Figure 4.25 shows that the behaviour at 800°C reproduces well what is experimented by Tian and his group. But when the parameters used by Tian for the tests are compared with those of this work, the sintering conditions and the strain rate used bring a different mechanical behaviour after the deformation. On the other hand, the sample tested at 1000°C presents an expected behaviour on the curve at 900°C (Figure 4.25). Moreover, the sample tested at 900°C does not fail as the sample deformes at 1000°C. Nevertheless, the final shape of the sample deformed at 900°C looks like a spindle shape [TSHD09] while the sample deformed at 1000°C has a lightning bold-like shape.

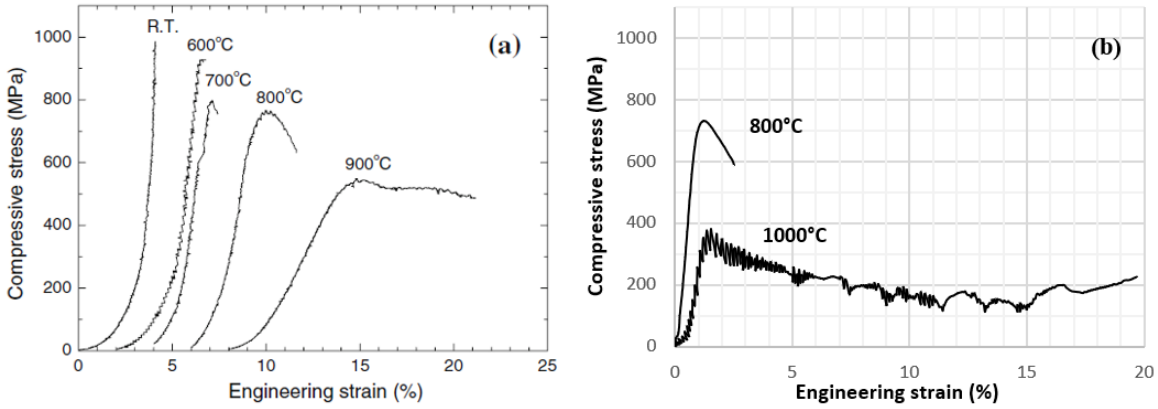

Figure 4.25: (a) Stress/strain curves of samples of Cr_2AlC (dimension of 2.5x2.5x6 mm^3) compressed from room temperature to 900°C, they have been sintered by pulse discharge sintering at 1250°C for 30 min, under 50 MPa and with a heating rate of 50°C/min, the strain rate is $5.6{\cdot}10^{-4}$ s^{-1}, the mean grain size is 6.4 ($\pm$ 2.1) μm [TSHD09], (b) stress/strain curve of samples of Cr_2AlC compressed at 800 and 1000°C for a strain rate of $1.25{\cdot}10^{-3}$ s^{-1}

This spindle shape has been observed on samples tested at 1000°C but when these tests ware stopped at a global engineering strain of 5, 10 and 15 % (Figure 3.17). Assuming that the deformation is the same in all the directions perpendicular to the loading direction, the deformation profile has been determined as a function of the length of the compressed samples and are represented on Figure 4.26. These profiles show that the largest deformation is located at the centre of the length of the samples. They also show that the deformation is localised at the centre while the extremities are almost not deformed. This local deformation begins for very small strain and evolves, without failure of the sample, until a very large strain.

The reason why the local true strain for the sample deformed at 5 % is close to the true strain for the sample deformed at 10 % is because the ratio h/d (see Chapter 2) is not equal to 2 for the square-based bar samples while the ratio is equal to 2 for the cylinder samples. The mechanism of deformation for this material proposed by Tian and his colleagues is identified and confirmed with these tests. For the mechanism of damage inside the grains, because the temperature is above the transition temperature from brittle to plastic deformation, the dislocations acquires enough energy to move out of the basal slip direction. They will then move towards the grain boundaries where they will accumulate. The local stress field is strongly increased because of this and causes the apparition of fractures in the grains and breaks them. Moreover, delamination within grains is also frequently observed in deformed samples. But these intragranular deflects

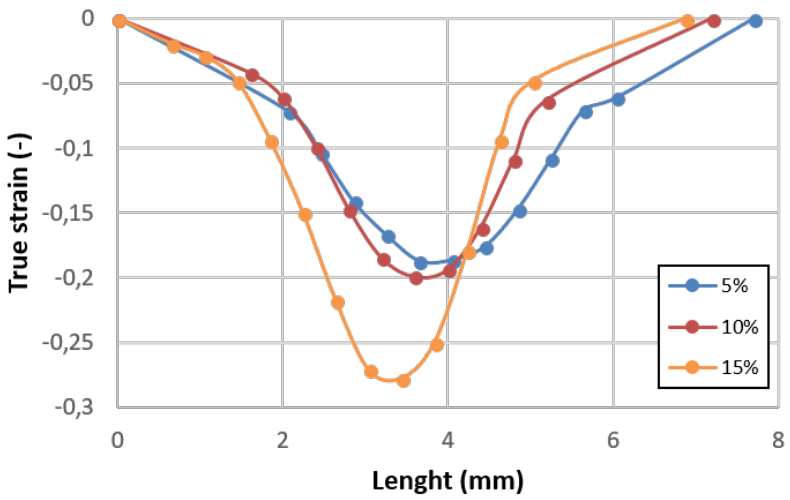

Figure 4.26: Graph of the local true strain as a function of the length of the sample for different global compressive strains

represent a small part of the global deformation. The intergranular damage is the main damage mechanism and is also very present in these samples. This mechanism is the decohesion of the grains between each others. The inter- and intra-granular mechanisms are shown in Figure 4.27.

All these mechanisms of deformation are mainly observed in the torus part of the spindle shape. Indeed, the grains in the central axis or closed to the edges of the sample in contact with the pistons are spared of whole damages.

Let's now compare the stress/strain curves for the sample as a function of their macroscopic shape. Figures 4.28 and 4.29 show these curves for the square-based bar and the cylinder samples, respectively. For the square-based samples, the behaviour at 5 % is the expected behaviour regarding the sample deformed until 20 %. On the contrary, the elastic deformation allowed for the cylinder samples is lower, the plastic regime occurs almost immediately after the beginning of the loading. And it is an interesting behaviour that will be further discussed in the following paragraphs. The blue curve in Figure 4.29 shows an elastic behaviour similar to the sample deformed at 5 % even if the macroscopic shapes are different. That point is well shown on Figure 3.14 where the beginning of the orange and the blue curves are identical. On the other hand, the sample deformed at 15 % does not show, even at the very first beginning of the increasing of the stress, the same slope for the elastic regime. What is interesting to note is that the sample deformed at 10 % may be considered as an intermediate behaviour between the samples deformed at 5 and 15 %. This assumption has to be confirmed by performing more tests to reproduce the results at 1000°C for 5, 10, 15 and 20 %. Through these tests, one will try to identify the parameters that can induce these differences. Regarding these three tests, two sets of parameters may be involved and are summarised below.

Between the samples deformed at 5 and 10 % the potential parameters during the life of the samples that can influence the mechanical test are the macroscopic shape (either the bar compared to the cylinder, or the ratio h/d), the texture (see Figure 2.11), the sintering process (closed relative density) and the microstructure (grain size). For the samples deformed at 10 and 15 %, one issue for this difference is maybe the location where the cylinder has been cut in the specimen coming from the SPS process. Nevertheless, other possibilities exist to explain this behaviour, the mechanical test itself contains differences in the procedure, like a wrong placement of the sample between the pistons which can induce a concentration of stress at one point, or a bad weld of the thermocouple that may cause an incorrect measure of the temperature. This is why the results have to be reproduced before testing all these parameters.

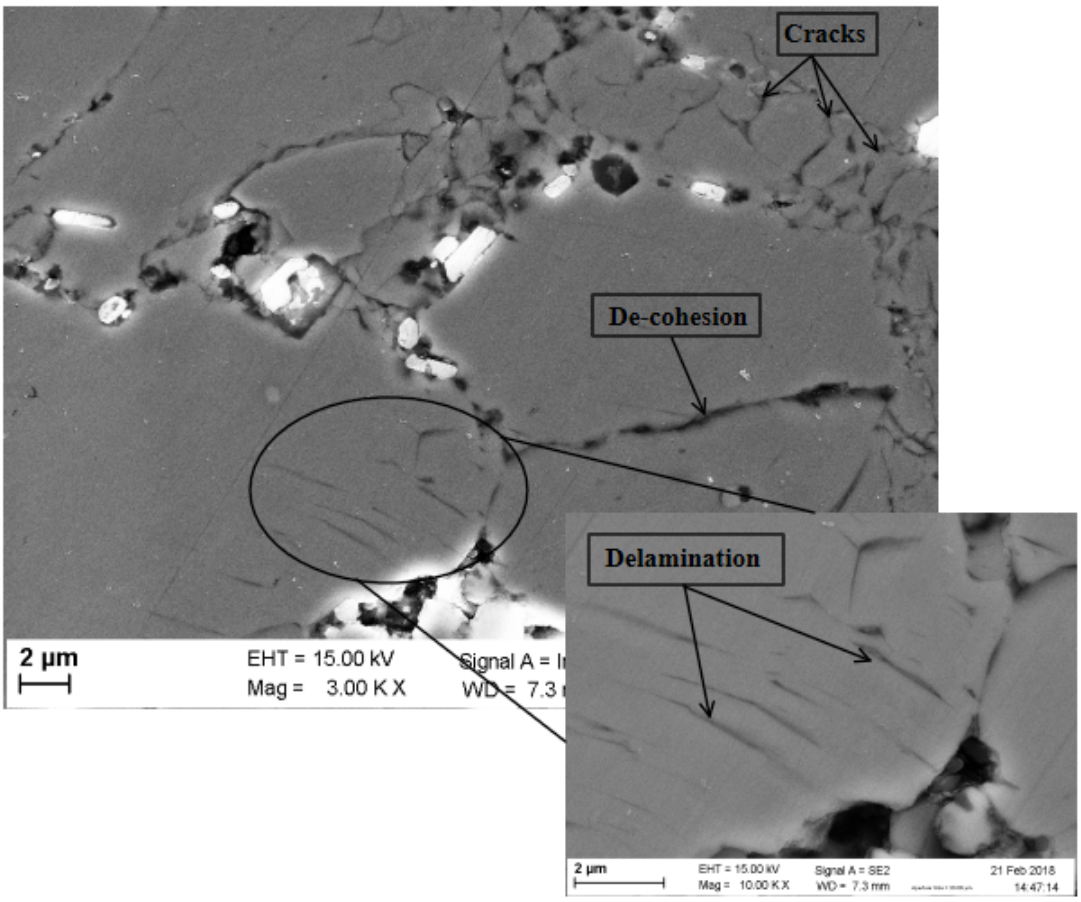

Figure 4.27: SEM images of the centre of a deformed sample, after a cutting and polishing process, the two mechanisms of damaging are observed, intergranular with the decohesion of the grains and within with the cracks propagation due to the movement of the dislocations and the delamination

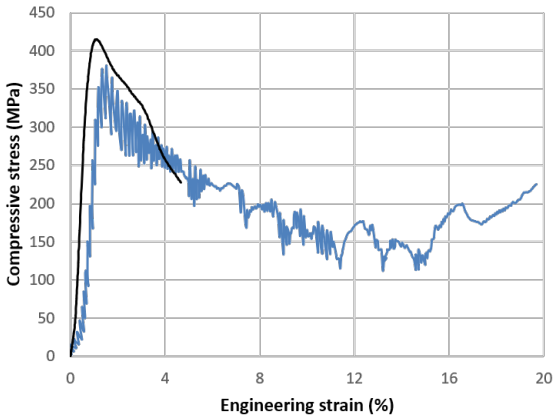

Figure 4.28: Stress/strain curves of square-based bar samples compressed at 1000°C until 5 and 20 % in strain

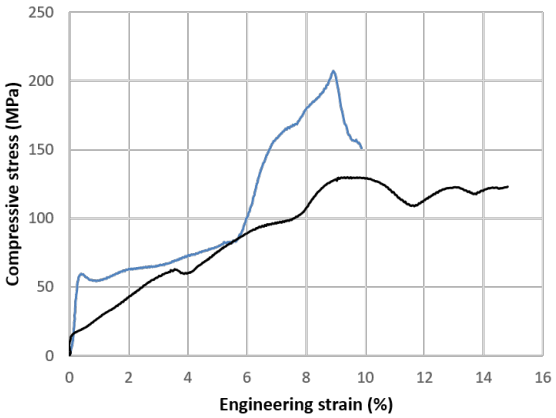

Figure 4.29: Stress/strain curves of cylinder samples compressed at 1000°C until 10 and 15% in strain

According to the analyses made previously in this chapter, the behaviour of the samples under creep will be covered. The main result obtained in this work regarding the creep tests is that the square-based samples effectively creep even under 100 MPa (Figures 3.18 and 3.19) while the

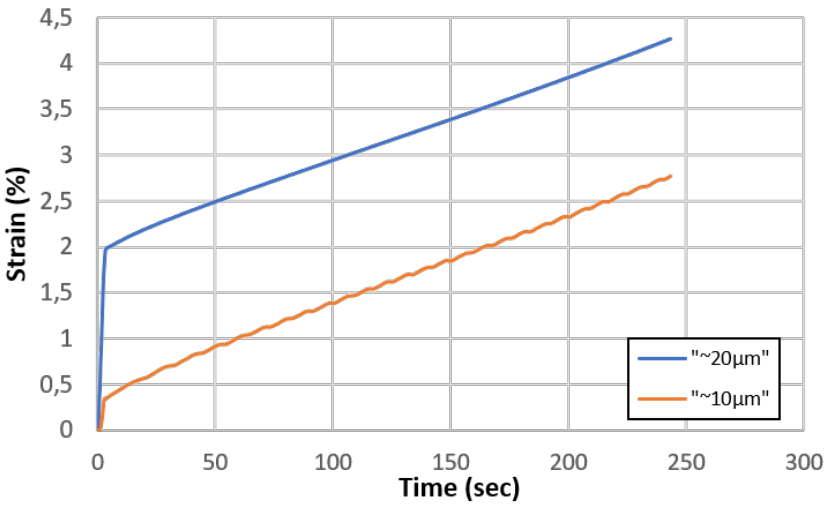

Figure 4.30: Comparison of the creep behaviour at 1000°C and 100 MPa for samples sintered at 1400 (blue curve) and at 1200°C (orange curve), with similar other sintering conditions

cylinder samples do not creep (Figures 3.20 and 3.21) at a smaller loading. On the square-based samples, a comparison can be achieved as a function of the microstructure of the samples, or in other words, their mean grain size (Figure 4.30).

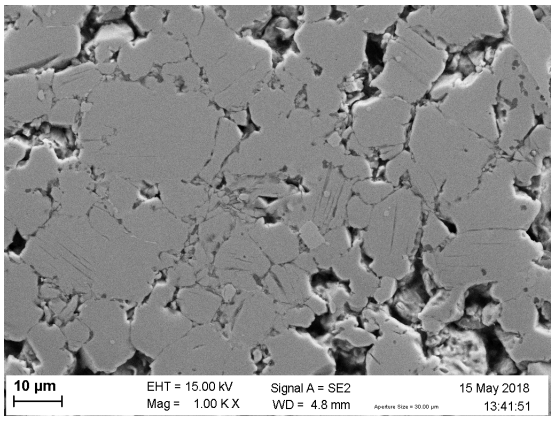

Figure 4.31: SEM image of the surface of the sample sintered under the reference condition and creep at 1000°C under 100 MPa located un the deformed part (torus of the spindle-like shape)

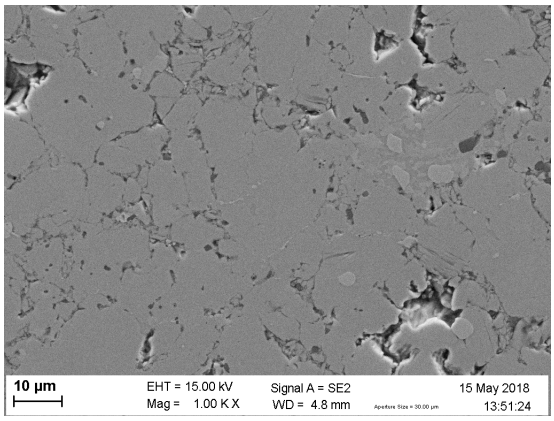

Figure 4.32: SEM image of the surface at the centre of the sample sintered and creep in the same conditions as the sample in Figure 4.31

During the primary creep, the sample with bigger grains shows a strain rate 3 times faster than the sample sintered at 1200°C. The strain rate are $6 \cdot 10^{-3}$ and $1.8 \cdot 10^{-3} s^{-1}$, respectively. On the other hand, when the two samples begin the secondary creep, their slope decrease as expected, and become $9.5 \cdot 10^{-4}$ and $1.1 \cdot 10^{-4} s^{-1}$, respectively (see Chapter 3). It is observed that the strain rate depends on the grains size, even with such a small difference. This result is aligned with the literature, Zhen *et al.* arrived at the same conclusion after performing compressive creep tests on fine- and coarse-grain samples of Ti_3SiC_2 above the transition temperature [ZBK+05]. In both observations, bigger grain size induced a larger strain rate during the creep, and the difference is small even when the difference of size is important (Figure 4.33).

A polishing surface showing the microstructure of the sample (cutting in two part to see the bulk microstructure) of Cr_2AlC sintered under the reference conditions and creep at 1000°C under

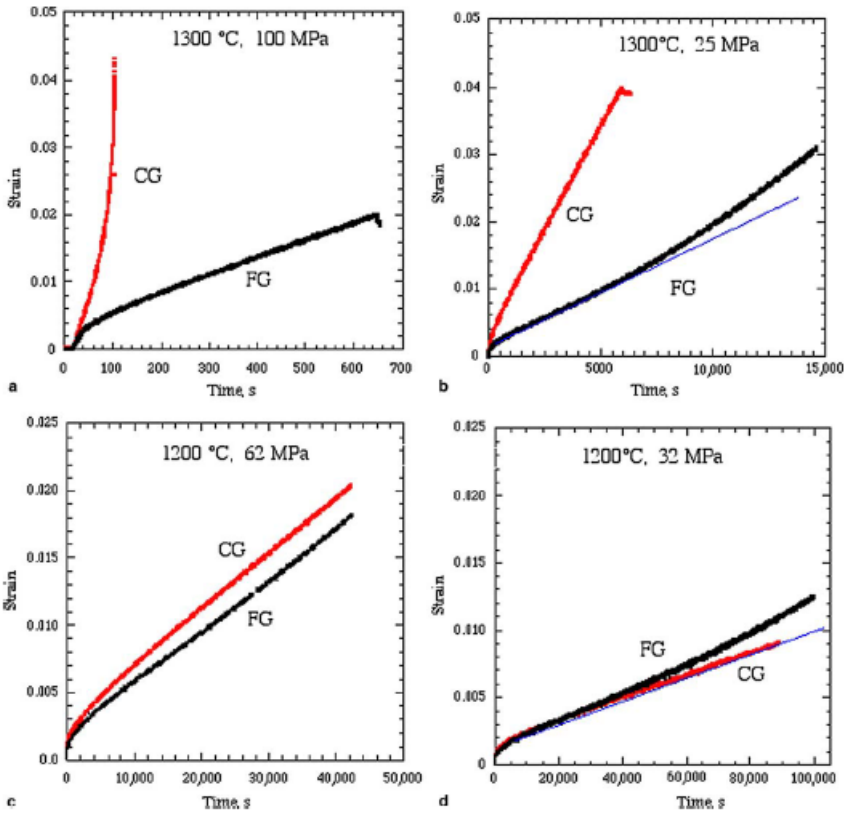

Figure 4.33: Creep curve for fine- and coarse grains of Ti_3SiC_2 in compression for different temperature, above the transition temperature, and loading

100 MPa is available in Figure 4.31. This surface belongs to the torus part of the spindle-like shape of the deformed sample. It is compared to the surface of the same sample deformed but located in the centre of the bar (Figure 4.32). Large pores are found in the torus region of a deformed sample due to the treatment that the sample received after deformation. As already said, these treatments are the cutting and the polishing processes. These manipulations in addition to the deformation mechanism (decohesion of the grains) lead to a pullout of some grains almost disconnected form the matrix and create this extra amount of porosity. Among the decohesion of the grains, delaminations inside the grains is also well observed and in greater amount on Figure 4.31 than in the centre of the sample. These two mechanisms are the main ones that occur during the deformation at high temperature.

The results obtained for the cylinder samples in creep are quite obvious. Because of their small compressive strength and the high stress rate of the creep tests, cracks propagate quickly between the grains (Figure 4.34) and give this particular shape in inverse spindle (remember Figures 3.20 and 3.21 in Chapter 3). This result can imply that the transition temperature, or the regime of plastic deformation depends on the stress rate at which the sample is deformed. This means that the transition temperature is not a property of the material but depends on external parameters. As observed for the creep and the compressive tests, the center of the bars, or the cylinders, seems not affected by the loading and remains almost undeformed. This behaviour is not already fully understood and does not seems influenced by the macroscopic shape.

The main mechanism for the creep deformation according to Zhen and its colleagues is the diffusion creep for the MAX-phase Ti_3SiC_2 at low stress [ZBK+05]. It is not possible to draw such a conclusion with the tests performed to date on Cr_2AlC but there is no apparent reasons

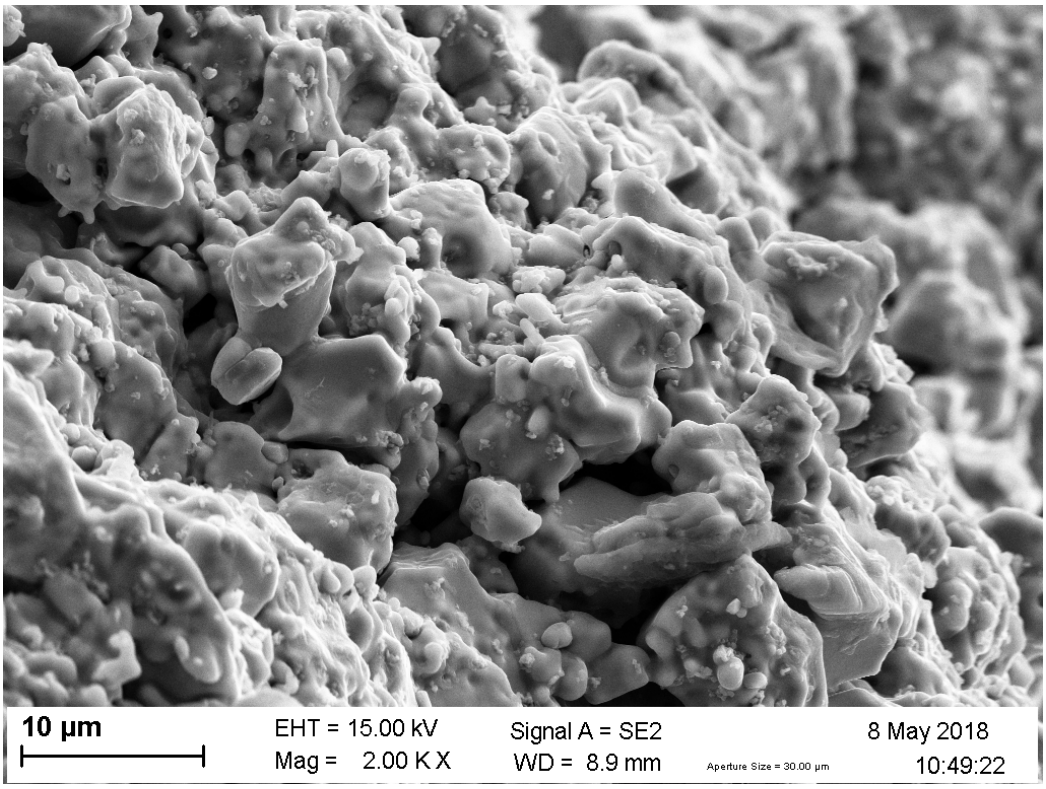

Figure 4.34: SEM image of the fracture surface of the cylinder sample creep at 1000°C under 50 MPa, higher magnification of the fracture in Figure 3.20

to believe that it isn't true. Indeed, only one temperature and one loading have been tested for creep tests. To be able to identify the main creep mechanism, the parameters that have to be studied are the sintering temperature, or the grain size of the sample creep with supplementary tests at other temperature and loading.

Chapter 5

Conclusion and perspectives

To conclude this report, a summary of the main results presented in this work is given. A future experimental procedure then proposed to further continue the research and answer questions that are still open. Eventually, some perspectives are proposed for the years to come in the study of the MAX-phase.

First, optimal sintering conditions have been determined for the synthesis of a specimen height of 3 mm and with a diameter of 20 mm. The conditions are a sintering temperature of 1200°C for 5 minutes, under 30 MPa and with a heating rate of 100°C/min. They lead to a microstructure with the finest grains, 5.62 (± 0.89) μm and the highest density, 99.72 (± 0.08) %. It is also under these sintering conditions that the purest MAX-phase is synthesize, 97.33 (± 0.68) % of Cr_2AlC. Presence of iron has been found in the powder used for the sintering process and this iron is found in sample sintered under 1300°C under the form of dendrites of intermetallic Fe-Al. The effect of the sintering temperature has been identify and as expected, induces a faster growth of the grains during the process. The presence of a texture has also be noted for the sample sintered with 6g of powder. An interesting feature would be to synthesize a sample with 18g of powder to obtain of cylinder height of 8 mm and with a diameter of 4 mm, but under the optimal condition. This would allow to perform mechanical tests at room and high temperature and compare the results with those of this work.

At room temperature and under micro- and nano-indentation, delamination and intergranular cracks have been observed as damage mechanism around the indents. The difference between the hardness obtained with the two methods have been highlighted. A model to explain the dependence of the Berkovich hardness as a function of the depth of the indent is described. Additional indents with different loading have to be realized to draw a complete model of the variation of the hardness with the indentation depth. Some discontinuities in the load/displacement curves obtained with the Berkovich indenter are explained with the experimental procedure using by the nano-indenter during the tests and the mechanical damages induced by the indentation. Indentations under a higher temperature than the transition temperature could be an interesting topic to further study. That kind of tests would allow to obtained results such as the hardness at high temperature and observe its evolution. The plastic behaviour of the material around the mark of the indent would also be observed.

In a second part, the behaviour at high temperature has been studied. Compressive tests on square-based bar and cylinder samples have been achieved and different behaviours were observed. Damage mechanisms of intergranular, such as de-cohesion of grains, and intragranular have been identify. Compared with the mechanisms at room temperature, only cracks inside grains, due to the accumulation of the dislocation at the grain boundaries, are new in the damage mechanism. This phenomenon has been explained because the dislocations at a temperature higher than the transition between brittle and plastic regime are allowed to move out of their basal slip plan and

propagate through the grains. At 800°C, the sample failed in a brittle manner while at 1000°C the sample does not failed but deforms in a lightning bolt-like shape. The microstructure and the macroscopic shape have an important influence on the compressive strength of the samples. These parameters have also an influence on the creep behaviour. The strain rate decreases with the grain size. Furthermore, a creep test under a loading close to the compressive strength of the sample will lead to a inverse spindle as observed in this work. The sintering conditions have to be adjusted as explained above to obtain another microstructure and increase the compressive strength of cylinder samples. Creep tests with higher and lower loading, for the same grain size, have also to be performed to identify the main creep mechanism. Eventually, creep tests under a temperature higher than 1000°C may be performed to identify the resistance under creep as a function of the temperature.

Appendix A

Sintering curves

The analysis of the sintering curve from the SPS process is reported in the following paragraphs, this analyse comes from the report that presents the results obtained during the traineeship realised during the summer holidays of 2017 at BCRC. Figure A.1 represents the relative displacement of the pistons during the SPS process heating at 1200°C for 5 minutes with an applied pressure of 10 MPa and a heating rate of 100°C/min.

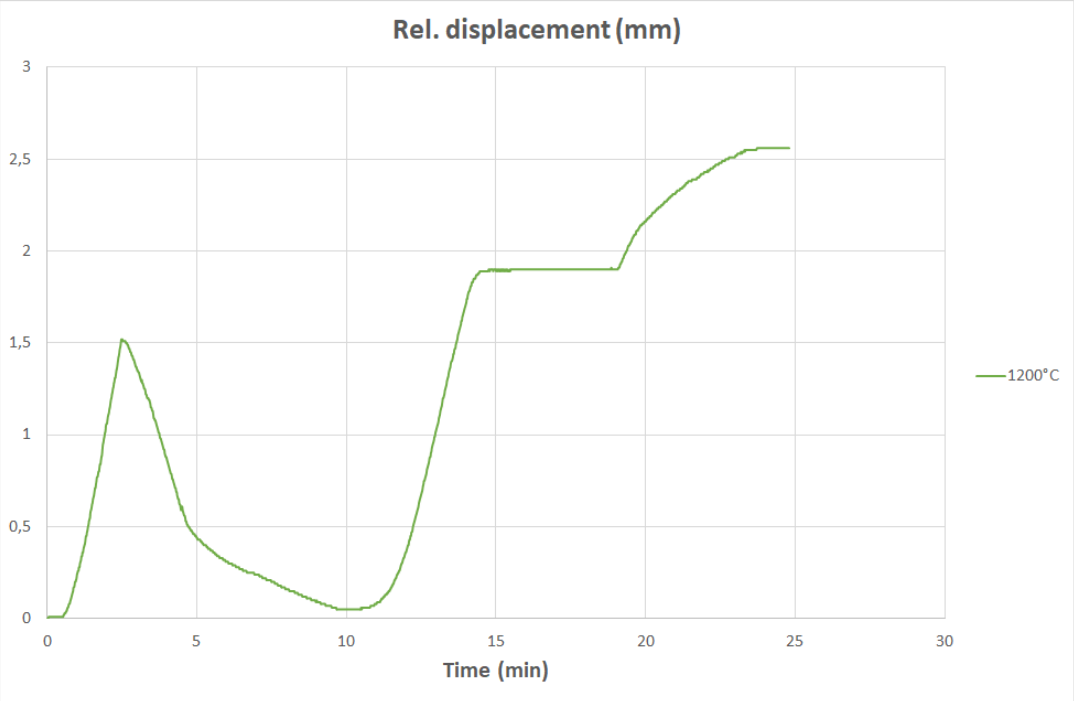

Figure A.1: Relative displacement of the pistons as a function of the time of the SPS process for a sample of Cr_2AlC heating at 1200°C for 5 minutes with a heating rate of 100°C/min and under a pressure of 10 MPa

The first increase of the curve is a compression of the sample before heating it under a pressure of 60 MPa, then the pressure is released and the sample expands. The change in the slope, after 5 minutes, shows the starting of the alternative current through the pistons and so the beginning of the heating process. The second increase, after 10 minutes, is due to the beginning of the sintering reaction because of the rise of the temperature. The plateau implies that the temperature reached 1200°C and stopped increasing. The last increase of the relative displacement is due the shrinking of the sample due to the cooling.

As already explained, relative displacement of the samples heating at 1400°C and 1300°C with a melting part, and 1200°C without melting part are represented on the Figure A.2 (a).

On the blue and orange curves, the first plateau is observed but its origin is not yet explained. To try to understand when it appears, Figure A.2 (b) shows that the two plateaus start at approximately the same temperature of 1220-1240°C. The sample at 1200°C does not reach 1215°C so there is only one plateau, on the Figure A.2 (a), when one stops the heating process.

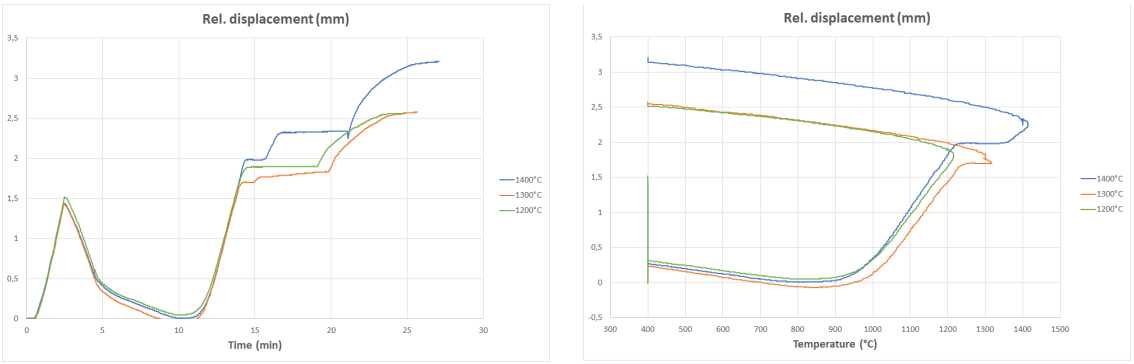

Figure A.2: (a) Relative displacement of the pistons as a function of the time of the SPS process (b) relative displacement of the pistons as a function of the evolution of the temperature of the sample during the process for the samples of Cr_2AlC heating at 1400, 1300 and 1200°C for 5 minutes with a heating rate of 100°C/min and under a pressure of 10 MPa

With respect to the different results obtained with the cycles at 1200°C, three parameters could be compared: the pressure, the heating rate under a certain pressure and the moment at which the compression starts.

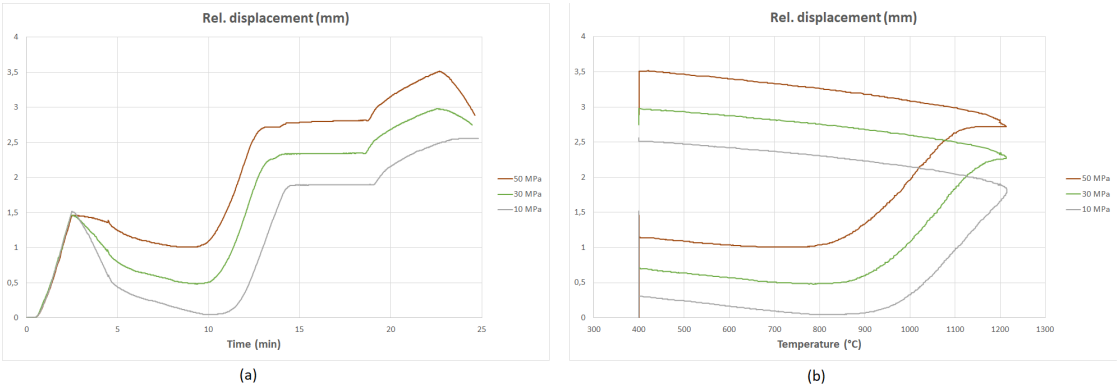

Figure A.3: (a) Relative displacement of the pistons as a function of the time of the SPS process (b) relative displacement of the pistons as a function of the evolution of the temperature of the sample during the process for the samples of Cr_2AlC heating at of 1200°C for 5 minutes with a heating rate of 100°C/min and under pressure of 10, 30 and 50 MPa

On Figure A.3, the expected behaviour of the sintering curve is observed for the sample compressed at 50 MPa, a larger displacement. One can also observe on the Figure A.3 (a), two plateaus on the curve at 30 and 50 MPa. These plateaus can be compared with samples sintered at a temperature above 1300°C but without melting part during the process. On the figure (b) the plateaus are also observed and they start at a different temperature. Eventually, under 400°C, an elastic return is observed and it is larger for higher pressures applied during the

process. This phenomenon is explained because the load is maintained during the cooling and it is realised after the temperature of the sample goes down 400°C. So, the three samples have approximately the same final relative displacement at the end of the sintering process.

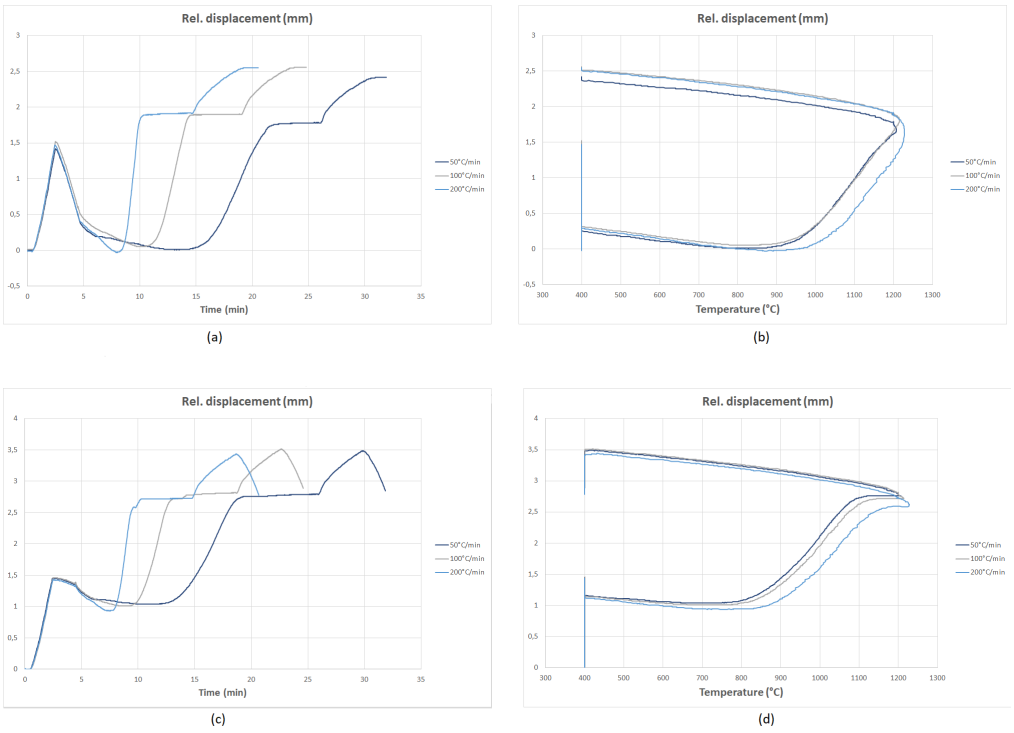

Figure A.4: Relative displacement of the pistons of the SPS, for the samples of Cr_2AlC compressed at 10 MPa and heating at 1200°C, as a function of (a) the time of the process and (b) the temperature of the sample during the process with a heating rate of 50, 100 and 200°C/min. The figures (c) and (d) show the relative displacement of samples sintered in the same conditions of temperature and heating rate but under a pressure of 50 MPa

Figure A.4 shows fours graphs related to the change of the heating rate during the process, under a pressure of 10 MPa (Figures A.4 (a) and (b)) and 50 MPa (Figures A.4 (c) and (d)). One observation is that the heating rate has no influence on the relative displacement of the pistons, as seen on Figures A.4 (b) and (d) but only the total time of the process. It will be longer for shorter heating rate. On Figure A.4 (d), the stabilization observed around 1100°C seems to indicate that the first densification is reached but on the graph (c), around 1200°C, the displacement increases again a bit.

The last parameter studied in this section is the moment when the compression begins. The difference in the operating conditions can be observed on Figure A.5. On the left figure, the pressure is realized until 10 MPa and anew applied once the relative displacement has reached the minimum (which correspond to a sample of 800°C) and starts to increase until the beginning of the cooling part of the process (Figure A.5 (a)). While on the right figure the pistons realise the pressure after the application of the 60 MPa and stop at 30 MPa (before the beginning of the heating part of the process). They maintain the loading until the end of the cooling (Figure A.5 (b)).

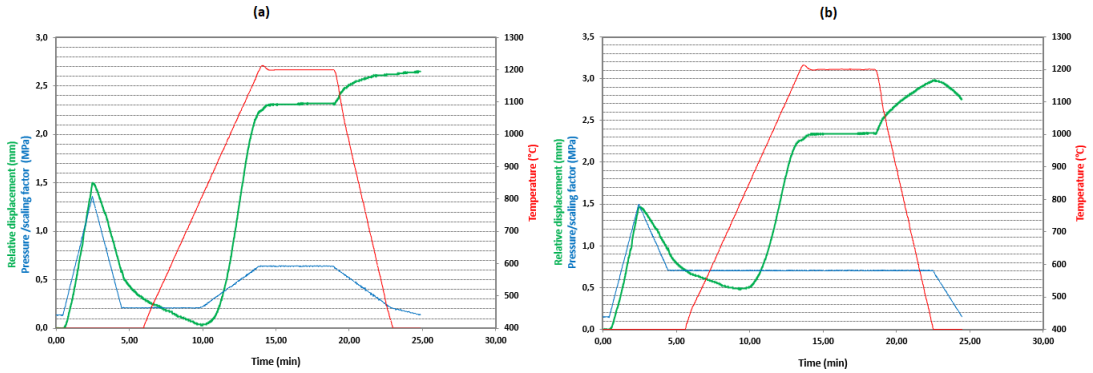

Figure A.5: Operating conditions of samples sintered at 1200°C for 5 minutes with and heating rate of 100°C/min with (a) the application of the pressure of 30 MPa start when the temperature of the sample reach 800°C, which correspond to the minimum of the relative displacement and (b) the pressure of 30 MPa is applied directly after the first loading of 60 MPa

For the conditions shown on Figure A.5 (a), the relative displacement of the pistons as a function of the time of the process and the temperature of the system for a pressure of 30 and 50 MPa are shown in Figure A.6 and compare with their correspondent of operating conditions shown on Figure A.5 (b).

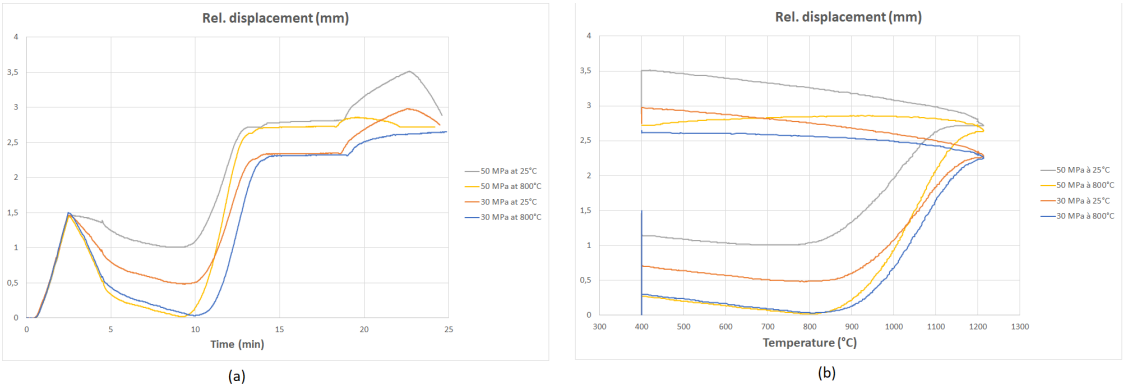

Figure A.6: Relative displacement of the pistons of the SPS as a function of (a) the time of the process and (b) the temperature of the sample during the process of samples of Cr_2AlC, the red and grey curve represents the displacement of a cycle when the loading, of 30 and 50 MPa respectively, is applied to the room temperature and on the blue and yellow curve, the loading starts at 800°C who corresponds to the minimum of the relative displacement on the graph in (a)

Eventually, it is also observed that the moment when the compression starts will not influence the final relative displacement. But it can also be observed that a little plateau is present before 1200°C. This phenomenon is then recurrent and it could be interesting to carry on interrupted tests on SPS before and just after the plateau and do XRD and MEB-EDS analysis on these samples to try to understand it. As last remark, the difference during the cooling phase is explained by the relaxation of the pressure at the beginning of the cooling, so at 1200°C for the samples charged at 800°C while the pressure is maintained during the cooling until 400°C for all other processes.

Appendix B

Pole figure

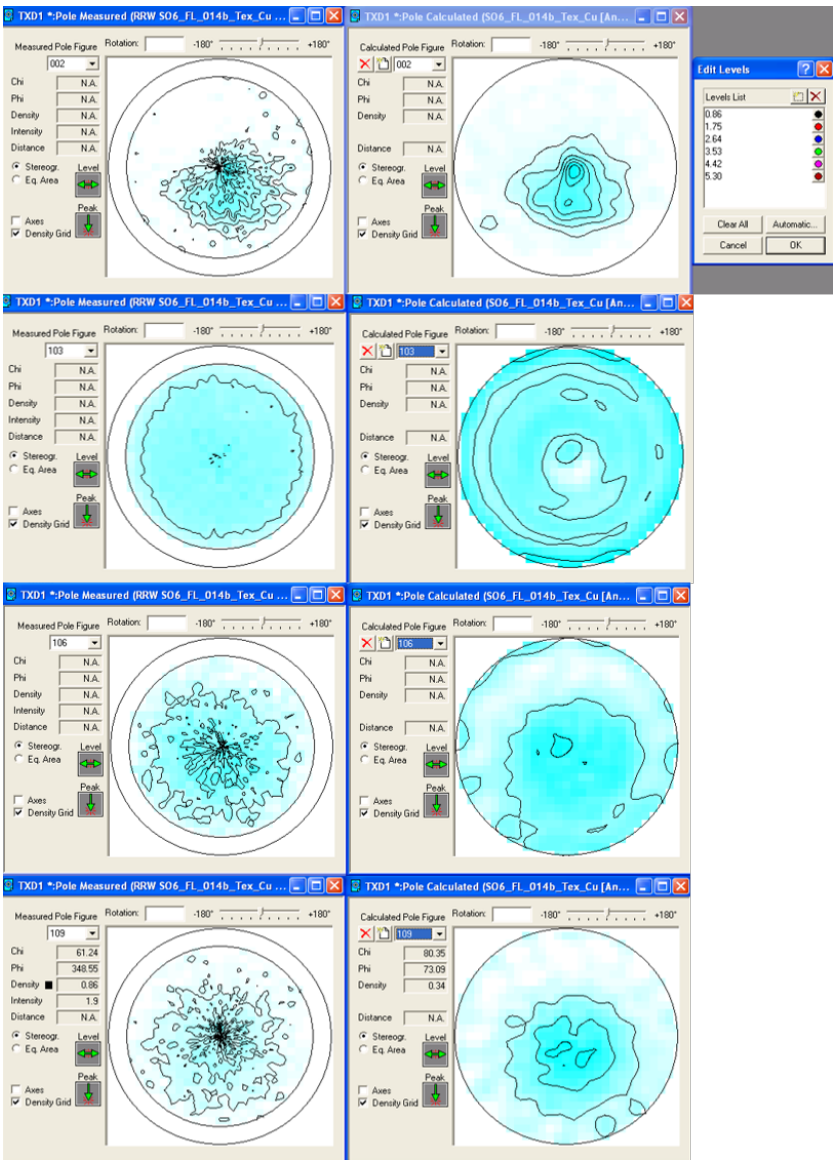

Figure B.1: Pole figures measured, on sample sintered at 1400°C and other conditions as the reference, and calculated for the triclinic symmetry

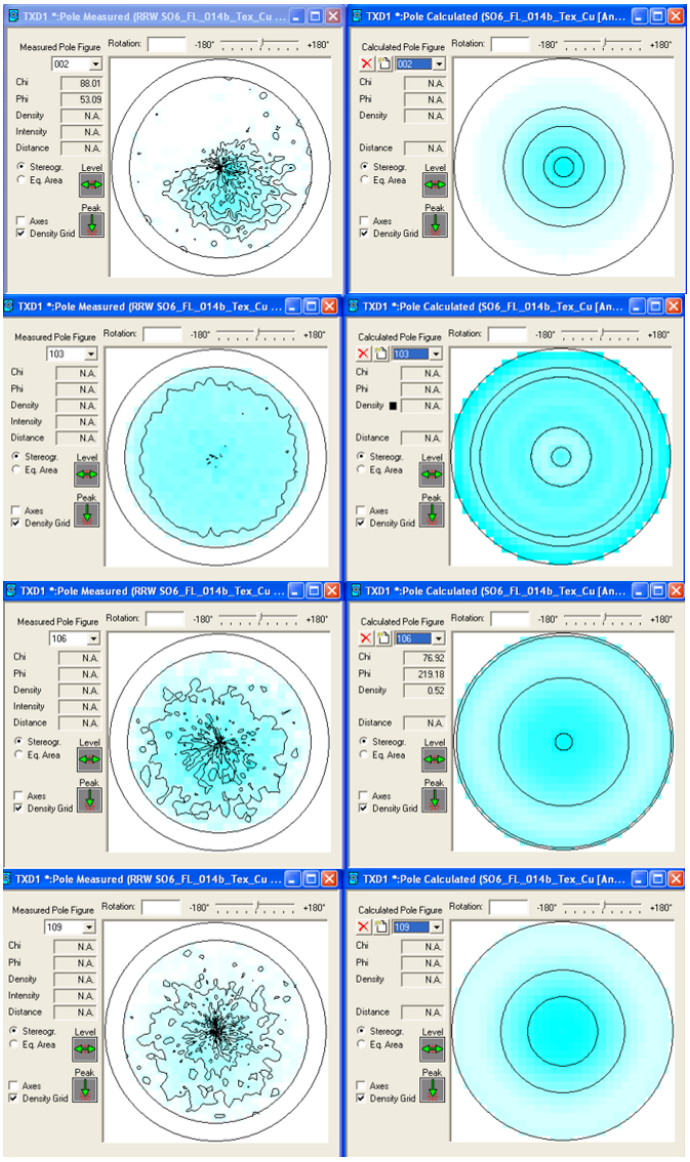

Figure B.2: Pole figures measured, on sample sintered at 1400°C and other conditions as the reference, and calculated for the fiber symmetry

Appendix C

Density calculation

	S06-FL-014	S06-FL-018	S06-FL-020	S06-FL-029	S06-FL-030	S06-FL-032	S06-FL-033	B2533
Dry mass (g)	5,18026667	5,26083333	5,28333333	5,2855	5,0238	5,0317	5,10525	13,4824
Mass under water (g)	4,19526667	4,2525	4,26886667	4,27006667	4,0599	4,0675	4,12565	10,84973333
Wet mass (g)	5,18253333	5,26293333	5,28413333	5,2868	5,02495	5,0337	5,10675	13,5288
Liquid density (g/cm³)	0,99862	0,99862	0,99862	0,99843	0,99843	0,99843	0,99843	0,9982
Theoric density of Al2O3 (g/cm³)	3,987	3,987	3,987	3,987	3,987	3,987	3,987	3,987
Theoric density of Cr7C3 (g/cm³)	6,877	6,877	6,877	6,877	6,877	6,877	6,877	6,877
Theoric density of Cr2AlC (g/cm³)	5,229	5,229	5,229	5,229	5,229	5,229	5,229	5,229
Amount of Al2O3 (%)	2,96	0,59	3,03	1,05	1,73	2,83	3,91	5,03
Min value	1,87	0,16	2,43	0,00	1,13	0,02	1,16	0,00
Max value	4,05	1,02	3,63	2,22	2,33	5,64	6,66	11,22
Amount of Cr7C3 (%)	8,97	6,45	2,28	3,99	0,66	3,86	4,99	3,69
Min value	4,25	1,32	0,81	3,78	0,45	1,10	0,00	0,00
Max value	13,69	11,58	3,75	4,20	0,87	6,62	11,88	7,81
Open porosity	0,23	0,21	0,08	0,13	0,12	0,21	0,15	1,73
Apparent density (g/cm³)	5,24	5,20	5,20	5,19	5,20	5,20	5,20	5,02
Closed apparent density (g/cm³)	5,25	5,21	5,20	5,20	5,20	5,21	5,20	5,11
Relative density (%)	98,12	97,59	99,38	98,27	99,60	98,90	98,72	96,10
Standard deviation	1,18	1,45	0,32	0,19	0,08	0,20	1,19	0,10
Max density	99,32	99,06	99,70	98,09	99,52	99,10	99,63	96,07
Min density	96,95	96,16	99,07	98,48	99,68	98,70	97,26	96,26
Closed relative density (%)	98,35	97,79	99,46	98,40	99,72	99,10	98,87	97,79
Standard deviation	1,19	1,45	0,32	0,19	0,08	0,20	1,19	0,10
Max density	99,55	99,26	99,78	98,22	99,64	99,30	99,78	97,76
Min density	97,18	96,36	99,15	98,60	99,80	98,90	97,41	97,96

Figure C.1: Summary of the calculation of the relative density of all the samples studied, the Max and Min value are determined with the standard deviation obtained of the amount of alumina and carbides in each sample, found in Appendix D

Appendix D

Mean linear intercept calculation

The results and details of the calculation of the mean grain size and the proportion of phases are summaries in the following tables. To have enough data for the statistics, many pictures are taken and many curves, as shown in Figure 2.6, have been drawn.

D.1 Grain size

	Label of pictures	Total length (µm)	Intercept/count	Mean grain size (µm)
1	S06-FL-014b_5x.jpg	776,386	35	22,18
2	S06-FL-014b_5x.jpg	548,301	24	22,85
4	S06-FL-014b_5x.jpg	608,229	32	19,01
5	S06-FL-014b_5x.jpg	694,097	34	20,41
1	S06-FL-014b_20x.jpg	279,195	20	13,96
2	S06-FL-014b_20x.jpg	284,564	15	18,97
3	S06-FL-014b_20x.jpg	316,779	13	24,37
4	S06-FL-014b_20x.jpg	250,559	15	16,70
1	S06-FL-014b_50x.jpg	148,387	5	29,68
2	S06-FL-014b_50x.jpg	126,882	10	12,69
3	S06-FL-014b_50x.jpg	138,172	8	17,27
4	S06-FL-014b_50x.jpg	108,602	7	15,51
Mean (µm)				**19,47**
SD (µm)				**4,79**

Figure D.1: Summary of the calculation of the mean grain size for the sample of Cr_2AlC sintered at 1400°C for 5 minutes, with a loading of 10 MPa and a heating time of 100°C/min, SD is the standard deviation

	Label of pictures	Perim of circle (µm)	Total length of lines (µm)	Intercept/count	Mean grain Size (µm)
1	018-grainSize-20x-BF-1.jpg	0,00	367,11	28	13,11
2	018-grainSize-20x-BF-1.jpg	0,00	346,31	29	11,94
3	018-grainSize-20x-BF-1.jpg	0,00	322,82	30	10,76
4	018-grainSize-20x-BF-1.jpg	396,39	0,00	37	10,71
1	018-grainSize-50x-BF-1.jpg	0,00	145,16	13	11,17
2	018-grainSize-50x-BF-1.jpg	0,00	172,04	12	14,34
3	018-grainSize-50x-BF-1.jpg	0,00	158,06	11	14,37
4	018-grainSize-50x-BF-1.jpg	238,15	0,00	24	9,92
Mean (µm)					**12,04**
SD (µm)					**1,71**

Figure D.2: Summary of the calculation of the mean grain size for the sample of Cr_2AlC sintered at 1300°C for 5 minutes, with a loading of 10 MPa and a heating time of 100°C/min, SD is the standard deviation

	Label of pictures	Total length (µm)	Intercept/count	Mean grain size (µm)
1	S06-FL-020_5x.jpg	624,329	40	15,61
2	S06-FL-020_5x.jpg	481,216	39	12,34
3	S06-FL-020_5x.jpg	685,152	74	9,26
4	S06-FL-020_5x.jpg	898,032	80	11,23
1	S06-FL-020_10x.jpg	550,336	60	9,17
2	S06-FL-020_10x.jpg	603,132	72	8,38
3	S06-FL-020_10x.jpg	461,745	54	8,55
4	S06-FL-020_10x.jpg	463,535	49	9,46
1	S06-FL-020_50x.jpg	118,996	17	7,00
2	S06-FL-020_50x.jpg	117,563	18	6,53
3	S06-FL-020_50x.jpg	93,907	8	11,74
4	S06-FL-020_50x.jpg	90,323	15	6,02
Mean (µm)				**9,61**
SD (µm)				**2,74**

Figure D.3: Summary of the calculation of the mean grain size for the sample of Cr_2AlC sintered at 1200°C for 5 minutes, with a loading of 10 MPa and a heating time of 100°C/min, SD is the standard deviation

	Label of pictures	Perim of circle (µm)	Total length of lines (µm)	Intercept/count	Mean grain Size (µm)
1	030-grainSize-50x-BF-att-1.jpg	121,77	121,77	26	4,68
2	030-grainSize-50x-BF-att-1.jpg	134,14	134,14	21	6,39
3	030-grainSize-50x-BF-att-1.jpg	135,75	135,75	22	6,17
4	030-grainSize-50x-BF-att-1.jpg	263,49	0,00	38	6,93
1	030-grainSize-100x-BF-att-1.jpg	67,97	67,97	12	5,66
2	030-grainSize-100x-BF-att-1.jpg	75,00	75,00	13	5,77
3	030-grainSize-100x-BF-att-1.jpg	65,95	65,95	15	4,40
4	030-grainSize-100x-BF-att-1.jpg	133,31	0,00	27	4,94
Mean (µm)					**5,62**
SD (µm)					**0,89**

Figure D.4: Summary of the calculation of the mean grain size for the sample of Cr_2AlC sintered at 1200°C for 5 minutes, with a loading of 30 MPa and a heating time of 100°C/min, SD is the standard deviation

	Label of pictures	Circle area (µm²)	Radius (µm)	Perimeter (µm)	Total length of lines (µm)	Intercept/count	Mean grain size (µm)
1	S06-FL-033-surf-GrainSize-x20-HF	5557,51	42,06	264,27	0,00	33	8,01
2	S06-FL-033-surf-GrainSize-x20-HF	12862,68	63,99	402,04	0,00	43	9,35
3	S06-FL-033-surf-GrainSize-x20-HF	13407,20	65,33	410,46	0,00	36	11,40
4	S06-FL-033-surf-GrainSize-x20-HF	6803,90	46,54	292,40	0,00	32	9,14
1	S06-FL-033-x20-att.jpg	0,00	0,00	0,00	382,657	35	10,93
2	S06-FL-033-x20-att.jpg	0,00	0,00	0,00	394,31	40	9,86
3	S06-FL-033-x20-att.jpg	0,00	0,00	0,00	441,57	47	9,40
4	S06-FL-033-x20-att.jpg	0,00	0,00	0,00	346,313	30	11,54
1	S06-FL-033-surf-GrainSize-x50-HF	3941,60	35,42	222,56	0,00	35	6,36
2	S06-FL-033-surf-GrainSize-x50-HF	2384,40	27,55	173,10	0,00	29	5,97
3	S06-FL-033-surf-GrainSize-x50-HF	3366,89	32,74	205,69	0,00	29	7,09
4	S06-FL-033-surf-GrainSize-x50-HF	6284,03	44,72	281,01	0,00	37	7,59
1	S06-FL-033-x50-att.jpg	0,00	0,00	0,00	127,405	20	6,37
2	S06-FL-033-x50-att.jpg	0,00	0,00	0,00	156,566	23	6,81
3	S06-FL-033-x50-att.jpg	0,00	0,00	0,00	168,604	20	8,43
4	S06-FL-033-x50-att.jpg	0,00	0,00	0,00	181,341	27	6,72
1	S06-FL-033-surf-GrainSize-x100-HF	931,66	17,22	108,20	0,00	21	5,15
2	S06-FL-033-surf-GrainSize-x100-HF	1031,16	18,12	113,83	0,00	19	5,99
3	S06-FL-033-surf-GrainSize-x100-HF	1031,16	18,12	113,83	0,00	19	5,99
4	S06-FL-033-surf-GrainSize-x100-HF	1668,99	23,05	144,82	0,00	24	6,03
1	S06-FL-033-x100-att.jpg	0,00	0,00	0,00	99,163	14	7,08
2	S06-FL-033-x100-att.jpg	0,00	0,00	0,00	86,203	10	8,62
3	S06-FL-033-x100-att.jpg	0,00	0,00	0,00	81,069	15	5,40
4	S06-FL-033-x100-att.jpg	0,00	0,00	0,00	81,007	14	5,79
Mean (µm)							7,71
SD (µm)							1,93

Figure D.5: Summary of the calculation of the mean grain size for the sample of Cr_2AlC sintered at 1200°C for 5 minutes, with a loading of 50 MPa and a heating time of 100°C/min, SD is the standard deviation

	Label of pictures	Total length (µm)	Intercept/count	Mean grain size (µm)
1	S06-FL-032-x20-att.jpg	305,118	31	9,84
2	S06-FL-032-x20-att.jpg	361,993	39	9,28
3	S06-FL-032-x20-att.jpg	390,567	36	10,85
4	S06-FL-032-x20-att.jpg	372,441	33	11,29
5	S06-FL-032-x50-att.jpg	155,207	17	9,13
6	S06-FL-032-x50-att.jpg	159,445	22	7,25
7	S06-FL-032-x50-att.jpg	170,487	24	7,10
8	S06-FL-032-x50-att.jpg	160,502	17	9,44
9	S06-FL-032-x100-att.jpg	86,184	12	7,18
10	S06-FL-032-x100-att.jpg	83,109	12	6,93
11	S06-FL-032-x100-att.jpg	102,125	14	7,29
12	S06-FL-032-x100-att.jpg	70,67	9	7,85
Mean (µm)				**8,62**
SD (µm)				**1,55**

Figure D.6: Summary of the calculation of the mean grain size for the sample of Cr_2AlC sintered at 1200°C for 5 minutes, with a loading of 10 MPa and a heating time of 50°C/min, SD is the standard deviation

	Label of pictures	Total length (µm)	Intercept/count	Mean grain size (µm)
1	S06-FL-029-x20-att.jpg	343,635	40	8,59
2	S06-FL-029-x20-att.jpg	380,323	51	7,46
3	S06-FL-029-x20-att.jpg	258,935	34	7,62
4	S06-FL-029-x20-att.jpg	335,97	32	10,50
1	S06-FL-029-x50-att.jpg	136,031	29	4,69
2	S06-FL-029-x50-att.jpg	147,477	27	5,46
3	S06-FL-029-x50-att.jpg	161,844	29	5,58
4	S06-FL-029-x50-att.jpg	152,134	25	6,09
1	S06-FL-029-x100-att.jpg	96,753	11	8,80
2	S06-FL-029-x100-att.jpg	87,893	17	5,17
3	S06-FL-029-x100-att.jpg	97,454	12	8,12
4	S06-FL-029-x100-att.jpg	82,741	11	7,52
Mean (µm)				**7,13**
SD (µm)				**1,75**

Figure D.7: Summary of the calculation of the mean grain size for the sample of Cr_2AlC sintered at 1200°C for 5 minutes, with a loading of 10 MPa and a heating time of 200°C/min, SD is the standard deviation

	Label of pictures	Total length (µm)	Intercept/count	Mean grain size (µm)
1	B2533-coeur-att-x50(6)-1.jpg	135,128	32	4,22
2	B2533-coeur-att-x50(6)-1.jpg	112,165	23	4,88
3	B2533-coeur-att-x50(6)-1.jpg	86,305	18	4,79
4	B2533-coeur-att-x50(6)-1.jpg	102,267	22	4,65
1	B2533-surf-att-x50(2).jpg	115,398	22	5,25
2	B2533-surf-att-x50(2).jpg	138,126	29	4,76
3	B2533-surf-att-x50(2).jpg	104,469	20	5,22
4	B2533-surf-att-x50(2).jpg	158,831	31	5,12
1	B2533-coeur-att-x50(5).jpg	123,148	25	4,93
2	B2533-coeur-att-x50(5).jpg	157,065	26	6,04
3	B2533-coeur-att-x50(5).jpg	130,808	26	5,03
4	B2533-coeur-att-x50(5).jpg	131,963	24	5,50
1	B2533-surf-att-x50.jpg	171,046	34	5,03
2	B2533-surf-att-x50.jpg	129,043	24	5,38
3	B2533-surf-att-x50.jpg	118,137	22	5,37
4	B2533-surf-att-x50.jpg	126,809	22	5,76
1	B2533-coeur-att-x50(3).jpg	146,535	17	8,62
2	B2533-coeur-att-x50(3).jpg	131,628	16	8,23
3	B2533-coeur-att-x50(3).jpg	142,997	17	8,41
4	B2533-coeur-att-x50(3).jpg	129,542	18	7,20
MEAN (µm)				**5,72**
SD (µm)				**1,31**

Figure D.8: Summary of the calculation of the mean grain size for a sample sintered at 1200°C for 5 minutes, with a loading of 10 MPa and a heating rate of 100°C/min, the amount of the powder used for the sintering process is 18g, so the sample is a final height of about 8 mm

D.2 Phase proportions

	label of pictures	Length of the segments (µm)	Identification phases	Proportion (%)	Somme of prop for each phases		Mean (%)	SD (%)
1	S06-FL-014b-NoAttack_01-1.tif	148,98	Total lenght	1	carbide	13,95	8,97	4,72
2	S06-FL-014b-NoAttack_01-1.tif	2,38	alumina	1,60	alumina	2,60	2,96	1,09
3	S06-FL-014b-NoAttack_01-1.tif	13,41	carbide	9,00	porosity	0,00	0,34	0,27
4	S06-FL-014b-NoAttack_01-1.tif	0,75	alumina	0,50	matrix	83,45	87,73	5,28
5	S06-FL-014b-NoAttack_01-1.tif	7,38	carbide	4,95				
6	S06-FL-014b-NoAttack_01-1.tif	0,75	alumina	0,50				
7	S06-FL-014b-NoAttack_01-1.tif	153,52	Total lenght	1	carbide	2,62		
8	S06-FL-014b-NoAttack_01-1.tif	0,83	alumina	0,54	alumina	1,85		
9	S06-FL-014b-NoAttack_01-1.tif	4,02	carbide	2,62	porosity	0,37		
10	S06-FL-014b-NoAttack_01-1.tif	0,67	alumina	0,44	matrix	95,16		
11	S06-FL-014b-NoAttack_01-1.tif	0,89	alumina	0,58				
12	S06-FL-014b-NoAttack_01-1.tif	0,45	alumina	0,29				
13	S06-FL-014b-NoAttack_01-1.tif	0,56	porosity	0,37				
14	S06-FL-014b-NoAttack_01-1.tif	136,31	Total lenght	1	carbide	10,33		
15	S06-FL-014b-NoAttack_01-1.tif	6,78	carbide	4,97	alumina	4,44		
16	S06-FL-014b-NoAttack_01-1.tif	1,42	alumina	1,04	porosity	0,66		
17	S06-FL-014b-NoAttack_01-1.tif	0,60	alumina	0,44	matrix	84,57		
18	S06-FL-014b-NoAttack_01-1.tif	3,58	carbide	2,62				
19	S06-FL-014b-NoAttack_01-1.tif	1,19	alumina	0,87				
20	S06-FL-014b-NoAttack_01-1.tif	0,53	alumina	0,39				
21	S06-FL-014b-NoAttack_01-1.tif	1,27	alumina	0,93				
22	S06-FL-014b-NoAttack_01-1.tif	3,72	carbide	2,73				
23	S06-FL-014b-NoAttack_01-1.tif	1,04	alumina	0,77				
24	S06-FL-014b-NoAttack_01-1.tif	0,91	porosity	0,66				

Figure D.9: Summary of the calculation of the proportion of phases for the sample of Cr_2AlC sintered at 1400°C for 5 minutes, with a loading of 10 MPa and a heating time of 100°C/min, SD is the standard deviation

	label of pictures	Length of the segments (µm)	Identification phases	Proportion (%)	Somme of prop for each phases		Mean (%)	SD (%)
1	018_AS_semiAtt_08-1.tif	198,37	Total length	1,00E+00	carbide	0,25	6,45	5,13
2	018_AS_semiAtt_08-1.tif	1,05	porosity	5,27E-03	alumina	1,03	0,59	0,43
3	018_AS_semiAtt_08-1.tif	1,88	porosity	9,50E-03	porosity	6,96	7,98	3,01
4	018_AS_semiAtt_08-1.tif	0,55	porosity	2,79E-03	matrix	91,77	84,97	4,84
5	018_AS_semiAtt_08-1.tif	4,71	porosity	2,37E-02				
6	018_AS_semiAtt_08-1.tif	2,53	porosity	1,27E-02				
7	018_AS_semiAtt_08-1.tif	1,14	alumina	5,75E-03				
8	018_AS_semiAtt_08-1.tif	1,19	porosity	6,01E-03				
9	018_AS_semiAtt_08-1.tif	0,89	alumina	4,50E-03				
10	018_AS_semiAtt_08-1.tif	1,88	porosity	9,50E-03				
11	018_AS_semiAtt_08-1.tif	0,50	carbide	2,50E-03				
1	018_AS_semiAtt_08-1.tif	193,33	Total length	1,00E+00	carbide	6,29		
2	018_AS_semiAtt_08-1.tif	1,33	porosity	6,89E-03	alumina	0,75		
3	018_AS_semiAtt_08-1.tif	4,70	carbide	2,43E-02	porosity	12,08		
4	018_AS_semiAtt_08-1.tif	6,25	porosity	3,23E-02	matrix	80,88		
5	018_AS_semiAtt_08-1.tif	1,31	porosity	6,77E-03				
6	018_AS_semiAtt_08-1.tif	2,37	carbide	1,22E-02				
7	018_AS_semiAtt_08-1.tif	0,52	porosity	2,67E-03				
8	018_AS_semiAtt_08-1.tif	1,28	carbide	6,59E-03				
9	018_AS_semiAtt_08-1.tif	0,70	porosity	3,63E-03				
10	018_AS_semiAtt_08-1.tif	3,23	porosity	1,67E-02				
11	018_AS_semiAtt_08-1.tif	3,82	carbide	1,97E-02				
12	018_AS_semiAtt_08-1.tif	2,85	porosity	1,47E-02				
13	018_AS_semiAtt_08-1.tif	4,12	porosity	2,13E-02				
14	018_AS_semiAtt_08-1.tif	0,68	alumina	3,52E-03				
15	018_AS_semiAtt_08-1.tif	0,77	alumina	3,99E-03				
16	018_AS_semiAtt_08-1.tif	1,92	porosity	9,92E-03				
17	018_AS_semiAtt_08-1.tif	1,13	porosity	5,84E-03				
1	018_AS_semiAtt_08-1.tif	146,35	Total length	1,00E+00	carbide	12,82		
2	018_AS_semiAtt_08-1.tif	3,75	porosity	2,56E-02	alumina	0,00		
3	018_AS_semiAtt_08-1.tif	0,47	porosity	3,23E-03	porosity	4,92		
4	018_AS_semiAtt_08-1.tif	1,55	porosity	1,06E-02	matrix	82,26		
5	018_AS_semiAtt_08-1.tif	7,42	carbide	5,07E-02				
6	018_AS_semiAtt_08-1.tif	11,35	carbide	7,76E-02				
7	018_AS_semiAtt_08-1.tif	1,42	porosity	9,70E-03				

Figure D.10: Summary of the calculation of the proportion of phases for the sample of Cr_2AlC sintered at 1300°C for 5 minutes, with a loading of 10 MPa and a heating time of 100°C/min, SD is the standard deviation

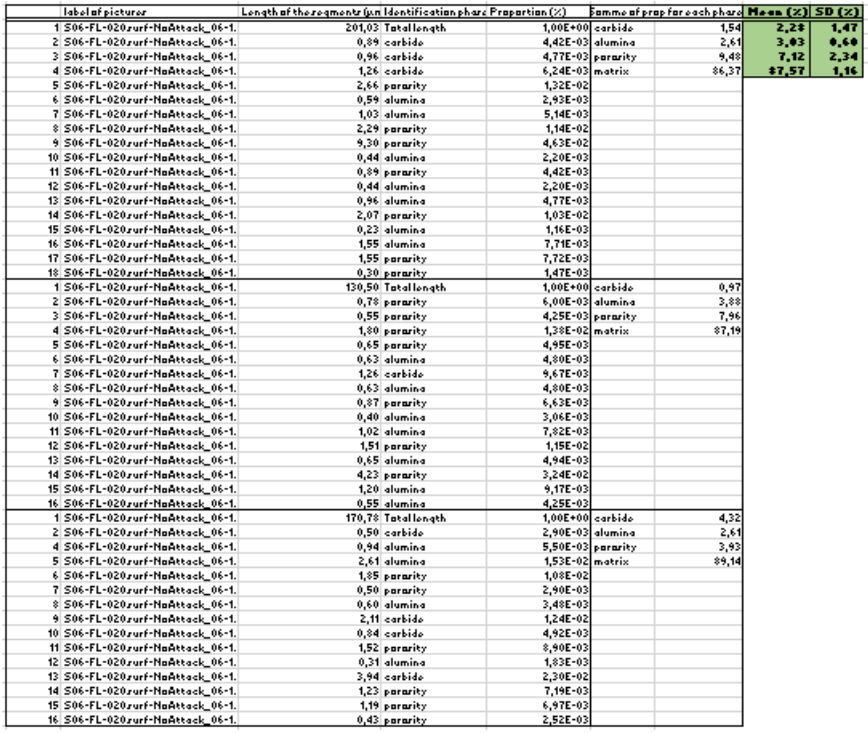

	label of pictures	Length of the segments (µm)	Identification phase	Proportion (%)	Somme of prop for each phase		Mean (%)	SD (%)
1	S06-FL-020zurf-NaAttack_06-1.	201,03	Total length	1,00E+00	carbide	1,54	2,24	1,47
2	S06-FL-020zurf-NaAttack_06-1.	0,89	carbide	4,42E-03	alumina	2,61	3,03	0,69
3	S06-FL-020zurf-NaAttack_06-1.	0,96	carbide	4,77E-03	porarity	9,48	7,12	2,34
4	S06-FL-020zurf-NaAttack_06-1.	1,26	carbide	6,24E-03	matrix	86,37	87,57	1,16
5	S06-FL-020zurf-NaAttack_06-1.	2,66	porarity	1,32E-02				
6	S06-FL-020zurf-NaAttack_06-1.	0,59	alumina	2,93E-03				
7	S06-FL-020zurf-NaAttack_06-1.	1,03	alumina	5,14E-03				
8	S06-FL-020zurf-NaAttack_06-1.	2,29	porarity	1,14E-02				
9	S06-FL-020zurf-NaAttack_06-1.	9,30	porarity	4,63E-02				
10	S06-FL-020zurf-NaAttack_06-1.	0,44	alumina	2,20E-03				
11	S06-FL-020zurf-NaAttack_06-1.	0,89	porarity	4,42E-03				
12	S06-FL-020zurf-NaAttack_06-1.	0,44	alumina	2,20E-03				
13	S06-FL-020zurf-NaAttack_06-1.	0,96	alumina	4,77E-03				
14	S06-FL-020zurf-NaAttack_06-1.	2,07	porarity	1,03E-02				
15	S06-FL-020zurf-NaAttack_06-1.	0,23	alumina	1,16E-03				
16	S06-FL-020zurf-NaAttack_06-1.	1,55	alumina	7,71E-03				
17	S06-FL-020zurf-NaAttack_06-1.	1,55	porarity	7,72E-03				
18	S06-FL-020zurf-NaAttack_06-1.	0,30	porarity	1,47E-03				
1	S06-FL-020zurf-NaAttack_06-1.	130,50	Total length	1,00E+00	carbide	0,97		
2	S06-FL-020zurf-NaAttack_06-1.	0,78	porarity	6,00E-03	alumina	3,88		
3	S06-FL-020zurf-NaAttack_06-1.	0,55	porarity	4,25E-03	porarity	7,96		
4	S06-FL-020zurf-NaAttack_06-1.	1,80	porarity	1,38E-02	matrix	87,19		
5	S06-FL-020zurf-NaAttack_06-1.	0,65	porarity	4,95E-03				
6	S06-FL-020zurf-NaAttack_06-1.	0,63	alumina	4,80E-03				
7	S06-FL-020zurf-NaAttack_06-1.	1,26	carbide	9,67E-03				
8	S06-FL-020zurf-NaAttack_06-1.	0,63	alumina	4,80E-03				
9	S06-FL-020zurf-NaAttack_06-1.	0,87	porarity	6,63E-03				
10	S06-FL-020zurf-NaAttack_06-1.	0,40	alumina	3,06E-03				
11	S06-FL-020zurf-NaAttack_06-1.	1,02	alumina	7,82E-03				
12	S06-FL-020zurf-NaAttack_06-1.	1,51	porarity	1,15E-02				
13	S06-FL-020zurf-NaAttack_06-1.	0,65	alumina	4,94E-03				
14	S06-FL-020zurf-NaAttack_06-1.	4,23	porarity	3,24E-02				
15	S06-FL-020zurf-NaAttack_06-1.	1,20	alumina	9,17E-03				
16	S06-FL-020zurf-NaAttack_06-1.	0,55	alumina	4,25E-03				
1	S06-FL-020zurf-NaAttack_06-1.	170,78	Total length	1,00E+00	carbide	4,32		
2	S06-FL-020zurf-NaAttack_06-1.	0,50	carbide	2,90E-03	alumina	2,61		
4	S06-FL-020zurf-NaAttack_06-1.	0,94	alumina	5,50E-03	porarity	3,93		
5	S06-FL-020zurf-NaAttack_06-1.	2,61	alumina	1,53E-02	matrix	89,14		
6	S06-FL-020zurf-NaAttack_06-1.	1,85	porarity	1,08E-02				
7	S06-FL-020zurf-NaAttack_06-1.	0,50	porarity	2,90E-03				
8	S06-FL-020zurf-NaAttack_06-1.	0,60	alumina	3,48E-03				
9	S06-FL-020zurf-NaAttack_06-1.	2,11	carbide	1,24E-02				
10	S06-FL-020zurf-NaAttack_06-1.	0,84	carbide	4,92E-03				
11	S06-FL-020zurf-NaAttack_06-1.	1,52	porarity	8,90E-03				
12	S06-FL-020zurf-NaAttack_06-1.	0,31	alumina	1,83E-03				
13	S06-FL-020zurf-NaAttack_06-1.	3,94	carbide	2,30E-02				
14	S06-FL-020zurf-NaAttack_06-1.	1,23	porarity	7,19E-03				
15	S06-FL-020zurf-NaAttack_06-1.	1,19	porarity	6,97E-03				
16	S06-FL-020zurf-NaAttack_06-1.	0,43	porarity	2,52E-03				

Figure D.11: Summary of the calculation of the proportion of phases for the sample of Cr_2AlC sintered at 1200°C for 5 minutes, with a loading of 10 MPa and a heating time of 100°C/min, SD is the standard deviation

	label of pictures	Length of the segments (µm)	Identification phases	Proportion (%)	Somme of prop for each phases		Mean (%)	SD (%)
1	030_AS_02.tif	146,73	Total length	1,00E+00	carbide	0,92	0,66	0,21
2	030_AS_02.tif	0,781	alumina	5,32E-03	alumina	1,60	1,73	0,60
3	030_AS_02.tif	0,672	porosity	4,58E-03	porosity	3,95	5,52	1,15
4	030_AS_02.tif	0,773	porosity	5,27E-03	matrix	93,53	92,09	1,42
5	030_AS_02.tif	1,293	porosity	8,81E-03				
6	030_AS_02.tif	1,127	porosity	7,68E-03				
7	030_AS_02.tif	0,699	porosity	4,76E-03				
8	030_AS_02.tif	1,344	carbide	9,16E-03				
9	030_AS_02.tif	1,563	alumina	1,07E-02				
10	030_AS_02.tif	1,235	porosity	8,42E-03				
1	030_AS_02.tif	153,428	Total length	1,00E+00	carbide	0,65		
2	030_AS_02.tif	0,595	porosity	3,88E-03	alumina	2,53		
3	030_AS_02.tif	3,882	porosity	2,53E-02	porosity	6,67		
4	030_AS_02.tif	0,247	porosity	1,61E-03	matrix	90,15		
5	030_AS_02.tif	0,994	carbide	6,48E-03				
6	030_AS_02.tif	1,22	alumina	7,95E-03				
7	030_AS_02.tif	1,088	porosity	7,09E-03				
8	030_AS_02.tif	3,653	porosity	2,38E-02				
9	030_AS_02.tif	0,773	porosity	5,04E-03				
10	030_AS_02.tif	1,551	alumina	1,01E-02				
11	030_AS_02.tif	1,105	alumina	7,20E-03				
1	030_AS_02.tif	144,919	Total length	1,00E+00	carbide	0,41		
2	030_AS_02.tif	0,579	porosity	4,00E-03	alumina	1,06		
3	030_AS_02.tif	0,597	carbide	4,12E-03	porosity	5,94		
4	030_AS_02.tif	0,579	porosity	4,00E-03	matrix	92,58		
5	030_AS_02.tif	0,474	porosity	3,27E-03				
6	030_AS_02.tif	0,474	porosity	3,27E-03				
7	030_AS_02.tif	1,541	alumina	1,06E-02				
8	030_AS_02.tif	2,78	porosity	1,92E-02				
9	030_AS_02.tif	1,366	porosity	9,43E-03				
10	030_AS_02.tif	1,575	porosity	1,09E-02				
11	030_AS_02.tif	0,787	porosity	5,43E-03				

Figure D.12: Summary of the calculation of the proportion of phases for the sample of Cr_2AlC sintered at 1200°C for 5 minutes, with a loading of 30 MPa and a heating time of 100°C/min, SD is the standard deviation

	label of pictures	Length of the segments (µm)	Identification phases	Proportion (%)	Somme of prop for each phases		Mean (%)	SD (%)
1	033_03.tif	83,812	total length	1,00E+00	carbide	12,35	**4,99**	**6,51**
2	033_03.tif	0,611	alumina	7,29E-03	alumina	0,73	**3,91**	**2,75**
3	033_03.tif	1,194	porosity	1,42E-02	porosity	10,20	**6,25**	**4,47**
4	033_03.tif	1,222	carbide	1,46E-02	matrix	76,72	**84,86**	**7,25**
5	033_03.tif	5,724	porosity	6,83E-02				
6	033_03.tif	0,444	porosity	5,30E-03				
7	033_03.tif	1,185	porosity	1,41E-02				
8	033_03.tif	6,855	carbide	8,18E-02				
9	033_03.tif	0,444	carbide	5,30E-03				
10	033_03.tif	1,832	carbide	2,19E-02				
11	033_03.tif	96,485	total length	1,00E+00	carbide	2,61		
12	033_03.tif	0,593	alumina	6,15E-03	alumina	5,39		
13	033_03.tif	1,333	alumina	1,38E-02	porosity	1,39		
14	033_03.tif	0,593	alumina	6,15E-03	matrix	90,61		
15	033_03.tif	2,519	carbide	2,61E-02				
16	033_03.tif	0,901	alumina	9,34E-03				
17	033_03.tif	0,296	porosity	3,07E-03				
18	033_03.tif	1,778	alumina	1,84E-02				
19	033_03.tif	1,048	porosity	1,09E-02				
20	033_03.tif	63,968	total length	1,00E+00	carbide	0,00		
21	033_03.tif	4,573	porosity	7,15E-02	alumina	5,60		
22	033_03.tif	1,325	alumina	2,07E-02	porosity	7,15		
23	033_03.tif	2,257	alumina	3,53E-02	matrix	87,25		

Figure D.13: Summary of the calculation of the proportion of phases for the sample of Cr_2AlC sintered at 1200°C for 5 minutes, with a loading of 50 MPa and a heating time of 100°C/min, SD is the standard deviation

	label of pictures	Length of the segments (µm)	Identification phases	Proportion (%)	Somme of prop for each phases		Mean (%)	SD (%)
1	032_02.tif	93,343	total length	1,00E+00	carbide	2,06	**3,86**	**2,76**
2	032_02.tif	0,663	porosity	7,10E-03	alumina	1,59	**2,83**	**2,81**
3	032_02.tif	2,85	porosity	3,05E-02	porosity	8,54	**7,93**	**4,91**
4	032_02.tif	0,889	alumina	9,52E-03	matrix	87,81	**85,37**	**9,98**
5	032_02.tif	1,926	carbide	2,06E-02				
6	032_02.tif	1,037	porosity	1,11E-02				
7	032_02.tif	2,227	porosity	2,39E-02				
8	032_02.tif	1,194	porosity	1,28E-02				
9	032_02.tif	0,593	alumina	6,35E-03				
10	032_02.tif	100,951	total length	1,00E+00	carbide	7,04		
11	032_02.tif	1,656	alumina	1,64E-02	alumina	6,05		
12	032_02.tif	1,037	alumina	1,03E-02	porosity	12,51		
13	032_02.tif	10,999	porosity	1,09E-01	matrix	74,40		
14	032_02.tif	1,63	porosity	1,61E-02				
15	032_02.tif	5,778	carbide	5,72E-02				
16	032_02.tif	3,411	alumina	3,38E-02				
17	032_02.tif	1,333	carbide	1,32E-02				
18	032_02.tif	76,509	total length	1,00E+00	carbide	2,48		
19	032_02.tif	2,095	porosity	2,74E-02	alumina	0,87		
20	032_02.tif	0,663	alumina	8,67E-03	porosity	2,74		
21	032_02.tif	1,897	carbide	2,48E-02	matrix	93,92		

Figure D.14: Summary of the calculation of the proportion of phases for the sample of Cr_2AlC sintered at 1200°C for 5 minutes, with a loading of 10 MPa and a heating time of 50°C/min, SD is the standard deviation

	label of pictures	Length of the segments (µm)	Identification phases	Proportion (%)	Somme of prop for each phases		Mean (%)	SD (%)
1	029_03.tif	67,01	total length	1,00E+00	carbide	0,00	**3,99**	**0,21**
2	029_03.tif	1,051	porosity	1,57E-02	alumina	0,00	**1,05**	**1,17**
					porosity	1,57	**3,81**	**2,78**
					matrix	98,43	**91,16**	**6,80**
3	029_03.tif	80,257	total length	1,00E+00	carbide	6,13		
4	029_03.tif	0,899	porosity	1,12E-02	alumina	0,83		
5	029_03.tif	0,678	porosity	8,45E-03	porosity	2,94		
6	029_03.tif	0,669	alumina	8,34E-03	matrix	90,10		
7	029_03.tif	0,781	porosity	9,73E-03				
8	029_03.tif	4,918	carbide	6,13E-02				
9	029_03.tif	87,8370	total length	1,00E+00	carbide	5,83		
10	029_03.tif	0,6310	porosity	7,18E-03	alumina	2,30		
12	029_03.tif	0,8670	carbide	9,87E-03	porosity	6,92		
13	029_03.tif	3,5090	carbide	3,99E-02	matrix	84,95		
14	029_03.tif	2,0230	alumina	2,30E-02				
15	029_03.tif	0,7430	carbide	8,46E-03				
16	029_03.tif	3,5090	porosity	3,99E-02				
17	029_03.tif	1,9390	porosity	2,21E-02				

Figure D.15: Summary of the calculation of the proportion of phases for the sample of Cr_2AlC sintered at 1200°C for 5 minutes, with a loading of 10 MPa and a heating time of 200°C/min, SD is the standard deviation

Appendix E

DRX analyse

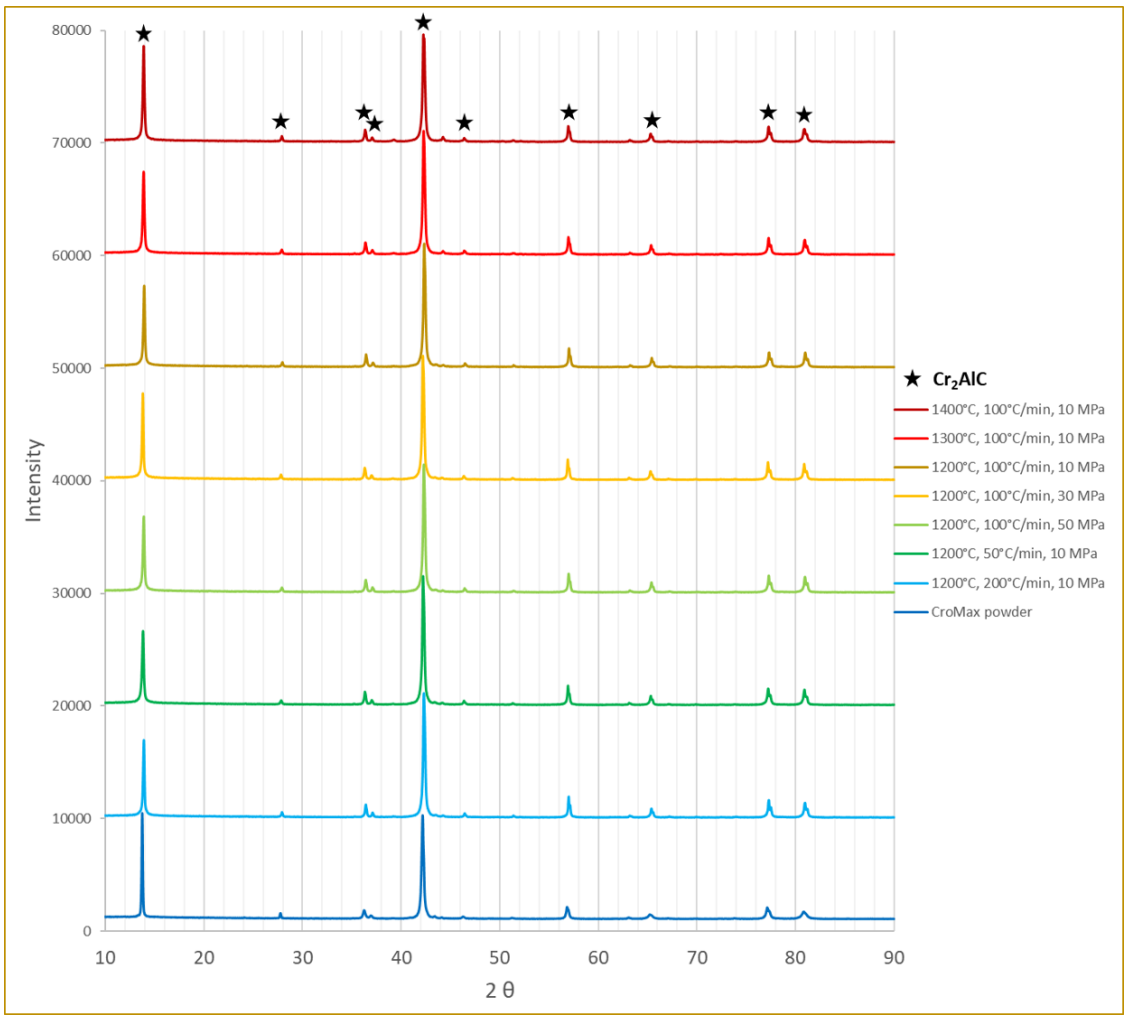

Figure E.1: XRD spectrum of the samples sintered with 6g of powder, study in Chapter 3

Appendix F

Load/Displacement curves

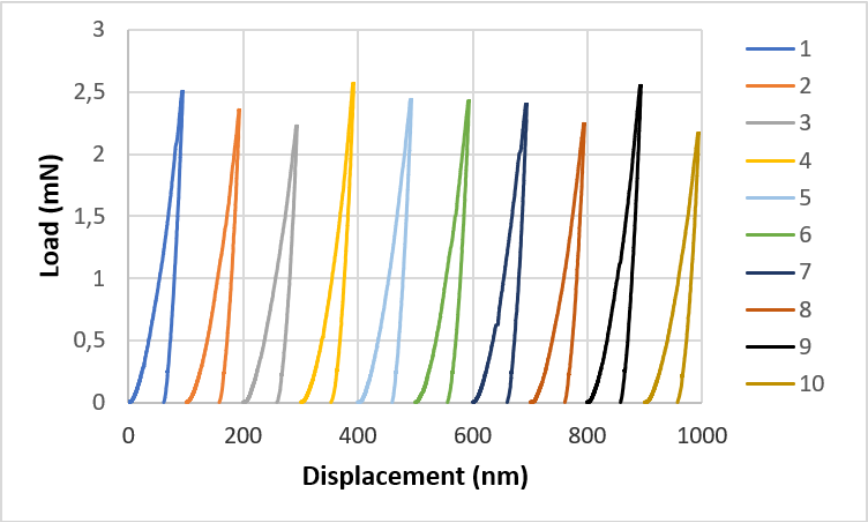

Figure F.1: Load/displacement curves of the 10 Berkovich indents with a depth of 100 nm, the curves are shifted of 100 nm to see them distinctly

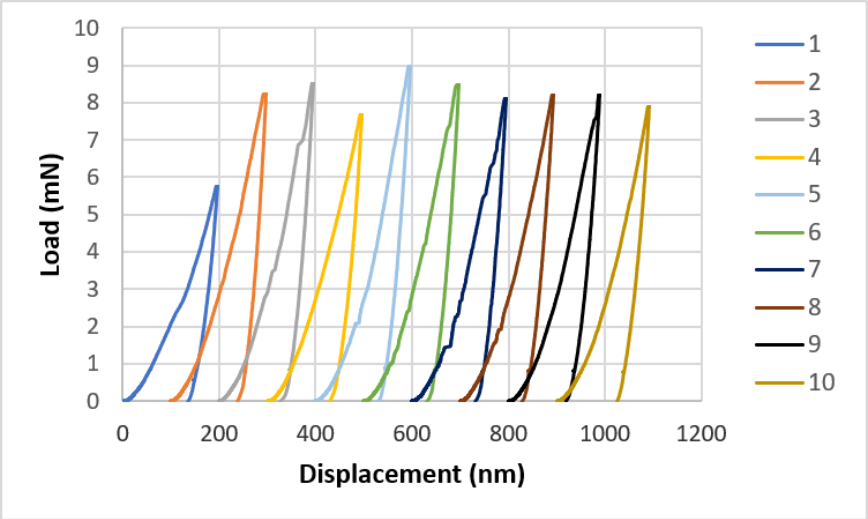

Figure F.2: Load/displacement curves of the 10 Berkovich indents with a depth of 200 nm, the curves are shifted of 100 nm to see them distinctly

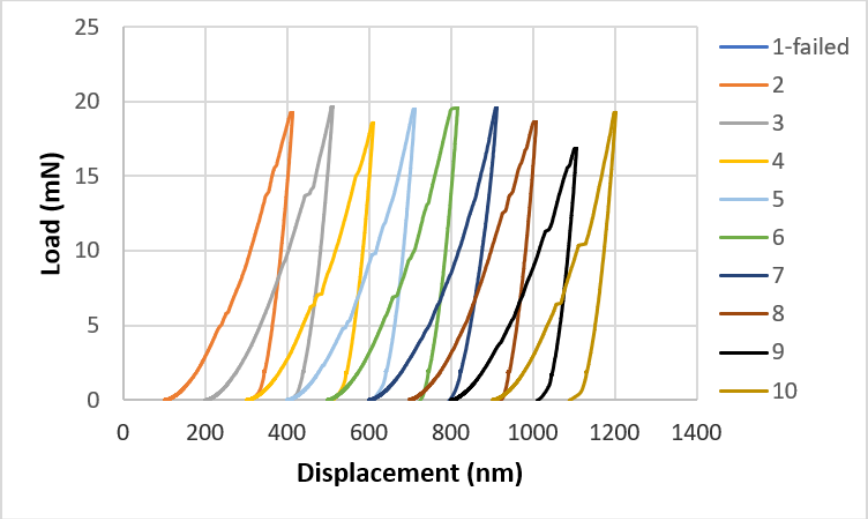

Figure F.3: Load/displacement curves of the 10 Berkovich indents with a depth of 300 nm, the curves are shifted of 100 nm to see them distinctly, the first indent failed

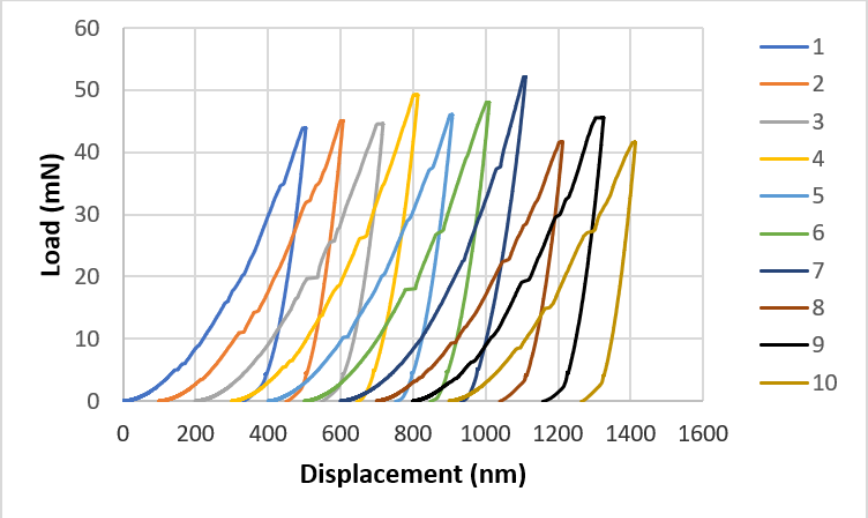

Figure F.4: Load/displacement curves of the 10 Berkovich indents with a depth of 500 nm, the curves are shifted of 100 nm to see them distinctly

Bibliography

[ALG17] Babak Anasori, Maria R Lukatskaya, and Yury Gogotsi. 2d metal carbides and nitrides (mxenes) for energy storage. Nature Reviews Materials, 2:16098, 2017.

[Bar00] Michel W Barsoum. The $M_{n+1}AX_n$ phases: A new class of solids: Thermodynamically stable nanolaminates. Progress in Solid State Chemistry, 28(1-4):201–281, 2000.

[Bar13] Michel W Barsoum. MAX phases: properties of machinable ternary carbides and nitrides. John Wiley & Sons, 2013.

[BR11] Michel W Barsoum and Miladin Radovic. Elastic and mechanical properties of the max phases. Annual review of materials research, 41:195–227, 2011.

[BZK+03] MW Barsoum, T Zhen, SR Kalidindi, M Radovic, and A Murugaiah. Fully reversible, dislocation-based compressive deformation of ti3sic2 to 1 gpa. Nature Materials, 2(2):107–111, 2003.

[CK14] Maria Cowan and Kapil Khandelwal. Modeling of high temperature creep in astm a992 structural steels. Engineering Structures, 80:426 – 434, 2014.

[CM99] Krishan Kumar Chawla and MA Meyers. Mechanical behavior of materials. Prentice Hall, 1999.

[Cob63] RL Coble. A model for boundary diffusion controlled creep in polycrystalline materials. Journal of applied physics, 34(6):1679–1682, 1963.

[Dem11] Maryse Demuynck. Spark Plasma Sintering (SPS): Evaluation critique d'une methode de frittage rapide et de son applicabilité aux ceramiques techniques et compasites. PhD thesis, Ecole polytechnique de Louvain, Université catholique de Louvain, Septembre 2011.

[DSJ+15] Xiaoming Duan, Lu Shen, Dechang Jia, Yu Zhou, Sybrand van der Zwaag, and Willem G. Sloof. Synthesis of high-purity, isotropic or textured cr2alc bulk ceramics by spark plasma sintering of pressure-less sintered powders. Journal of the European Ceramic Society, 35(5):1393 – 1400, 2015.

[eFu18] eFunda. Compression members, May 2018. http://www.efunda.com/formulae/solid_ mechanics/columns/intro.cfm.

[ENS98] Olivier Gabathuler ENSCI. Site internet consacré à la découverte des céramiques industrielles et à ses applications, December 1998. http://ogabathuler.free.fr/Francais/Histoire/histoire.html.

[GGP+09] Gemma Guilera, Bernard Gorges, Sakura Pascarelli, Hugo Vitoux, Mark A Newton, Carmelo Prestipino, Yasutaka Nagai, and Naoyuki Hara. Novel high-temperature

reactors for in situ studies of three-way catalysts using turbo-xas. Journal of synchrotron radiation, 16(5):628–634, 2009.

[GJGMV18] J Gonzalez-Julian, T Go, DE Mack, and R Vaßen. Thermal cycling testing of tbcs on cr2alc max phase substrates. Surface and Coatings Technology, 340:17–24, 2018.

[GJOBG16] Jesus Gonzalez-Julian, Sara Onrubia, Martin Bram, and Olivier Guillon. Effect of sintering method on the microstructure of pure cr2alc max phase ceramics. Journal of the Ceramic Society of Japan, 124(4):415–420, 2016.

[GK18] Technology GmbH and Co. KG. Surface, always one step ahead, April 2018. http://www.surfacetec.com/nanotips.php.

[Hen07] Charles Henager. Hydrogen Permeation Barrier Coatings. CRC Press 2007, 12 2007.

[Ins18] Instron. Compression test, May 2018. http://www.instron.in/en-in/our-company/library/test-types/compression-test.

[JI17] Pascal Jacques and Hosni Idrissi. LMAPR 2642 Crystallographic and Microstructural Characterisation of Materials. Université Catholique de Louvain-la-Neuve, 2017.

[JS18] Pascal Jacques and Aude Simar. LMAPR 2420 High Performance Metallic Materials. Université Catholique de Louvain-la-Neuve, 2018.

[KAS+13] Mohammad Khazaei, Masao Arai, Taizo Sasaki, Chan-Yeup Chung, Natarajan S Venkataramanan, Mehdi Estili, Yoshio Sakka, and Yoshiyuki Kawazoe. Novel electronic and magnetic properties of two-dimensional transition metal carbides and nitrides. Advanced Functional Materials, 23(17):2185–2192, 2013.

[LGS+96] P-L Larsson, AE Giannakopoulos, E Söderlund, DJ Rowcliffe, and R Vestergaard. Analysis of berkovich indentation. International Journal of Solids and Structures, 33(2):221–248, 1996.

[Low12] It-Meng Low. Advances in science and technology of Mn+ 1AXn phases. Woodhead Publishing Limited 2012, 2012.

[LZZ15] Jin-Cheng Lei, Xu Zhang, and Zhen Zhou. Recent advances in mxene: Preparation, properties, and applications. Frontiers of Physics, 10:276–286, 2015.

[Mur17] KL Murty. Creep and Stress Rupture. NC State University, 2017.

[NKP+11] Michael Naguib, Murat Kurtoglu, Volker Presser, Jun Lu, Junjie Niu, Min Heon, Lars Hultman, Yury Gogotsi, and Michel W Barsoum. Two-dimensional nanocrystals produced by exfoliation of ti3alc2. Advanced Materials, 23(37):4248–4253, 2011.

[Now71] Von Hans Nowotny. Strukturchemie einiger verbindungen der übergangsmetalle mit den elementen c, si, ge, sn. Progress in Solid State Chemistry, 5:27–70, 1971.

[PB85] J.J. Poubeau and J. Bigot. Determination de la solubilite du carbone dans le chrome par mesure de la resistivite electrique a basse temperature. Acta Metallurgica, 33(6):1137 – 1141, 1985.

[PRX+11] A Poty, J.-M Raulot, H Xu, J Bai, Christophe Schuman, Jean-Sebastien Lecomte, Marie-Jeanne Philippe, and C Esling. Classification of the critical resolved shear stress in the hexagonal-close-packed materials by atomic simulation: Application to -zirconium and -titanium. Journal of Applied Physics, 110:014905–014905, 07 2011.

[RB13] Miladin Radovic and Michel W Barsoum. Max phases: bridging the gap between metals and ceramics. American Ceramics Society Bulletin, 92(3):20–27, 2013.

[SAL+09] TH Scabarozi, S Amini, O Leaffer, A Ganguly, S Gupta, W Tambussi, S Clipper, l JE Spanier, MW Barsoum, JD Hettinger, et al. Thermal expansion of select m n+ 1 ax n (m= early transition metal, a= a group element, x= c or n) phases measured by high temperature x-ray diffraction and dilatometry. Journal of Applied Physics, 105(1):013543, 2009.

[SMZ+05] ZM Sun, A Murugaiah, T Zhen, A Zhou, and MW Barsoum. Microstructure and mechanical properties of porous ti3sic2. Acta materialia, 53(16):4359–4366, 2005.

[Sub18] SubsTech. General classification of ceramics, March 2018. http://www.substech.com/dokuwiki/doku.php?id=general_classification_of_ceramics.

[Sun11] ZM Sun. Progress in research and development on max phases: a family of layered ternary compounds. International Materials Reviews, 56(3):143–166, 2011.

[TSHD09] Wubian Tian, ZhengMing Sun, Hitoshi Hashimoto, and Yulei Du. Compressive deformation behavior of ternary compound cr2alc. Journal of materials science, 44(1):102–107, 2009.

[TWZ+06a] Wubian Tian, Peiling Wang, Guojun Zhang, Yanmei Kan, Yongxiang Li, and Dongsheng Yan. Synthesis and thermal and electrical properties of bulk cr2alc. Scripta Materialia, 54(5):841 – 846, 2006. Viewpoint set no. 39: Statistical mechanics and coarse graining of dislocation behavior for continuum plasticity.

[TWZ+06b] Wubian Tian, Peiling Wang, Guojun Zhang, Yanmei Kan, Yongxiang Li, and Dongsheng Yan. Synthesis and thermal and electrical properties of bulk cr2alc. Scripta Materialia, 54(5):841–846, 2006.

[Wik18a] Wikipedia. Aluminium oxide, May 2018. https://en.wikipedia.org/wiki/Aluminium_oxide.

[Wik18b] Wikipedia. Ceramic, March 2018. https://en.wikipedia.org/wiki/Ceramic.

[Wik18c] Wikipedia. Contact de hertz, May 2018. https://fr.wikipedia.org/wiki/Contact_de_Hertz.

[Wik18d] Wikipedia. Diffusion creep, April 2018. https://en.wikipedia.org/wiki/Diffusion_creep.

[Wik18e] Wikipedia. Nanoindentation, May 2018. https://en.wikipedia.org/wiki/Nanoindentation.

[Wik18f] Wikipédia. Stress−strain curve, April 2018. https://en.wikipedia.org/wiki/Stress_strain_curve.

[Wik18g] Wikipédia. Thermal expansion, May 2018. https://en.wikipedia.org/wiki/Thermal_expansion.

[ZBK+05] T Zhen, MW Barsoum, SR Kalidindi, M Radovic, ZM Sun, and T El-Raghy. Compressive creep of fine and coarse-grained ti3sic2 in air in the 1100–1300°C temperature range. Acta materialia, 53(19):4963–4973, 2005.

Rue Archimède, 1 bte L6.11.01, 1348 Louvain-la-Neuve **www.uclouvain.be/epl**